NACA RM A56I05

NACA

RESEARCH MEMORANDUM

SOME EXPERIMENTS AT HIGH SUPERSONIC SPEEDS ON THE AERODYNAMIC AND BOUNDARY-LAYER TRANSITION CHARACTERISTICS OF HIGH-DRAG BODIES OF REVOLUTION

By Alvin Seiff, Simon C. Sommer, and
Thomas N. Canning

Ames Aeronautical Laboratory
Moffett Field, Calif.

NATIONAL ADVISORY COMMITTEE
FOR AERONAUTICS

WASHINGTON

January 14, 1957
Declassified May 29, 1961

TABLE OF CONTENTS

	Page
SUMMARY	1
INTRODUCTION	1
NOTATION	4
Subscripts	7
Derivative Notation	7
APPARATUS AND TEST TECHNIQUE	7
Facilities	7
Models	8
Surface Finish	8
Type I	9
Type II	9
Type III	9
Range of Test Variables	10
Data Reduction	11
RESULTS AND DISCUSSION	13
Force and Moment Data	13
Drag	14
Static stability	15
Dynamic stability	16
Boundary-Layer Transition	17
Evidence of turbulence	17
Round-nosed 60° cone	19
Pointed 60° cone	21
Hemisphere	22
Comparison with earlier data from slender-model tests	23
Pointed ogives	24
Round-nosed ogive	24
Round-nosed 30° cone	25
Comparison of Roughness Height to Boundary-Layer Thickness	26
Pointed bodies	26
Correlation of critical-roughness data for pointed bodies	27
Round-nosed bodies	29
Effect of scale	29
Other Causes of Boundary-Layer Instability	32
Pressure gradients	32
Shear-layer effects	34
Air-stream turbulence	36
Görtler instability	36
Reynolds Numbers for High-Speed Entry Into the Earth's Atmosphere	37
CONCLUSIONS	38
APPENDIX A - EQUATIONS OF PITCHING MOTION FOR A MISSILE IN DECELERATING FREE FLIGHT AT CONSTANT ALTITUDE	41

TABLE OF CONTENTS - Concluded

Page

APPENDIX B - RELATIVE CONTRIBUTIONS OF AERODYNAMIC DAMPING AND DAMPING DUE TO DYNAMIC-PRESSURE VARIATION 45
APPENDIX C - METHOD OF CALCULATING BOUNDARY-LAYER THICKNESS 50
REFERENCES 52
FIGURES 57

NATIONAL ADVISORY COMMITTEE FOR AERONAUTICS

RESEARCH MEMORANDUM

SOME EXPERIMENTS AT HIGH SUPERSONIC SPEEDS ON THE AERODYNAMIC AND BOUNDARY-LAYER TRANSITION CHARACTERISTICS OF HIGH-DRAG BODIES OF REVOLUTION

By Alvin Seiff, Simon C. Sommer, and
Thomas N. Canning

SUMMARY

Measurements have been made at Mach numbers of 4.0 and 8.3 of the drag, static stability, damping in pitch, and boundary-layer transition characteristics of a number of high-drag bodies of revolution of a type that might be used for high-speed entry into the earth's atmosphere. It was found that the static stability of the test models was inherently very great with centers of pressure as far aft as 91 percent of the length from the nose. The damping coefficients measured for a round-nosed 60° cone were found to be adequate for rapid damping of pitching oscillations of a full-scale vehicle. Boundary-layer transition on these models was found to occur at low Reynolds numbers compared to what has been obtained on slender models at the same free-stream conditions. Raising the Mach number had a favorable effect on the extent of laminar flow, but did not significantly increase the Reynolds number of transition when based on local flow properties. The reasons underlying the early transition were studied and are discussed.

INTRODUCTION

In reference 1, it was shown that bodies of moderate size and weight can enter the earth's atmosphere at hypersonic velocity with less aerodynamic heat input if the wave drag is large than if the body is slender and aerodynamically efficient. This is due to the fact that wave drag converts missile kinetic energy to heat in the atmosphere, whereas the

large skin-friction drag associated with slender bodies converts missile kinetic energy to heat in the missile. This finding focuses interest on the hypersonic aerodynamic characteristics of bodies with large wave drag. Many things are poorly understood in this flow regime, and the authors of this report chose to investigate the following:

1. Boundary-layer transition characteristics of high-drag bodies.

2. Static and dynamic flight stability of high-drag bodies.

3. Adequacy of Newtonian theory for predicting force and moment characteristics of these bodies.

The importance of boundary-layer transition at hypersonic speeds is generally known. Turbulent boundary layers transfer significantly larger amounts of heat than laminar boundary layers, the exact comparison depending on particular conditions. Therefore, the difficult problem of coping with aerodynamic heating during atmospheric entry is alleviated if the boundary layer remains laminar.

There has been considerable speculation on the likelihood of laminar flow on high-drag bodies at hypersonic speeds. This speculation has been based on subsonic experience with spheres, supersonic and hypersonic wind-tunnel experience with slender bodies, supersonic wind-tunnel experience with spheres, and laminar stability theory. The subsonic experience showed that a strong negative pressure gradient such as occurs on a sphere is very favorable for keeping the boundary layer laminar. The supersonic experience with slender bodies showed that heat transfer into the body significantly increases the stability of laminar flow. Spheres tested supersonically at nearly zero heat transfer (refs. 2, 3, and 4) have given indications of laminar boundary layers at moderate Reynolds numbers. Laminar stability theory has been used (see, e.g., ref. 5) to conclude that high-drag pointed cones of large included angle will, for all reasonable values of wall temperature in flight, have stable laminar boundary layers at hypersonic speeds. Since pointed cones may require rounding to avoid loss of the tip due to overheating in flight, the effect of rounding off the cone is of interest. This has been discussed in references 6 and 7 and was found to be favorable to laminar flow in one important sense - the local Reynolds numbers are appreciably reduced due to rounding. Thus, several indications lead to the expectation that laminar flow should not be difficult to retain on spheres and round-nosed cones at hypersonic speeds.

Two factors have appeared to work against keeping the boundary-layer laminar on a missile entering the atmosphere. The first is angle of attack. The missile can be expected to enter the atmosphere with

some angular misalignment, and thereafter to undergo a pitching oscillation. Slender bodies at angle of attack have been shown (ref. 8) to experience transition on their sheltered sides at angles of attack as small as 1°. The expectation for low-fineness-ratio bodies, reference 8, is that they will not be as sensitive to angle of attack. However, the changes in the boundary layer due to angle of attack are so complex that this cannot be accepted with assurance. A second factor opposing laminar flow is surface roughness. Hypersonic missiles may be subjected to dust collisions, surface oxidation, and surface ablation in flight, thus producing, in some degree, a roughened surface. It is therefore particularly important to know the effect of surface roughness on transition for this application.

With this background information in mind, it was decided to make tests of hemispheres, pointed cones with 60° included angle, and 60° cones with the nose rounded off spherically. As the tests proceeded, additional test configurations were added to investigate particular points. The test conditions were Mach numbers of 4 and 8 with the models at room temperature and with stagnation air temperatures of 2200° and 4300° Rankine, thus simulating the flight condition of large heat-transfer rate into the body surface.

Little is known about the static and dynamic flight stability of high-drag bodies. For cones of large included angle, the center of pressure is known to lie somewhat behind 2/3 the length from the nose (the position for slender cones). For the other test bodies only the Newtonian theory was available for estimating the static stability, but the accuracy of such estimates was not known. Moreover, no measurements of dynamic stability derivatives for high-drag bodies at hypersonic speeds are known to the authors. Therefore exploratory measurements of the aerodynamic characteristics of the test bodies were made to see if they were satisfactory for practical application.

Work has been done on the drag and pressure distributions of high-drag configurations at hypersonic speeds. Reference 9, for example, gives pressure distributions on round-nosed cones and hemispheres, while references 2, 3, and 4 give similar data for spheres. Drag data has been reported for cones of large included angle (ref. 10) and spheres (refs. 11 and 12). Drag measurements were likewise made in the present test and are compared in the report with the preceding data and with Newtonian theory.

Preliminary results of that portion of the present tests dealing with transition were previously reported in reference 13.

NOTATION

A	frontal area, ft^2
C_D	drag coefficient, $\frac{drag}{q_\infty A}$
C_L	lift coefficient, $\frac{lift}{q_\infty A}$
C_{L_α}	lift-curve slope, $\frac{dC_L}{d\alpha}$, per radian
C_m	pitching-moment coefficient, $\frac{\text{pitching moment}}{q_\infty A l}$
C_{m_α}	pitching-moment-curve slope, $\frac{dC_m}{d\alpha}$, per radian
C_{m_q}	damping-moment coefficient, $\frac{\partial C_m}{\partial\left(\dot{\theta}\frac{l}{V}\right)}$
$C_{m_{\dot{\alpha}}}$	damping-moment coefficient, $\frac{\partial C_m}{\partial\left(\dot{\alpha}\frac{l}{V}\right)}$
C_N	normal-force coefficient, $\frac{\text{normal force}}{q_\infty A}$
C_{N_α}	normal-force-curve slope, $\frac{dC_N}{d\alpha}$, per radian
C_p	pressure coefficient, $\frac{p - p_\infty}{q_\infty}$
C_{p_t}	pitot-pressure coefficient, $\frac{p_t - p_\infty}{q_\infty}$
d	diameter, ft
d_n	nose diameter, ft

e	Naperian base
f	frequency, cps
h	roughness height, in.
I_y	transverse moment of inertia about y axis through center-of-gravity, $m\sigma^2$, slug ft^2
J_o	Bessel function of the first kind
$\frac{k_1}{2}$	damping constant defined in equation (5), ft^{-1}
k_2	frequency-determining constant defined in equation (A10), ft^{-2}
k_3	damping constant defined in equation (B12)
k_4	frequency-determining constant defined in equation (B13)
l	reference length, ft
m	mass, slugs
M	Mach number
$\frac{n_T}{N}$	number of observations, n_T, in which a given station on the body is turbulent, compared to the total number of observations, N
p	static pressure, lb/ft^2
p_t	total pressure behind normal shock wave, lb/ft^2
q_∞	free-stream dynamic pressure, lb/ft^2
R_n	free-stream Reynolds number based on nose diameter, $\frac{\rho_\infty u_\infty d_n}{\mu_\infty}$
R_h	Reynolds number based on roughness height, $\frac{\rho_1 u_1 h}{\mu_1}$
R_∞	Reynolds number based on diameter, $\frac{\rho_\infty u_\infty d}{\mu_\infty}$
R_s	Reynolds number based on distance along model surface, $\frac{\rho_1 u_1 s}{\mu_1}$

R_x	Reynolds number based on axial distance from leading edge, $\frac{\rho_1 u_1 x}{\mu_1}$
s	distance along model surface, ft
s_T	distance along model surface to point of transition, ft
t	time, sec
T	temperature, ^{o}R
u	velocity, ft/sec
V	velocity along flight path, ft/sec
V_E	velocity at which missile enters earth's atmosphere, ft/sec
x	coordinate along the model axis or along the flight path, ft
x_{cg}	distance from nose to center of gravity, ft
x_{cp}	distance from nose to center of pressure, ft
y	altitude, ft
α	angle of attack, radians except where noted
α_{max}	envelope of pitching oscillation, deg
β	constant, 1/22,000, ft^{-1}
γ	flight-path angle, radians
δ	boundary-layer thickness, ft
δ_{sp}	initial boundary-layer thickness at stagnation point, ft
λ	wave length of pitching oscillation, ft/cycle
μ	coefficient of viscosity, lb sec/ft^2
ρ	air density, slugs/ft^3
ρ_o	datum air density, 0.0034 slugs/ft^3
σ	radius of gyration, ft
θ	angle between body axis and horizontal, radians

θ_c cone half-angle, deg

θ_E flight-path angle at which missile enters earth's atmosphere, deg

θ_s inclination of body surface to free-stream direction, deg

ζ $\left(C_{m_q} + C_{m_{\dot{\alpha}}}\right)\left(\frac{l}{\sigma}\right)^2 + C_D - C_{L_\alpha}$

Subscripts

∞ free-stream conditions

1 conditions at outer edge of boundary layer

w conditions at model surface

i initial conditions

R resultant

Derivative Notation

$(\dot{}),(\ddot{})$ first and second derivatives with respect to time, respectively

$(')$,$(")$ first and second derivatives with respect to distance, respectively

APPARATUS AND TEST TECHNIQUE

Facilities

The test facilities used for this investigation were the Ames supersonic free-flight wind tunnel (ref. 14) and the Ames supersonic free-flight underground range. In the former, gun-launched models are flown upstream through the test section of a supersonic wind tunnel to produce hypersonic test conditions. The wind-tunnel test section is equipped with four shadowgraph stations at 5-foot intervals along the flight path to record the motion history of the models. Reynolds number variation is obtained by variation of the supply air pressure. The underground range is a more conventional ballistic-type firing range in which models are fired through still air at atmospheric pressure. The instrumentation

consists of seven shadowgraph stations at 11-foot intervals. In both facilities, test models were launched from a 1.75-inch bore diameter smooth-bore gun.

Models

The basic model, the 60° included-angle cone with a spherical tip, had a tip radius equal to one-third the cone-base radius, and a base radius of 0.863 inch. The geometry behind the base varied, depending upon the launching technique used. One type had a short, threaded base extension, with diameter equal to 71 percent of the base diameter, which screwed into a split nylon sabot. After leaving the gun, the sabot halves separated leaving the model in free flight. The second type had a slender shaft extending from the center of the base (diameter about 8-1/2 percent of the base diameter and 0.75 inch long) which not only supported the model in the sabot but also aided in the determination of the angle of attack from the shadowgraphs. Both types were made of 7075-T6 aluminum, and are shown seated on their respective sabots in figure 1(a). A third variation of this model was geometrically identical to the second type; however, the forward 90 percent of the model length was constructed of magnesium and the last 10 percent plus the shaft was constructed of high-strength steel in order to move the center-of-gravity position aft.

The auxiliary models used are represented in figures 1(b) and 1(c). Figure 1(b) shows a 60° included-angle pointed cone and a hemisphere with the same base diameter as the round-nosed cone of figure 1(a), and also shows a 3/8-inch-diameter sphere. The cone and hemisphere were made of 7075-T6 aluminum, and the sphere was a commercial steel ball bearing. A slight modification of the hemisphere, a spherical segment subtending a total angle of 214°, was also employed. Illustrated in figure 1(c) is a series of aluminum models that were tested primarily to investigate boundary-layer transition. The model shown at the top of the figure is a segment of a pointed ogive. The next model differs only in that it has a rounded nose, the rounded portion (enlarged and illustrated to the left of the model in the figure) being a section of a sine wave of revolution faired into the basic ogive with continuous first and second derivatives at the tangent point. The model shown at the bottom of the figure is a spherical-tipped 30° included-angle cone. This model, unlike the others, was launched using the vacuum technique described in reference 14 for holding the model on the sabot.

Surface Finish

The methods of surface preparation and inspection used in this investigation were patterned after and developed from the methods

described in reference 8. Three classes of surface finish were employed. These will be described, and then the techniques used to inspect them will be outlined.

Type I.- Successively finer grades of emery polishing paper were used, with care exercised at each step to remove the polishing scratches of the previous step. For the final polish the finest available grade, designated 4/0, was used. This procedure resulted in a finish with circumferential scratches as much as 10 to 20 microinches deep (as determined with a surface interferometer to be described below). The scratch width or spacing was determined from photomicrographs to be about 500 microinches or 0.0005 inch. Scratches of this dimension are perceptible to the naked eye, as can be seen in figure 1(a), which shows models with Type I surface finish.

Type II.- Models with Type I finish were repolished with maximum care using grades 3/0 and 4/0 paper in an effort to improve the uniformity of the surface. Scratches were comparable to those in the Type I surface.

Type III.- Models with Type II surface were further polished with aluminum-oxide abrasive of 20-microinch particle size. The circumferential scratches were reduced to a depth of 3 to 5 microinches and were normally less than 0.01 inch long. However, the Type III surfaces had more three-dimensional roughness, usually pits left by pulling out alloying inclusions, than Types I and II. Figure 1(d) shows a model with a Type III surface.

One of the techniques used to inspect the model surfaces was direct examination with a metallurgical microscope. A photomicrograph at 500X typical of either a Type I or a Type II finish is shown in figure 2(a).[1] The polishing scratches are very conspicuous. A Type III surface at the same magnification is shown in figure 2(b). The scratches are now greatly reduced but still perceptible. The alloying inclusions and pits referred to above show up as dark spots in the photomicrograph.

To measure the height of the roughness, a surface interferometer was employed. It consists of a partly silvered optical flat placed in contact with the model surface, with the region near the point of contact in view through a microscope. Monochromatic light is used for illuminating the mirror from above. Fringes are then observed in the microscope. Photomicrographs of the fringes are shown in figures 2(c), 2(d), and 2(e). The fringes result from interference between light reflected from the mirror and light reflected from the model surface. They can be shown to be contour lines of constant distance between the model surface and the mirror. Adjacent fringes mark contours which differ in elevation by half

[1]The broad, dark line running across the middle of the picture is a wire shadow used for measurement of rough surfaces. It has no significance in the present case.

the wave length of the light. In the present case, green light from the mercury-arc spectrum was used, and the half wave length is approximately 10 microinches. Where the contour lines are smooth, the surface is smooth. Where the contour line is displaced, for example, by half a fringe space, there exists a 5-microinch irregularity in the surface.

Figure 2(c) shows an interferogram of a Type I surface. The worst scratches and ridges are seen to be about 10 microinches high and, in a few places, the depth may exceed 10 microinches. The Type III surface, shown in figure 2(d), has roughness nowhere greater than about 5 microinches. The root-mean-square roughness would, of course, be considerably less. The stagnation point of a model with Type III surface is shown in figure 2(e). A scratch ranging from 3 to 10 microinches deep runs directly across the stagnation point. Examination of representative pictures like these three led to the selection of peak roughness amplitudes given earlier.

Range of Test Variables

When the models were fired through still air in either the wind tunnel or underground range, the Mach number was limited to about 4.5. Tests in the wind tunnel with an air-stream Mach number of 2 gave test Mach numbers up to 9.3. The model velocities ranged from 3500 to 6000 feet per second and were controlled by varying the propellent powder charge. The nominal test Mach numbers, temperature conditions, and Reynolds numbers based on free-stream properties and maximum diameter are listed below for each of the models tested.

M_∞	Model type	$R_\infty \times 10^{-6}$	Free-stream static air temperature, T_∞, $^\circ R$	Stagnation temperature (computed), $^\circ R$	T_w/T_∞
3	60° cone	3.0	530	1450	1.0
4	Round-nosed 60° cone Hemisphere Pointed ogive Sine-wave-rounded ogive Round-nosed 30° cone	3.8	530	2200	1.0
8.3	Round-nosed 60° cone 60° cone Hemisphere	4.8	295	4300	1.8
9.3	3/8-in.-diameter sphere	1.1	295	5300	1.8

A pertinent variable for transition tests, the ratio of local wall temperature to local static air temperature just outside the boundary layer, T_w/T_1, is omitted from the above table because T_1 varies along the body, except in the case of the pointed cone, so that no single value of T_w/T_1 will describe conditions for the entire body. However, it can be noted that T_1 is always higher than T_∞ for the models tested, and therefore that T_w/T_1 is always less than the values tabulated above for T_w/T_∞.

Data Reduction

The methods used for measuring force and moment characteristics will be described in this section. Methods used to detect the location of boundary-layer transition will, because of their intimate relation to the results obtained, be included in the later section where boundary-layer transition is treated in detail.

Aerodynamic forces and moments studied included drag, static stability, dynamic stability, and (briefly) lift-curve slope. These characteristics were determined from the shadowgraph records of model motion as a function of time and distance. Drag coefficients were computed from the deceleration of the models by the procedure given in reference 14. Static stability was computed from the frequency of pitching oscillation. To determine the frequency, a damped sine wave,

$$\alpha = e^{-\frac{k_1}{2}x}\left(C_1 \cos 2\pi \frac{x}{\lambda} - C_2 \sin 2\pi \frac{x}{\lambda}\right) \tag{1}$$

is fitted by least squares to the available observations of α as a function of distance traveled, x. An example set of data and the fitted sine wave are given in figure 3. From the pitching frequency, the static stability derivative, C_{m_α}, was computed by use of the relation

$$C_{m_\alpha} = -\left[\frac{(2\pi f)^2 I_y}{q_\infty A l} + \frac{k_1^2 I_y}{2\rho_\infty A l} + \frac{C_{m_q} C_{L_\alpha} \rho_\infty A l}{2m} + \frac{C_D C_{L_\alpha} \rho_\infty A I_y}{2 l m^2}\right] \tag{2a}$$

which is derived in Appendix A. This equation assumes linear pitching moment and damping proportional to pitching rate, but it differs from equations that have been given previously in that the effect of model deceleration on the pitching motion is accounted for. Including this effect leads to the result that the pitching frequency is proportional to velocity, but that the wave length of oscillation, λ, is constant. There is, then, a significant advantage in using distance as the

independent variable in equation (1) rather than time. Furthermore a small-order term involving C_D is found to occur in equation (2a). This term, however, and the two preceding terms are found to be negligible for the present test conditions (less than 1/2 percent of the first term, total) even though the velocity loss in flight was relatively large. The resulting equation used was

$$C_{m_\alpha} = -\left[\frac{(2\pi f)^2 I_y}{q_\infty A l}\right] = -\frac{8\pi^2}{\lambda^2}\frac{I_y}{\rho_\infty A l} \tag{2b}$$

where, in the case of the countercurrent air stream, λ must be defined as the wave length relative to the free-stream air.

The pitching-moment data obtained in this way were broken down to give normal-force-curve slopes and center-of-pressure locations by use of the familiar relation

$$C_{m_\alpha} = C_{N_\alpha}\frac{x_{cp} - x_{cg}}{l} \tag{3}$$

Since both center-of-pressure location and normal-force-curve slope are unknown, the data from two models with different center-of-gravity locations are required. (As was noted in the section on models, a configuration using heavy metal in the base section was employed to give a rear c.g. location.) In one case, however, it was not necessary to use two models to obtain this breakdown of the pitching-moment data. By chance, a model flew with sufficient pitching amplitude, 12°, to cause the center of gravity to fly a measurably swerving course. From the curvature of the flight path, the lift-curve slope, C_{L_α}, was computed by the method of reference 15. The value of C_{N_α} was then obtained from the relation

$$C_{N_\alpha} = C_{L_\alpha} + C_D \tag{4}$$

which can be shown to hold accurately for small angles of attack from consideration of the vector diagram of aerodynamic forces. The measurement of C_{m_α} for this round by the methods outlined in the preceding paragraph, and the application of equation (3) for center of pressure gave the complete static-stability data from one round fired.

The measurement of dynamic stability goes back to the determination of the constant, k_1, in equation (1) by obtaining the best fit of a damped sine wave to the angle-of-attack data. In Appendix A, it is shown that k_1 is related to the dimensionless aerodynamic damping coefficients as follows:

$$\frac{k_1}{2} = -\frac{\rho_\infty A}{4m}\left[\left(C_{m_q} + C_{m_{\dot{\alpha}}}\right)\left(\frac{l}{\sigma}\right)^2 + C_D - C_{I_\alpha}\right] = -\frac{\rho_\infty A}{4m}[\zeta] \qquad (5)$$

Hence $C_{m_q} + C_{m_{\dot{\alpha}}}$ can be readily computed once k_1, C_D, and C_{I_α} are known. Of even more interest, however, is the fact that the group of coefficients in the bracket of equation (5), designated ζ for brevity, is the same group obtained by Allen in reference 16.[2] According to this reference, ζ must be negative to give a well-damped motion of a missile on re-entry. It must likewise be negative to give a convergent oscillation in the present test. Hence (except for possible differences in radius of gyration between test and flight), convergence of the motion in the test indicates convergence of the motion for re-entry. The rate of convergence, however, is not in general the same, since it is governed by multiplying factors involving air density, model frontal area and mass, etc., which are not the same either in algebraic form or in magnitude for range tests and re-entry flight. Hence, the combined group of dimensionless aerodynamic coefficients, ζ, represents the most general way of stating the dynamic characteristics of a configuration.

RESULTS AND DISCUSSION

The results to be presented will concern the force and moment characteristics and the boundary-layer transition characteristics of the test configurations. The former data can be presented and discussed briefly and in a straightforward manner because there are few points of interpretation involved. Consequently this will be done first. Following this, the boundary-layer transition data will be presented. As will be seen, this section will include a description of the shadowgraph evidence used to detect transition, a discussion of various factors possibly influencing the results, and some speculation as to what the test results might indicate for objects of larger scale.

Force and Moment Data

The force and moment measurements were made not so much with the idea of cataloging the characteristics of a wide range of configurations as with the idea of providing a few spot checks of the theoretical methods available. Thus, drag measurements were limited to four configurations at two Mach numbers; normal force and center of pressure, to two

[2]The similarity of form results from including the effect of deceleration in both cases. (Note the appearance in eq. (5) of C_D.) The effect of deceleration is to reduce the dynamic pressure, and therefore it is destabilizing with respect to pitching amplitude.

configurations at two Mach numbers; and damping-in-pitch measurements were limited to the basic configuration at one Mach number. These measurements, however, may indicate what can be expected from bodies of this category, and also the ability of the available theory to predict the individual characteristics.

Drag.- Total-drag coefficients of the round-nosed 60° cone, pointed 60° cone, hemisphere, and sphere were measured at Mach numbers near 4 and 8 and are plotted as a function of Mach number in figure 4. The round-nosed 60° cone and the pointed 60° cone have drag coefficients that are essentially equal. The drag coefficients of the hemispheres and spheres are substantially higher and nearly independent of Mach number over the test Mach number range.

A comparison of the experimental total-drag coefficients with theory is shown in figure 5(a) for the round-nosed cone, hemisphere, and sphere. Two methods of calculating total-drag coefficients were used; the method of reference 17, and a modification of the Newtonian impact theory of reference 18. The method of reference 17 consists of adding the wave drag of the spherical tip, from experiment, to the theoretical wave drag of the cone (from ref. 19) and subtracting the wave drag of the conical tip. Additional allowance is made for base drag and skin-friction drag. The modification of Newtonian impact theory consists of substituting the pitot-pressure coefficient, C_{p_t}, for the coefficient 2 in the expression for pressure coefficient as a function of flow deflection angle, θ_s. Thus we use

$$C_p = C_{p_t} \sin^2\theta_s \tag{6}$$

instead of

$$C_p = 2 \sin^2\theta_s \tag{6a}$$

This modification tends to give more nearly the correct pressure coefficients on the blunt portions of the body and becomes exact at the stagnation point of round-nosed bodies. Again allowance is made for base drag and skin-friction drag. Precise estimation of base drag and skin-friction drag is not required, however, since the major contribution to the total drag of these bodies is wave drag. The base pressure was therefore arbitrarily taken to be 0.3 of the free-stream static pressure, and a skin-friction coefficient of 0.0025 based on wetted area was arbitrarily selected. From these assumptions, the base drag coefficient at $M_\infty = 8.0$ becomes 0.016, and the skin-friction drag coefficient based on frontal area becomes 0.005, compared to an estimated wave-drag coefficient of 0.562 for the round-nosed cone and 0.915 for the sphere.

The calculations by the method of reference 17 give the drag of the round-nosed 60° cone within 5 percent. The drag estimated using modified Newtonian theory is too low for the round-nosed 60° cones by as much as 10 percent, and too high for the spheres by about 5 percent, although the agreement in the case of the former model seems to improve as Mach number is increased. The use of unmodified Newtonian theory, equation 6(a), gives estimates about 10 percent higher, and thus improves agreement with experiment for the round-nosed cone at the lower Mach number, but worsens agreement in the case of the sphere.

The total-drag data for the sharp 60° cones of this test are plotted in figure 5(b) along with the experimental drag curve for the 60° cone-cylinders of reference 10, which agree with the present measurements very satisfactorily. Of course, the exact conical-flow theory of reference 19 provides precise prediction of the wave drag for this model (ref. 10), but to test further the modified Newtonian theory, equation (6) was applied to this case. The result (including friction and base drag) is shown in the figure by the solid curve. It underestimates the measured drag by as much as 18 percent. Thus, in three comparisons, the modified Newtonian theory is found both to underestimate and overestimate drag, with a maximum discrepancy of 18 percent. Unmodified Newtonian theory is subject to errors of similar magnitude. The method of reference 17 appears somewhat more accurate for the limited cases to which it can be applied.

Static stability.- No presentation is made here of the values of C_{m_α} measured, since they would apply only for the particular center-of-gravity locations used. Instead, the quantities, C_{N_α} and x_{cp}, which specify the static stability for any desired center-of-gravity location are given.

Experimental values of C_{N_α} for the round-nosed 60° cone are shown in figure 6 and compared with theory. The normal-force-curve slopes fall somewhat below the value indicated by slender-body theory, 2.0, but this still gives the order of magnitude, even under these conditions of extreme departure from slenderness. The modified Newtonian theory tends to fall somewhat below the data as shown. Unmodified Newtonian theory would agree somewhat better. The theory for a pointed 60° cone (ref. 19) falls in the middle of the data for the two Mach numbers. To what extent this could be expected to continue for cones of different included angle and increasing amounts of bluntness is unknown.

Center-of-pressure data for the round-nosed 60° cone and the pointed 60° cone are given as a function of Mach number in figure 7. (Note that in the case of the pointed cone, square symbol, the theoretical value of C_{N_α} was used with the measurement of C_{m_α} to obtain the result shown.) In both cases, the center of pressure falls approximately 90 percent of the length from the nose. Prediction of the center of pressure of the

round-nosed cone by Newtonian theory is surprisingly accurate, within 3 percent of the length, in view of the discrepancies in prediction of drag. The result for the pointed cone is in very satisfactory alignment with conical flow theory, and provides confirmation for the following center-of-pressure equation for pointed cones with attached shock waves:

$$\frac{x_{cp}}{l} = \frac{2}{3}\left(1 + \tan^2\theta_c\right)$$

In the case of the hemispheres, no static stability measurements were made. However, it is of interest to mention that the center-of-pressure forces on the front face will fall at the center of curvature - that is, at the base. The bodies were designed with this expectation in mind, and their flight characteristics were very satisfactory, a proper nose-forward attitude being consistently maintained.

The above results indicate that there should be little difficulty in obtaining statically stable flight with bodies of this type at high speeds.

Dynamic stability.- Damping-in-pitch information was obtained from two round-nosed 60° cones at a Mach number of 4. Round 1 was fired in the wind tunnel (air off) and gave four angle-of-attack observations in one cycle of oscillation. Round 2, which is the one shown in figure 3, was fired in the underground range, and provided seven observations of angle-of-attack spread over 3.5 cycles. The data from these two rounds are summarized in the following table:

Round no.	Mach no.	x_{cg}/l, percent	Amplitude ratio per cycle	$C_{m_q} + C_{m_{\dot{\alpha}}}$ (exp.)	C_{m_q} (theory)	ζ (exp.)	ζ (theory)
1	3.98	70	0.78	-0.70	-0.23	-5.1	-2.0
2	3.91	70	.74	-.85	-.23	-6.2	-2.0

Considering the differences in the distribution and extent of the raw data, and the minimal definition of the oscillations, the agreement of the two results is fairly good. The agreement of Newtonian theory with experiment is not very satisfactory. The theory gives an estimate of C_{m_q} only, which is about one third as great as the measured values of $C_{m_q} + C_{m_{\dot{\alpha}}}$. The predicted value of ζ is likewise about one third as great as measured. The accurate prediction of ζ will be very difficult because ζ involves sums and differences of the aerodynamic coefficients and precision depends on extreme accuracy (or compensating errors) in the individual coefficients. Further investigation will be required to determine fully the adequacy of the theory. The measured coefficient, $C_{m_q} + C_{m_{\dot{\alpha}}}$, was negative, indicating a tendency to damp the motion. The

combined coefficient, ζ, was negative as well because the tendency for deceleration to destabilize the motion (C_D in eq. (5)) was, in this case, fully canceled by the damping due to plunging (C_{L_α} in eq. (5)).

At the time these measurements were made, it was not clear that the coefficients obtained would or would not lead to a well-damped re-entry flight. Therefore, the calculations described in Appendix B were undertaken to consider the flight of an example missile. Friedrich and Dore (ref. 20) had obtained equations for the pitching motion during re-entry of a body with zero aerodynamic damping and zero damping due to plunging. They considered only the effect of the variation in dynamic pressure, which damps the motion at the beginning but causes divergence to occur at low altitudes when q begins to decrease because of velocity loss. The envelope of a motion of this type is shown in figure 8 by the curve labeled "dynamic-pressure effect - aerodynamic damping = 0." Approximate equations developed in Appendix B were then applied to determine the contribution of aerodynamic damping, using experimental values of the damping coefficients. This led to the amplitude variation indicated in the figure as "contribution of aerodynamic damping." The resultant motion is then obtained by multiplying the ordinates of the two curves which leads to the curve labeled "total effect." The aerodynamic damping coefficients measured are found to be very beneficial at altitudes below 100,000 feet. They are, in fact, sufficient to overcome the tendency for divergence at low altitude.

Subsequent to these calculations, the linear equations of planar pitching motion during re-entry were solved with only minor approximations as reported in reference 16. Calculation of the motion envelope by the methods of that reference led to identically the same "total effect" curve as that given in figure 8. (See Appendix B.)

Boundary-Layer Transition

Transition to turbulence of the boundary layers on the test models was studied from the spark shadowgraphs. Because the boundary layers and disturbed-flow fields were thin, and because light refraction effects were strong, transition locations were not so immediately apparent in these shadowgraphs as in those of the slender bodies of reference 8. It was possible in most cases, however, to find evidence of the type of boundary-layer flow.

Evidence of turbulence.- It was found that boundary-layer turbulence on these bodies could produce one or more of at least four indications in the shadowgraph:

1. In some cases, the turbulence could be directly observed as in reference 8. This required a relatively thick boundary layer in a region

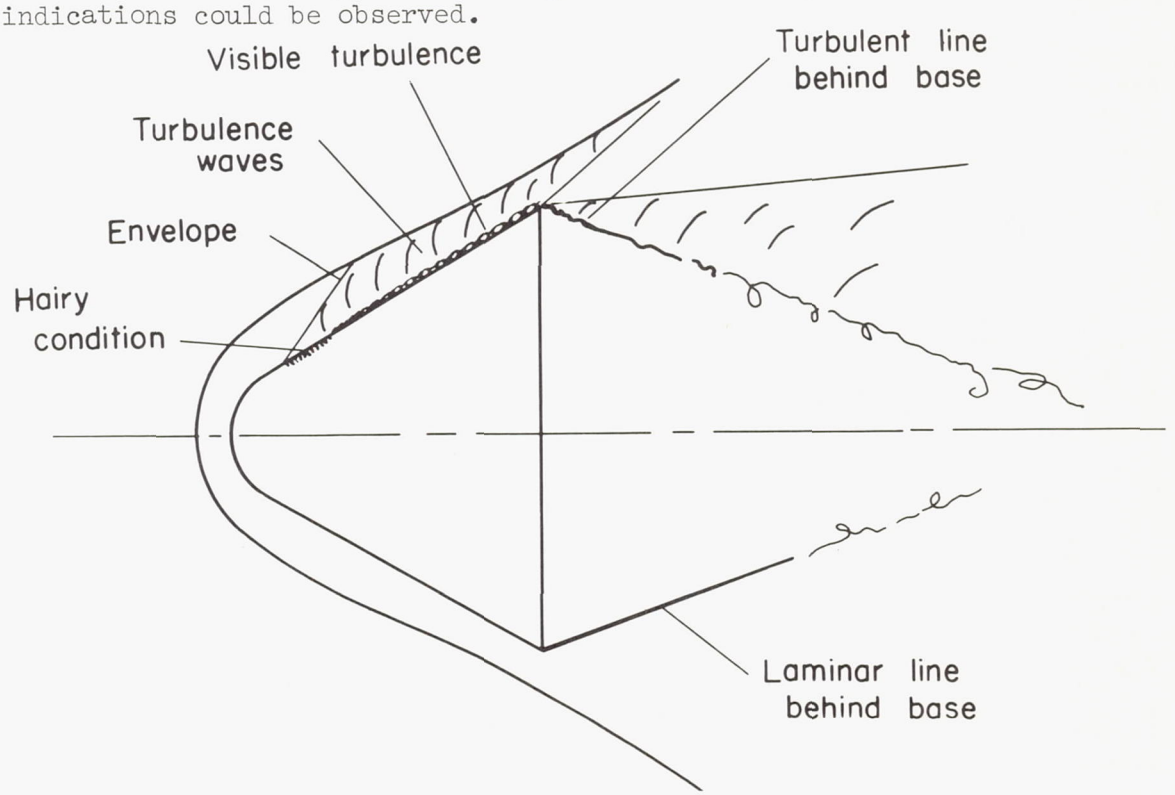
free of light distortion from the bow shock wave and was therefore usually limited to positions toward the back of the test bodies.

2. Where the turbulent boundary layer was very thin, the turbulent eddies frequently caused minute light filaments to be refracted into the model shadow, producing the impression of hairiness at the model edge.

3. Sometimes Mach waves produced by the turbulence could be seen well outside the boundary layer when the turbulence itself was not evident. The turbulence waves are of greater slope than body-fixed Mach waves. Sometimes they occur as isolated single waves in the case of bursts of turbulence. Other times, when transition is relatively steady, a field of turbulence waves will occur and it will be bounded by an envelope corresponding to a body-fixed Mach wave originating at the transition point.

4. The condition of the boundary layer behind the model base can frequently be determined from its appearance. The laminar layer gives a thin, smooth, steady line which can persist far behind the base, as in figures 9(a) and 9(d). The turbulent layer gives an indefinite, noticeably turbulent line which diffuses rapidly, as in figures 9(b) and 9(c).

These features are all indicated schematically in the accompanying sketch. In the course of the discussion, shadowgraph pictures from the test showing some of these characteristics will be introduced. Turbulence was considered to be present in a given case if any one of the above indications could be observed.



Round-nosed 60° cone.- Shadowgraph pictures typical of those obtained with the round-nosed 60° cones with Type I surface finish at a Mach number of 8.3 and a Reynolds number of 4.8 million, based on maximum diameter and free-stream air properties, are shown in figure 10. These pictures contain examples of two of the turbulence indications cited above. In figure 10(a) the shadowgraph sensitivity is low and, as a result, turbulence in the boundary layer is directly visible in the original negative as, for example, on the top surface starting at about midlength. In figure 10(b) the view of the surface is obscured because of higher sensitivity but a laminar line can be seen behind the base on the bottom meridian. Thus, it can be concluded that there is fully laminar flow on the bottom but not on the top.

This asymmetry in transition was noted for two models tested at this condition. One side was laminar throughout the flight, independent of angle of attack and regardless of whether the laminar side was at the moment windward or sheltered. On the other side, the boundary-layer flow off the base was consistently turbulent. This was taken as evidence of an influence of roughness on transition, since roughness was known to be almost certainly asymmetric (see, e.g., fig. 2(e)), whereas no other significant characteristic of the model or air stream was known to be persistently asymmetric.

Graphical presentation of the data from the model of figure 10 and one other model at a Mach number of 8.3 is given in figure 11. In part (a), the location of transition is plotted against angle of attack. Three kinds of symbols are employed. The circles without arrows indicate direct observation of transition to turbulence on the model or behind the base. The circles with downward-facing arrows indicate that transition occurred at some unknown location ahead of the base. The x's indicate the observation of turbulence waves, usually single waves from transient bursts of turbulence. The figure indicates that transition occurred on the model on a majority of the meridians observed. The effect of angle of attack appears to have been relatively moderate compared to that observed with the slender models of reference 8. Transition apparently began to move forward on both windward and sheltered sides at angles of attack above 2°.

The local Reynolds numbers at transition are presented in figure 11(b). For transition on the body, the Reynolds number was based on surface length to the transition point and air properties just outside the boundary layer at the transition point. To compute the air properties, the total pressure outside the boundary layer was assumed to be that behind a normal shock wave. The static-pressure distribution on the spherical portion was computed by modified Newtonian theory, equation (6a). The static-pressure distribution on the conical portion was approximated by smooth fairing between the terminal pressure of the sphere and the static pressure at the base, assumed to be that of a pointed cone. Even fairly large changes in the assumed pressure distribution would not

significantly alter the Reynolds numbers shown in figure 11(b). Behind the base, pressure was assumed equal to 1/10 free-stream static pressure, and this led to a value of local Reynolds number per unit length behind the base about 1/100 of that in the free stream. Thus, the sizable runs of laminar flow behind the base shown in figure 11(a) represent only slight increases in transition Reynolds number over the value for transition at the base. The local transition Reynolds numbers are of the order of 1 million or less.

Additional tests of this model configuration were made at a lower Mach number, near 4.0, and at a slightly lower Reynolds number, about 3.8 million based on diameter and free-stream conditions. Surface finishes of Type I (four models) and Type III (one model) were employed. A shadowgraph print of this model at $M_\infty = 4.0$ is shown in figure 12.[3] Notice that the background of tunnel-wall turbulence is absent for this case, since the test was made in still air, and there is a consequent gain in shadowgraph clarity. Also the lower Mach number increases the separation of the shock wave from the surface (which is somewhat contrary to the frequently expressed idea that Mach number has no influence on these flows). As a result, turbulence can be directly observed wherever it occurs, except on the spherical nose. Two other things were noted in the original negative. First, the hairy condition was seen where the boundary layer is thin, and this develops into visible turbulence as the boundary-layer thickness increases. Second, the turbulence behind the model base could be clearly seen both by looking at the edge of the base flow and by looking through the base flow.

Transition data collected from such pictures are presented in figure 13. Part (a) is comparable to figure 11(a) except that the angle-of-attack range extends up to 11° instead of 3°. It also differs in that transition was found to occur forward on the body in every case observed. The effect of angle of attack again appears to be small. Separating the data according to meridians gave a somewhat more systematic effect of angle of attack. The two or three observed points on any individual meridian showed in almost every case that increasing the angle of attack tended to move transition forward. Differences in roughness of the individual meridians caused them to have differences in transition location which are largely responsible for the vertical spread of the data in figure 13(a).

The data for the model with the Type III finish are shown by the filled symbols. No improvement in the extent of laminar flow was produced by the additional polishing. This may be due to the roughness remaining in the Type III finish after even the most careful polishing

[3]The bright lens-shaped image located about 1/2 inch behind and parallel to the model base is due to light from the shadowgraph spark reflecting off the model base.

(see figs. 2(d) and 2(c)). The roughness of the Type III finish tends to be three-dimensional, and hence may be as destabilizing to the laminar boundary layer as the scratches of the Type I finish at this test condition.

The local transition Reynolds numbers represented by the data of figure 13(a) were computed by the method previously described and are shown in figure 13(b). The most interesting point to be noted is that while the extent of laminar flow on this configuration was less at a Mach number of 4 than at a Mach number of 8, the local Reynolds number of transition was nearly the same at both Mach numbers, about 1 million.

Pointed 60° cone.- For comparison with the above data, limited tests were made of a pointed 60° cone with Type I surface finish at a Mach number of 8.3. The Reynolds number based on free-stream properties and diameter was 4.8 million, the same for the pointed cone as for the round-nosed cone at this Mach number.

A shadowgraph from this model test is shown in figure 14(a). Close examination of the model edge did not reveal any of the indications of turbulence cited earlier. In particular, the edge of the model appeared very clean and smooth, free of visible eddies or hairiness. Calculations were made to estimate the thickness of a turbulent boundary layer on this cone at the test conditions. The thickness computed to occur at the model base was 0.020 inch for transition at the tip and 0.017 inch for transition at midlength, thicknesses which should be easily visible in the pictures. It was therefore concluded that the absence of any visible turbulent boundary layer and the absence of any burst waves indicated that the boundary layer on the surface was fully laminar. Study of the wake boundaries did not, however, reveal any laminar line as distinct and persistent as in figure 10(b). A faint laminar line appeared intermittently, both near the base and farther back, which suggested that transition to turbulence occurred unsteadily along the boundary of the separated region.

To determine the appearance of these flow details in a case of definitely turbulent boundary layer, a cone was roughened by sandblasting with number 60 carborundum grit. One of the shadowgraphs of this cone in flight is reproduced in figure 14(b). Three differences from the pictures of the smooth cone were noted: Turbulence was visible at the model edge. No fine line whatsoever was visible at the edge of the base region. The minimum section of the wake was advanced from a mean position of about 1.4 diameters behind the base for the polished model to about 0.8 diameter behind the base for the rough model (see also fig. 9). These differences tended to support the conclusion that the smooth cone had fully laminar boundary layer.

The local slant-length Reynolds number of the cone at this flight condition was computed to be 6.7 million. The local Reynolds number of

transition would therefore be something in excess of 6.7 million. The angle-of-attack range of the data was from 0.9° to 3.8°, but the data were too limited to permit the evaluation of possible angle-of-attack effects.

Comparison of results from the rounded cone and the pointed cone showed that, for the particular conditions of these tests, rounding the cone reduced the average extent of laminar flow. This occurred even though the local Reynolds numbers were appreciably higher in the case of the pointed cone. The surface finishes of the two configurations were nominally the same. Nevertheless, the round-nosed cone gave indication of roughness effect in that transition differed on different meridians, whereas the pointed cone with Type I finish showed no tendency for roughness to cause transition. It is therefore indicated that the rounding increased the sensitivity of the laminar boundary layer to surface roughness as a contributing cause of transition.

Hemisphere.- Hemispheres were used as a second comparison configuration, thus giving the case of no rounding (pointed 60° cone), intermediate rounding (round-nosed 60° cone), and full rounding (hemisphere) to be compared. Tests of hemispheres with a Type I surface finish were made at the two basic Mach numbers, 4 and 8.3, and at free-stream Reynolds numbers based on diameter comparable to those of the round-nosed cones.

The shadowgraph pictures of the hemispheres at the higher Mach number were very difficult to interpret. One of them is shown in figure 15(a). The boundary layer on the surface was not clearly visible, but in the heavily exposed pictures, the model edge was seen to be hairy, to within 7° of the stagnation point in one picture, corresponding to a transition Reynolds number of about 20,000. The appearance of the boundary layer behind the model base was somewhat puzzling. It seemed to have laminar characteristics for a short distance (0.1 or 0.2 of an inch) before becoming distinctly turbulent. This may indicate an effect of strong expansion (along the sphere) of the type observed and discussed by Sternberg in reference 21 for the expansion at the corner of a 60° cone-cylinder. The relative turbulence will be decreased by rapid expansion if the turbulent velocity fluctuations grow, as would be expected, at a smaller rate than the velocities in and at the edge of the boundary layer. If this is the correct explanation for the apparent laminar flow just behind the model base, it suggests the possibility that laminar or intermediate heat-transfer characteristics might be occurring toward the rear part of the hemisphere. This suggests an interesting topic for further research, a test of the heat transfer on a sphere with turbulence induced near the stagnation point.

For contrast with the above model test, a hemisphere roughened by sandblasting was tested, and shadowgraphs like figure 15(b) were obtained. While the hairy condition at the model edge was somewhat intensified, and

the length of laminar line behind the base was somewhat reduced, the main impression to be derived from comparing these pictures with those of the smoother model was that they were substantially the same.

Tests at the lower Mach number of 4 of the 214° spherical segment model (fig. 15(c)) gave definite evidence (hairiness and visible turbulence) of turbulence on the front face at locations as far forward as within 40° of the stagnation point. The local Reynolds number at this point was 0.8 million. Because of optical distortion, it could not be determined how far ahead of this point transition took place. Toward the back of the model, the apparent intensity of turbulence decreased, but the flow coming off the model base remained in this case definitely turbulent.

Comparison with earlier data from slender-model tests.- At this point, it was apparent that transiton was occurring at far lower Reynolds numbers on the round-nosed models than on slender pointed models tested under similar free-stream conditions (refs. 8 and 22). The slender models had been able to retain laminar boundary layers with appreciable two-dimensional roughness present - orders of magnitude greater than that on the present models. The reasons for the relatively poor performance of the present round-nosed models in retaining laminar boundary layer were naturally the subject of considerable speculation. As was discussed in reference 13, one aspect of the flow on nonslender bodies of this type which seemed significant was the compression to surface Mach numbers much lower than free-stream Mach number. From the viewpoint of laminar stability theory (ref. 23), the large regions of subsonic flow on the round-nosed bodies could not be completely stabilized by cooling, even if the disturbances were restricted to the more favorable, two-dimensional kind. Experimentally, it had been shown (ref. 22) that at low wall temperature, reducing the Mach number at the boundary-layer edge increased the sensitivity of the laminar boundary layer to roughness-induced transition. For these reasons, attention was focused on the low surface Mach numbers occurring on the test bodies as a primary factor causing early transition. Another thing that aroused some interest was the thickness of the boundary layers on these bodies. The occurrence of roughness effects on relatively smooth surfaces seemed consistent with the expectation that the boundary layers would be very thin. Therefore, calculations of boundary-layer thickness were undertaken. Finally, unusual aspects of the flow over these bodies were considered to see if some additional destabilizing influences could be found. Several such influences will be discussed subsequently.

Because it was suspected that the low values of local Mach number were instrumental in causing early transition, it was desired to test a body with higher local Mach numbers, but still with a fineness ratio comparable to that of the other bodies tested. This led to the tests described below.

Pointed ogives.- A model was designed to have a minimum surface Mach number of 2 at a free-stream Mach number of 4. This, of course, required that it be pointed. Continuous expansion along the surface to a Mach number of 2.3 at the base was provided. The resulting model was the pointed ogive shown in figure 1(c). Two of these were prepared, one with Type I finish and the other with Type II. Since the supersonic free-flight wind tunnel was by then shut down for modifications, the tests of this model were made in the underground range and were limited to a free-stream Mach number of 4. The Reynolds number based on diameter was the same as in the earlier tests at this Mach number.

The results obtained are shown in figures 16 and 17. Figure 16(a) shows the model with Type I surface and shows bursts of turbulence (as indicated by the burst waves) occurring very far forward. Figure 16(b) shows the model with the Type II surface. It is free of turbulent burst waves, but shows very fine-grained turbulence beginning at about one fifth the length from the nose. (This latter picture was obtained at reduced shadowgraph sensitivity to reduce the distortion due to the bow shock wave. The method used to reduce the sensitivity was to bring the film very close to the plane of flight, within about 2 inches.) The data from the two rounds are presented graphically in figure 17. Since no angle-of-attack effects were noted, the distribution of observed transition points is presented according to the method of references 8 and 24. The number of cases in which a given body station is found turbulent, n_T, divided by the total number of observations made, N, is plotted as a function of body station. The mean location of transition is seen to have been relatively near to the tip where the relative accuracy of determining the transition location is poor. The difference shown in the mean location of transition on the two models is therefore not believed to be significant.

The reasons why these models failed to retain laminar flow were not clear at the time but, subsequently, a correlation of the roughness necessary to cause transition as a function of local Mach number showed that this test was still in the region where roughness controls transition. This point will be further discussed in the section on "Comparison of Roughness Height to Boundary-Layer Thickness."

Round-nosed ogive.- To obtain additional information on the effects on transition due to rounding a pointed body, a round nose was applied to the pointed ogive. The nose diameter was selected to give a low Reynolds number layer thicker than the boundary layer, according to the argument of reference 6. A sine-wave rounding was employed to provide continuous first and second derivatives at the juncture. A shadowgraph of the round-nosed ogive is shown in figure 18, and the transition locations read are compared in figure 19 with those of the pointed ogive. The effect of rounding, in this instance, was to increase the extent of laminar flow as predicted in reference 6. It is to be noted, however, that in the earlier case of the 60° cone at a Mach number of 8, rounding

reduced the extent of laminar flow. Thus, depending on particular factors, rounding may or may not increase the extent of laminar flow. It appears that effects of rounding, such as changes in local Mach number and pressure distribution, can be as important as the effect on local Reynolds number and must therefore be considered.

Comparison of the pointed and round-nosed ogives on the basis of local transition Reynolds number is made in figure 20, which is like figure 19 except that the body stations are now represented by their local Reynolds numbers. This presentation inverts the relation between the pointed and round-nosed ogives - the round-nosed models show slightly lower average Reynolds number of transition. This indicates the presence of some moderately adverse effects of rounding.

A comparison of round-nosed ogives with Type II and Type III surfaces is given in the figure. The two surfaces gave almost the same transition pattern. Rather than indicating no effect of roughness, this indicates (more generally) that the two surfaces are of equivalent roughness.

Round-nosed 30° cone.- In order to investigate a case intermediate in fineness ratio between the preceding bodies and the very slender bodies of references 8 and 22, the spherical-nosed 30° included-angle cone of figure 1(c) was tested in the underground range. The Mach number was 4.3, the Reynolds number based on free-stream properties and diameter was 4 million, and the surface finish was Type II. Shadowgraphs are presented in figure 21.

Transition to turbulence still occurred relatively early. This can be seen in the shadowgraphs both from visible turbulence and burst waves. The data read from the shadowgraphs are presented in figure 22, where observations from the four individual meridians observed are kept separate and denoted right, left, top, and bottom. Apparently, some systematic differences between the transition on individual meridians occurred, although these differences were not so pronounced as in the case of the round-nosed 60° cone. In the present case, for example, the performance at zero angle of attack was best on the right-hand meridian, worse by a factor of 3.5 on the left, and intermediate on top and bottom, possibly because of microscopic differences in smoothness of these meridians.

The effect of angle of attack shown in this figure seems to be generally similar to that of figures 11 and 13, namely, a moderate effect, with transition tending to move forward on both windward and sheltered sides as angle is increased. It is thought that in the case of more extensive laminar flow, a stronger effect of angle of attack might be observed on this body.

The local Mach number occurring on this body just ahead of the base was estimated to be near 2.0 from the slopes of Mach waves visible in

the shadowgraph. The local Reynolds numbers at transition, based on wetted length and estimated air properties outside the boundary layer, were again of the order of 1 million.

Comparison of Roughness Height to Boundary-Layer Thickness

The roughness-height data described in the section on surface roughness are not of themselves sufficient to describe the roughness conditions of these tests, but must be considered in relation to the boundary-layer thicknesses on the test models. In reference 13, a roughness parameter to relate roughness height, h, to laminar boundary-layer thickness, δ, for cases of distributed surface roughness of uniform height on a flat plate was proposed. Since this parameter was only briefly mentioned in reference 13, it will be further treated in this section, with the objective of applying it to the correlation and interpretation of the present test results.

Pointed bodies.- In the case of a pointed cone or sharp-edged flat plate with uniform surface roughness, a difficulty arises in attempting to specify a characteristic value of h/δ, since this ratio will vary from infinity at the leading edge to values generally less than 1 near the base. Therefore, the specification of h/δ must either be arbitrary, as in references 8 and 25, or in the form of a graph giving the distribution of h/δ. For flat plates and cones, however, it is possible to identify a parameter which specifies the relationship of roughness to laminar boundary-layer thickness for the entire surface. To find this parameter, first note that on the flat plate,

$$\frac{\delta}{x}\sqrt{R_x} = C \tag{7}$$

where C is constant over the surface of the plate, but is a function of the boundary-layer-edge Mach number and the ratio of wall temperature to boundary-layer-edge temperature. In order to make it possible to use the theoretical results of Van Driest (ref. 26) for the constant C, the boundary-layer thickness is defined throughout this report as the distance from the surface at which $u/u_1 = 0.995$. From equation (7), then, it follows that

$$\frac{h}{\delta} = \frac{h}{Cx}\sqrt{R_x} = \frac{h}{C}\sqrt{\frac{\rho_1 u_1}{\mu_1 x}} \tag{8}$$

so that h/δ is a function of the Reynolds number per unit length, $\rho_1 u_1/\mu_1$, and the distance from the leading edge, x. Equation (8) can be written

$$\frac{h}{\delta} = \left[\frac{\rho_1 u_1 h/\mu_1}{C(\rho_1 u_1 x/\mu_1)}\right]\sqrt{R_x} \tag{9}$$

or

$$\frac{h}{\delta}\sqrt{R_x} = \frac{R_h}{C} \tag{10}$$

The right side of equation (10) is seen to be constant for flat plates of uniform roughness and a given Reynolds number per unit length. By the same token, $(h/\delta)\sqrt{R_x}$ is seen to be a function of the Reynolds number per unit length and the roughness amplitude, but is constant over the surface.

For cones, equation (10) must be modified by the Hantzche and Wendt factor, $\sqrt{3}$, to account for the reduced rate of boundary-layer growth on cones. It becomes

$$\frac{h}{\delta}\sqrt{R_s} = \frac{R_h}{C}\sqrt{3} \tag{11}$$

where C is evaluated from flat-plate calculations for the Mach number and static air temperature at the boundary-layer edge. The Reynolds number per unit length is also evaluated at the boundary-layer edge.

For curved bodies, $(h/\delta)\sqrt{R_s}$ must, for precision, be computed from estimates of δ which take into account the effect of pressure gradient. The roughness parameter will now depart somewhat from a constant value. The variation, however, will not be large for moderately curved, pointed three-dimensional bodies of any fineness ratio, which do not depart too far from conical shape. The ogive of the present investigation was such a case. To compute $(h/\delta)\sqrt{R_s}$ for this body, the boundary-layer thickness distribution was first calculated by the method of Cohen and Reshotko (see refs. 27 and 28 and Appendix C). The Reynolds numbers, R_s, based on local properties outside the boundary layer and surface length were calculated using shock-expansion theory. The roughness height, h, was taken to be 10 microinches. Combining these data gave the roughness-parameter distribution shown in figure 23. As anticipated, a nearly constant value of $(h/\delta)\sqrt{R_s}$ is obtained.

Correlation of critical-roughness data for pointed bodies.- Use will now be made of the above roughness parameter for studying the roughness to boundary-layer-thickness aspects of the present and other tests. Critical values of the roughness parameter will be defined as the values above which roughness begins to control the Reynolds number of transition. For present purposes, if roughness caused transition to occur at Reynolds numbers of the order of 1 to 2 million, it was considered that the roughness parameter was higher than critical. If laminar flow persisted to

Reynolds numbers of the order of 10 to 30 million, it was considered that the roughness parameter was below the critical value. Based on these definitions, data from the present test and other sources were collected to define the variation of the critical roughness parameter with Mach number shown in figure 24 for wall-temperature ratios, T_w/T_1, of the order of 1. The three points at Mach numbers of 3.5, 4.9, and 6.9 were obtained by cross-plotting data from figure 8 of reference 13. The points selected as critical were the points at which an increase in roughness started to move transition forward. The two upright triangles are data from the present investigation. The pointed 60° cone at a free-stream Mach number of 8.3 had a surface Mach number of 3.0 and fully laminar flow to a local length Reynolds number of about 7×10^6, so the surface is considered smoother than critical (arrow up). The pointed ogive at a free-stream Mach number of 4 had a local Mach number of 2 ahead of transition and showed early transition, so the surface is considered rougher than critical (arrow down). The cluster of data at Mach numbers between 1 and 3 represents a broad range of test conditions but, nevertheless, demonstrates considerable consistency with the above data. The data of Sternberg (ref. 29) and that of Low (ref. 5) each give a point on the critical roughness curve which is in good alignment with the data for higher Mach numbers. Additional points from the data of Sternberg (at a Mach number of 2.7), and Rumsey and Lee, reference 30, (at a Mach number of 2.9) represent conditions of extensive laminar flow and fall in the region of smoother-than-critical surfaces. The data of Czarnecki and Sinclair, reference 31, and Czarnecki, Robinson, and Hilton, reference 32, are again for smoother than critical surfaces at local Mach numbers near 1.5, and indicate a somewhat higher position for the critical roughness curve than would be deduced from the other data. However, the large differences in the conditions of these various tests with respect to roughness types, pressure gradient, wall temperature ratios, and facilities do not lead to the expectation of quantitative agreement. Finally, the data obtained by Luther (ref. 33) in investigating the amount of roughness needed to trip the boundary layer near a model tip show, as would be expected, that the roughness required to bring about immediate transition at a Reynolds number of 94,000 is somewhat greater than that required to influence transition initially. Nevertheless, the trend of variation with Mach number in his data is very similar to that shown by the solid curve. It appears that the critical roughness parameter increases rapidly with increasing local Mach number at supersonic Mach numbers above 2.

The significance of figure 24 in relation to the present test results is evident. Although the free-stream test Mach numbers were high, the local surface Mach numbers were always less than 3 and usually less than 2. This put the tests into a region where surface roughness effects were difficult to avoid. Figure 24 indicates the desirability of obtaining a more precise definition of the critical values of the roughness parameter in the low surface Mach number region where low-fineness-ratio missiles are required to operate.

Round-nosed bodies.- A calculation of the boundary-layer thickness development on the bodies with hemispherical noses (by the method of refs. 27 and 28 as discussed in Appendix C) showed that within 30° angular displacement from the stagnation point, the boundary-layer thicknesses were not represented even approximately by equation (7). In fact, the boundary layer on a blunt body has finite thickness initially, and from the stagnation point to the sonic point δ is very nearly constant, as is indicated by the calculated thicknesses in figure 25. This suggested that the parameter h/δ_{sp} would satisfactorily represent roughness effects in this region, and this parameter was adopted for use with the round-nosed bodies.

The calculated ratios of nominal roughness height (taken to be 10 microinches[4]) to boundary-layer thickness on the stagnation point are tabulated below for the hemispheres and round-nosed cones:

Body	M_∞	d_n, in.	$\rho_\infty u_\infty d_n/\mu_\infty$, million	δ_{sp}, in.	h/δ_{sp}
Hemisphere	3.8	1.73	3.9	0.00121	0.008
	8.0	1.65	4.5	.00187	.005
Round-nosed 60° cone	4.0	.57	1.3	.00072	.014
	8.3	.57	1.6	.00103	.010
Round-nosed 30° cone	4.3	.25	.6	.00048	.010

The values of h/δ_{sp} computed are of the order of 1 percent, and, judging from the observed asymmetry of the boundary-layer transition, roughness of this amplitude was sufficient to influence transition.

Effect of scale.- The maintenance of equal h/δ_{sp} provides a basis (which is not as yet supported by experiments) for defining round-nosed bodies of equivalent roughness but different physical size and Reynolds number. The computation of an equivalent roughness does not, however, give any information as to the effect on transition Reynolds number of increasing the flight Reynolds number at a constant roughness condition. This information can be provided thus far only by tests or flights at the desired Reynolds number. Nevertheless, it is interesting and informative to compute equivalent surface roughnesses to those of the present tests for cases of larger scale bodies and increased Reynolds numbers.

[4]The stagnation points of these models were the hardest places to polish smooth. All the models examined had several three-dimensional pits of the order of 10 microinches deep, within a radius of 0.01 inch of the stagnation point.

Laminar boundary-layer thickness is, in general, directly proportional to physical size, and inversely proportional to the square root of Reynolds number. Any characteristic dimension may be used as a measure of the size, and any single Reynolds number may be used to identify the distribution of local Reynolds numbers that exist on a body of particular shape. In the following discussion, the nose diameter, d_n, will be used to specify size, and the free-stream Reynolds number based on nose diameter, R_n, will be used along with the body shape to specify the distribution of Reynolds numbers. Then, for given, fixed conditions of Mach number and wall-temperature ratio,

$$\frac{\delta}{d_n}\sqrt{R_n} = f\left(\frac{s}{l}\right) \tag{12}$$

and

$$\frac{h}{\delta_{sp}} = \left(\frac{h}{d_n}\right)\frac{\sqrt{R_n}}{f(s/l)_{sp}} \tag{12}$$

For two bodies of the same shape (but different size and Reynolds number) to have the same value of h/δ_{sp} then

$$\left[\frac{h}{d_n}\frac{\sqrt{R_n}}{f(s/l)_{sp}}\right]_1 = \left[\frac{h}{d_n}\frac{\sqrt{R_n}}{f(s/l)_{cp}}\right]_2 \tag{14}$$

where the subscripts 1 and 2 identify the two conditions of scale. If Mach number and wall-temperature ratio are the same in cases 1 and 2, then

$$\left(\frac{h}{d_n}\sqrt{R_n}\right)_1 = \left(\frac{h}{d_n}\sqrt{R_n}\right)_2 \tag{15}$$

Thus, to make a numerical comparison, consider a body 20 inches in nose diameter (60 inches in base diameter) having the shape of the round-nosed 60° cone, in flight at $M_\infty = 8$ with a free-stream Reynolds number based on nose diameter of 15 million, and find the roughness of this body which is equivalent to the 10 microinches used in the present test.

$$\frac{h}{20}\sqrt{15\times10^6} = \frac{10/10^6}{0.57}\sqrt{1.6\times10^6}$$

$$h = 115 \text{ microinches} \approx 0.0001 \text{ inch}$$

That is, 0.0001-inch roughness on the large-scale body provides equal h/δ_{sp} to that experienced in the present test.

In figure 25, the effect of increasing Mach number on initial boundary-layer thickness on round-nosed bodies is shown. The calculated initial thickness (ignoring dissociation) for M = 20 is about 3.5 times that for M = 3.8. Hence, one might expect that the smoothness requirement on round-nosed bodies might be relaxed by increasing Mach number as well as by increasing scale. For the conditions of scale used in the above example, the roughness equivalent at M = 20 to that of the present test at M = 8 would become 0.00024 inch.

The situation for scaling roughness on sharp-edged flat plates and pointed cones differs fundamentally from that for round-nosed bodies in that the flat plate has no characteristic dimension other than the roughness height (provided that transition occurs within the length of the plate) whereas the round-nosed body has as a characteristic dimension, the diameter of the nose, on which the boundary-layer thickness depends. Thus, for the round-nosed bodies, the scaling relationship suggested (eq. (15)) depends on roughness height, nose diameter, and Reynolds number; while the roughness parameter expression for flat plates (eq. (10)) depends only on roughness height and Reynolds number per unit length. It would be expected that for flat plates, cones, and perhaps approximately for other pointed bodies, that $(h/\delta)\sqrt{R_s}$ should be kept constant to give equivalent roughness, and that therefore

$$R_{h_1} = R_{h_2}$$

is the roughness scaling law.

When it is desired to compare the roughnesses of cones of different included angles, or to correlate cone and flat-plate data, then it is essential that the Reynolds numbers be based on air properties at the edge of the boundary layer. If it is desired only to compare cones of identical geometry but of different size and Reynolds number, then free-stream properties may be used, since the ratio of free-stream to local air properties will be the same if the Mach number is the same. Thus, to convert the roughness of the pointed 60° cone from the scale tested to the same frontal area and flight condition as the preceding example (60-inch base diameter and 45 million Reynolds number based on free-stream air properties and base diameter)

$$\frac{45\times10^6}{60}\,h = \frac{4.8\times10^6}{1.73}\left(\frac{10}{10^6}\right)$$

$$h = 37 \text{ microinches}$$

Thus, the relaxation of the smoothness requirement with increase in scale may be less rapid for pointed bodies than for round-nosed bodies.

These scaling methods have been discussed at some length because the question of proper ways of scaling roughness is a fundamental one for studying the transition of boundary layers on large-scale objects from small-scale tests. It is emphasized that the procedures used above are purely theoretical and have not been investigated experimentally.

Other Causes of Boundary-Layer Instability

Attention has been given above to surface roughness as a contributing cause of transition in these tests, and it appears that roughness had a considerable influence on the results obtained. Other factors, however, undoubtedly contributed to causing transition, and these will now be discussed.

Pressure gradients.- Pressure distribution is well known to have important effects on boundary-layer transition. This subject has received considerable attention in the literature (see refs. 8, 22, 25, 34, and refs. noted therein). It is therefore necessary to consider the pressure fields about the present models.

The round-nosed 60° cones of the present tests are similar to the 80° included-angle round-nosed cone of reference 9. In figure 26, taken from reference 9, it may be seen that there is a minimum pressure just aft of the spherical nose, followed by a fairly quick recovery toward the pressure predicted for a sharp 80° cone. Unpublished data from the Ames low-density wind tunnel and the data of figure 26 indicate that as the test Reynolds number increases, the pressure minimum and subsequent recovery become more pronounced. The present tests were made at still higher Reynolds numbers so that considerable pressure rise may be presumed.

Additional evidence of pressure rise along the conical portion of the round-nosed 60° cone was obtained from the shadowgraphs. It was noted that the bow-shock-wave profiles were peculiar in that they showed a region of reverse curvature - concave outward. This can be seen in figures 10, 12, and 21. The reverse curvature was appreciable, and could not have been caused by optical distortion since the contour of the bow-wave leading edge is recorded by undisturbed light passing through the free-stream air just ahead of the shock wave. In the region of reverse curvature, the wave slope is increasing, and the wave strength must likewise be increasing. The increase in wave strength is attributed to compression disturbances feeding up from the body surface, and is therefore believed to reflect the condition of rising pressure on the body surface. The forwardmost influence of the conical surface on the bow wave has been traced in some shadowgraphs of rough models from preliminary tests by

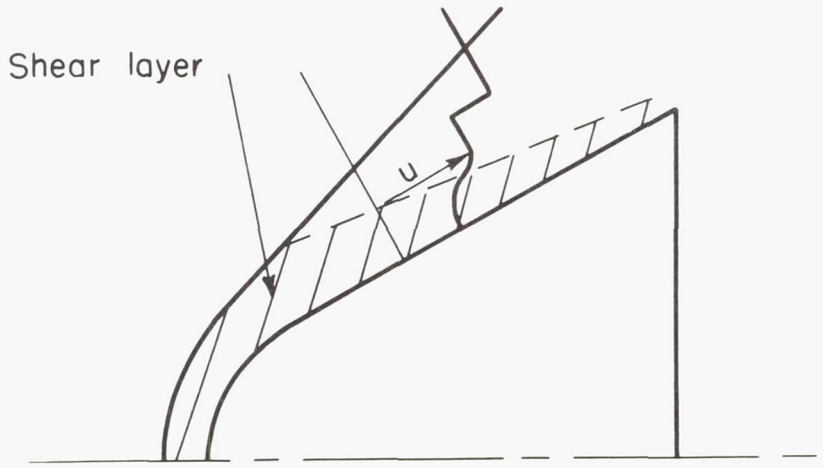
following Mach lines attached to body-fixed roughness. At the intersection on the bow wave of a Mach wave from the body tangent line, the bow-wave profile immediately became straight. Very shortly thereafter, the concave profile began. This indicates that the rising pressure on the body surface began almost immediately behind the tangent line.

For purposes of estimating the pressure rise quantitatively, Newtonian theory was of no value, since it fails to predict the occurrence of either the overexpansion or the pressure rise. If centrifugal force effects are included by use of one of the highly approximate procedures available, the overexpansion can be introduced, but it will be followed by a discontinuous pressure rise and constant pressure on the conical surface. As a more reliable alternative, use was made of sphere pressure distributions from reference 3 and conical pressure data from reference 19 to estimate the pressure rise. Application of this data to the case shown in figure 26 would, for example, indicate a minimum value of C_p at the tangent point of 0.39 $C_{p_{max}}$, a value that appears to be in good alignment with the pressure data of figure 26 for the conical part of the model at the highest Reynolds number. When this method of estimation is applied to the present round-nosed 60° cone at $M_\infty = 3.8$, it is found that the pressure coefficient at the tangent line (based on free-stream dynamic pressure) is lower by 0.16 than the pressure to which the flow will ultimately recover on the cone. Converting this result to the form $\Delta p/p_{min}$ (the pressure rise along the surface divided by the minimum pressure along the surface) yields a value of 0.32. According to reference 22 (which was concerned with slender bodies), this should be enough to assure transition if the local Mach numbers are supersonic. It is not known that this full pressure rise occurred within the length of model, or to what extent the pressure rise that did occur influenced transition. As was noted earlier, the hemisphere and ogive models with continually favorable pressure gradients had transition Reynolds numbers at $M_\infty = 4$ comparable to the round-nosed cones.

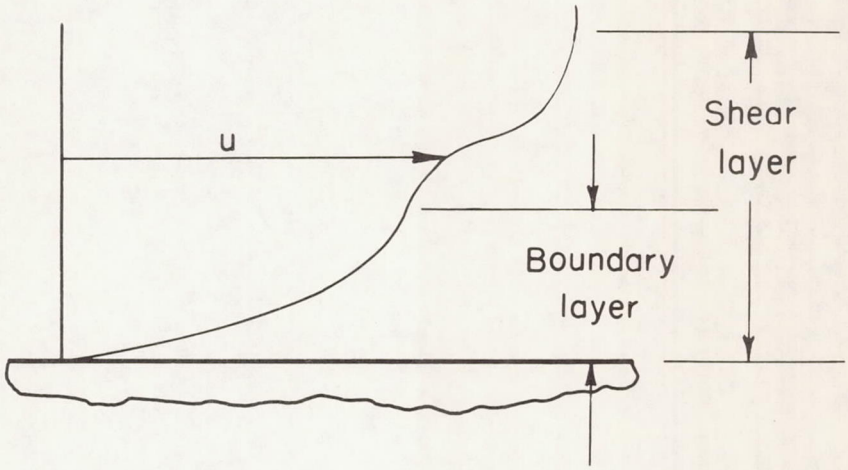
Similar estimates were made of the pressure rise on the round-nosed 60° cone at $M_\infty = 8$ by extrapolating the sphere pressure coefficients of Stine and Wanlass to this Mach number. A possible pressure-rise coefficient of about 0.17 above minimum was calculated. It is interesting that this value is just below the critical value of $\Delta p/p_{min}$ given in reference 22 and that, for the test at this condition, laminar flow to the base was obtained on some meridians. Calculation of the pressures on the round-nosed 30° cone at $M_\infty = 4.3$ indicated that the terminal pressure on the spherical nose was slightly greater than that of the pointed cone, which would lead to the expectation of favorable pressure gradient downstream of the tangent point. This, however, is not consistent with the fact that reverse curvature of the bow shock wave was observed, which indicates that some pressure rise must have occurred. It further indicates that more experimental and theoretical work can be profitably devoted to investigating flow fields about bodies of this type.

It is suspected that the unfavorable pressure distributions of the round-nosed cones contributed to the early transition observed, but there is also evidence from comparison with results from the other test configurations that other causes of laminar instability were present and probably of overriding importance.

Shear-layer effects.- In addition to its effect on pressure distribution, the flow field outside the boundary layer may also assume importance in another way which will now be discussed. Behind the convex bow wave lies a region characterized by extreme variations in total pressure from one streamline to the next. The region in which these large variations occur is quite nicely defined in the shadowgraphs of the round-nosed 60° cone. As was pointed out above, the juncture of the first Mach wave from the cone with the bow wave appears to mark the end of the convex portion of the bow wave. The streamline which passes this point lies on a sudden change in density gradient normal to the local flow direction. Since the shadowgraph is sensitive to changes in density gradient, this streamline becomes a visible line in the shadowgraph and shows up clearly in figure 10(a). Outside this line the total-pressure variations are relatively gradual as evidenced by the comparative straightness of the bow wave. The inner region is of interest because of the velocity profiles which can be expected to occur there. Where the total pressure varies rapidly across the streamlines, a region of nearly constant static pressure is characterized by large velocity gradients and consequently by the existence of appreciable shear. This leads to the term "shear layer," which will be used in the remainder of this discussion. Layers of this kind have been discussed by Moeckel (ref. 6) and Ferri and Libby (ref. 35). A velocity profile in a shear layer is shown in the following sketch as it would appear in inviscid flow, and is qualitatively like that between two parallel jets of differing velocities. Near the nose



of such a body in viscous flows, the boundary layer superimposes its velocity distribution onto that of the preceding sketch. The resulting velocity profile might then be like that sketched below. In this case, little interaction between boundary layer and shear layer would be anticipated provided both remained laminar. However, it should be noted that this velocity distribution contains two inflection points, one where the boundary layer meets the shear layer and one in the shear layer itself. It is expected that this velocity distribution would be unfavorable to continued laminar flow.



It is important to note that transition to turbulent flow can occur in the shear layer well outside the boundary layer. This phenomenon may be seen clearly in the shadowgraphs of figure 21 of the present paper, and the occurrence of this transition is indicated in figure 22. Another feature of this type of flow is illustrated in figure 27 wherein the models are open tubes. The flow on the outside is essentially two-dimensional. There is a difference between the two models in the leading-edge thickness. In the case of the thin-leading-edge model, figure 27(a), the boundary-layer growth after transition is relatively slow compared to that for the thick-leading-edge model, figure 27(b). The distance from the transition point has been marked off in inches for convenience in comparing boundary-layer thicknesses at corresponding stations. In the latter case a shear layer (visible in the shadowgraph) has been produced by the thick leading edge, and the turbulence quickly envelopes this layer, thereby producing a thicker than normal boundary layer. This is probably beneficial in that the heat transfer and skin friction of the thick turbulent boundary layer should be lower than for a turbulent boundary layer of normal thickness. Abnormal thickening of the turbulent boundary layer was also observed on the original negatives of the round-nosed 60° cone. The turbulent boundary layer in these pictures apparently envelopes the complete shear layer almost immediately after transition.

Air-stream turbulence.- In the present tests, as in all investigations of boundary-layer transition, the effects of air-stream turbulence should be considered. In the case of the data for $M_\infty = 4$ the tests were conducted in still air. The Mach number 8 data on the other hand were obtained with a countercurrent air stream of unknown, but large, turbulence. When the turbulence velocities are compared to the sum of the air and model velocities, the "percent turbulence" is only about one fourth as great as when compared to the air velocity alone. However, in the subsonic region behind the detached bow wave of round-nosed models the compression yields a fivefold increase in turbulence level. This can be seen by considering the flow through a normal shock wave where, for continuity

$$\rho_\infty u_\infty = \rho_1 u_1$$

By the normal-shock relations for $\gamma = 1.4$,

$$\frac{\rho_1}{\rho_\infty} = \frac{6M_\infty^2}{M_\infty^2 + 5}$$

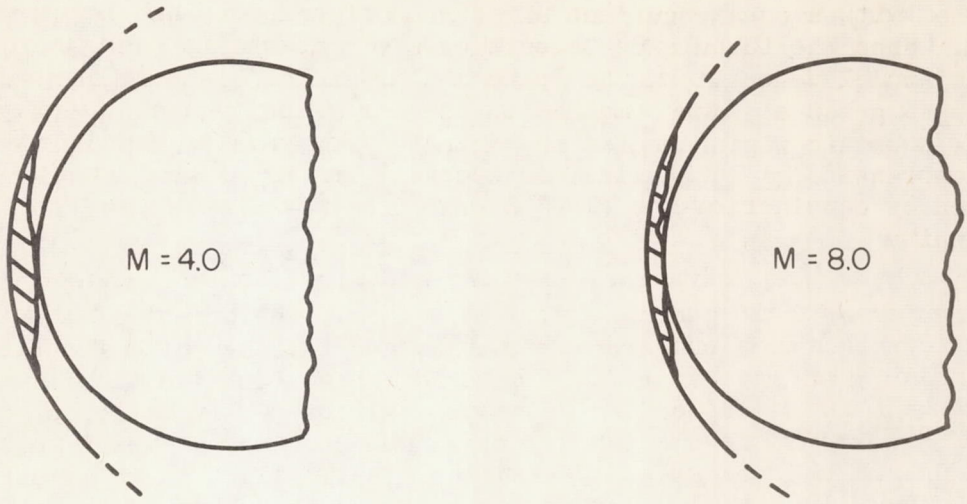
Hence, at $M_\infty = 8$

$$\frac{\rho_1}{\rho_\infty} = \frac{u_\infty}{u_1} = 5.57$$

The resulting increase in percent turbulence probably contributes to the difficulty in obtaining laminar flow under these test conditions.

Görtler instability.- In reference 36, H. Görtler has treated the case of laminar flow over a concave wall and finds this flow configuration to be favorable to the production of vortices lying along streamlines. In a lecture on laminar boundary-layer instability at Stanford University in March 1956, Görtler stated that this phenomenon is not limited to boundary-layer flows. Rather, the conditions necessary for it to occur are: (a) streamline curvature and (b) velocity gradient positive toward the center of curvature. As pointed out by Görtler these conditions are met near the stagnation point of a blunt body.

In the following sketch, the approximate boundaries of the region of vortex amplification are shown. (The shock-wave shapes and positions for this sketch were obtained from the shadowgraphs of the present test.)



The shaded area represents the region in question. The outermost streamline involved is probably the one that passes through the point at which the maximum flow deflection occurs in the bow wave and the sketch is based on this assumption. It can be seen that streamlines inside this point will have initially concave profiles. On the body, the curvature is always convex, so the region of concave flow may touch the surface only at the stagnation point. Therefore it would appear that a thin boundary layer would not lie in the region of vortex amplification, and that any destabilization would have to occur before the air reached the boundary layer or by other indirect means.

No evidence from the present test confirms or disproves the importance of this instability.

Reynolds Numbers for High-Speed Entry Into the Earth's Atmosphere

If the Reynolds number of a full-scale missile is kept low, more and perhaps all of the boundary-layer flow may be kept laminar. It is therefore pertinent not only to calculate the magnitude of the Reynolds numbers to be expected in the entry flights of full-scale missiles, but also to see what can be done to keep them to a minimum.

The variation of velocity with altitude of an entering missile is given approximately by

$$V = V_E e^{-\frac{1}{2}\frac{C_D A}{m}\frac{\rho_o}{\beta \sin \theta_E} e^{-\beta y}}$$

for an atmosphere with exponentially varying density (ref. 1). Thus, at any altitude, for a particular selection of V_E, θ_E, and $C_D A/m$, V is known. Furthermore, the density, viscosity, and speed of sound at that altitude may be obtained from the assumed atmosphere or from tables of air properties as a function of altitude. From these data, the Mach number and Reynolds number are readily computed as a function of altitude.

The velocity and angle of entry, V_E and θ_E, are fairly well fixed by the flight range of the re-entering missile. However, $C_D A/m$ is a parameter under some control by the designer. The effect of this parameter on the Reynolds numbers per unit length is shown as a function of Mach number during re-entry in figure 28 for an entrance velocity of 23,000 feet per second and an entrance angle of 30° from the horizontal. For all the cases shown, peak Reynolds number occurs at the time when the Mach number is about 9. Making the missile light in relation to its drag reduces the Reynolds number per unit length. This is accomplished either by reducing the weight, increasing the drag coefficient, or increasing the frontal area. There is this additional reason, then (in addition to those advanced in ref. 1), for using the maximum practical value of $C_D A/m$. This fact was noted by the authors of reference 37.

CONCLUSIONS

From the present tests and analysis of high-drag bodies of revolution at Mach numbers near 4 and 8, Reynolds numbers near 4 million based on diameter, and at stagnation temperatures of 2200° R and 4300° R, respectively, the following conclusions are drawn:

1. The over-all pressure drag of the bodies tested is predicted accurately to within 20 percent in the worst case by modified Newtonian impact theory, slightly better than this by unmodified Newtonian theory, and more accurately still by the component method of NACA RM A55L21 where it is applicable. None of these methods, however, is adequate for predicting the details of the pressure distribution such as is required for interpreting boundary-layer transition data. The component method indicates the existence of a region of pressure rise just behind the spherical portion of the round-nosed cone, consistent with experiment, but does not yield values of the pressure gradient. Impact theory fails to predict the existence of the pressure rise.

2. The static stability of low-fineness-ratio bodies like those tested is inherently very great. Center-of-pressure position of the

60° cone was at about 0.90 of the cone length from the tip, consistent with the theory for low-fineness-ratio cones. Center of pressure of the rounded cone was about 0.91 of the length from the nose, as predicted by impact theory.

3. The measured dynamic stability of the round-nosed cone was found, from application to an example atmospheric entry of a large-scale body, to provide an effective increment to the damping, particularly at low altitudes. It was, in fact, sufficient to overcome the tendency for the pitching oscillation to diverge as a result of the decrease in dynamic pressure at low altitudes.

4. Boundary-layer transition on the round-nosed bodies was found to occur at low Reynolds numbers compared to those that have been obtained on slender bodies. The Reynolds numbers of transition based on local flow properties were about 1 million at both free-stream Mach numbers in spite of the fact that the roughness amplitude was from 0.5 to 2 percent of the calculated boundary-layer thickness. Transition at this value of the local Reynolds number gave about twice the extent of laminar flow at $M_\infty = 8$ as at $M_\infty = 4$.

5. For many of the models, transition was observed to be consistently asymmetric, differing on the different meridians of the model. Since surface roughness was also asymmetric, it is considered that surface roughness influenced transition. Consideration of possible scaling relationships indicated that the test models were representative of relatively smooth full-scale missiles.

6. From the available data on the effects of roughness on boundary-layer transition on pointed bodies, critical values of a roughness parameter were obtained. It was found that as the local Mach number increased above 2 the permissible values of the roughness parameter increased rapidly.

7. Other potentially important causes of instability which may have contributed to early transition of the boundary layers are:

(a) Extensive regions of subsonic flow which are not susceptible to complete stabilization, regardless of wall temperature.

(b) Regions of rising pressure along the direction of surface streamlines on some of the test bodies.

(c) Amplification of the free-stream turbulence by deceleration of the main stream velocity through the bow shock wave.

(d) Instability of the Görtler type in the vicinity of the stagnation point.

(e) Instability of the shear layer produced behind the highly curved bow shock wave.

8. Transition of the shear layer was noted in several pictures. In addition, when transition began in the boundary layer, the shear layer was observed to be quickly enveloped to form a thicker-than-normal turbulent boundary layer.

Ames Aeronautical Laboratory
National Advisory Committee for Aeronautics
Moffett Field, Calif., Sept. 5, 1956

APPENDIX A

EQUATIONS OF PITCHING MOTION FOR A MISSILE IN DECELERATING FREE FLIGHT AT CONSTANT ALTITUDE

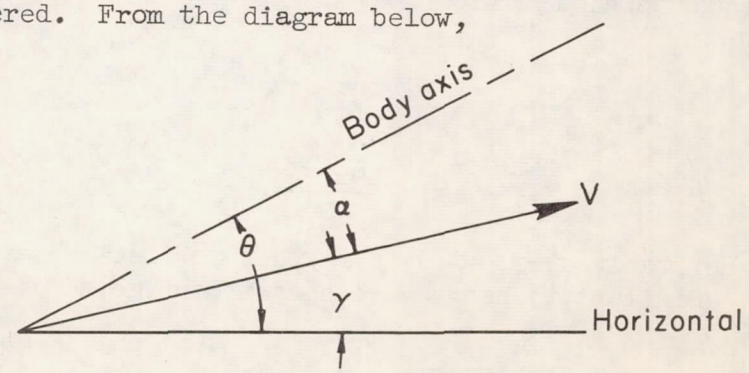
When a missile decelerates, in flight at constant altitude or in a testing range, it experiences a loss in dynamic pressure which tends to amplify the oscillating motion and reduce the pitching frequency. Therefore, the usual equations for flight at constant speed do not accurately describe the motion nor can they, in general, be used to accurately reduce observed motions to aerodynamic coefficients. To derive equations which include the effect of deceleration, we start with the following differential equation of motion of a missile oscillating in pitch at constant altitude with linearly varying aerodynamic coefficients:

$$I_y\ddot{\theta} = C_{m_\alpha} q_\infty A l \alpha + C_{m_q}\left(\frac{l}{V}\right) q_\infty A l \dot{\theta} + C_{m_{\dot{\alpha}}}\left(\frac{l}{V}\right) q_\infty A l \dot{\alpha} \qquad \text{(A1a)}$$

where the notations ($\dot{}$) and ($\ddot{}$) refer to the first and second derivatives with respect to time, respectively, and

$$\left.\begin{aligned} C_{m_\alpha} &= \frac{\partial C_m}{\partial \alpha} \\ C_{m_q} &= \frac{\partial C_m}{\partial\left(\dot{\theta}\frac{l}{V}\right)} \\ C_{m_{\dot{\alpha}}} &= \frac{\partial C_m}{\partial\left(\dot{\alpha}\frac{l}{V}\right)} \end{aligned}\right\} \qquad \text{(A1b)}$$

These derivatives are assumed invariant with Mach number over the flight range considered. From the diagram below,



$$\left.\begin{aligned} \theta &= \alpha + \gamma \\ \dot{\theta} &= \dot{\alpha} + \dot{\gamma} \\ \ddot{\theta} &= \ddot{\alpha} + \ddot{\gamma} \end{aligned}\right\} \qquad \text{(A2)}$$

and therefore

If C_{L_q} and $C_{L_{\dot{\alpha}}}$ are neglected, the equation for rate of change of the flight direction is:

$$mV\dot{\gamma} = C_{L_\alpha} q_\infty A\alpha \qquad \text{(A3a)}$$

or

$$\dot{\gamma} = \frac{C_{L_\alpha} q_\infty A\alpha}{mV} = \frac{C_{L_\alpha} \rho_\infty VA\alpha}{2m} \qquad \text{(A3b)}$$

Change variables from time to distance traveled, x, where the notations (') , (") refer to the first and second derivatives with respect to x, respectively.

$$\dot{\gamma} = V\gamma' \qquad \text{(A4a)}$$

$$\ddot{\gamma} = V^2\gamma'' + \gamma' \frac{dV}{dt} \qquad \text{(A4b)}$$

where

$$\frac{dV}{dt} = -\frac{C_D q_\infty A}{m} = -\frac{C_D \rho_\infty V^2 A}{2m} \qquad \text{(A4c)}$$

so that

$$\ddot{\gamma} = V^2\gamma'' - \frac{C_D \rho_\infty V^2 A\gamma'}{2m} \qquad \text{(A4d)}$$

Substitute equation (A3b) into (A4a)

$$\gamma' = \frac{C_{L_\alpha} \rho_\infty A\alpha}{2m} \qquad \text{(A5a)}$$

and

$$\gamma'' = \frac{C_{L_\alpha} \rho_\infty A\alpha'}{2m} \qquad \text{(A5b)}$$

so that the derivatives of γ with respect to distance are independent of velocity. Similarly, change variables from time to distance in equation (A2).

$$\left.\begin{aligned} \theta &= \alpha + \gamma \\ \dot{\theta} &= V\left(\dot{\alpha} + \frac{C_{L_\alpha}\rho_\infty A\alpha}{2m}\right) \\ \ddot{\theta} &= V^2\left[\ddot{\alpha} - \left(C_D - C_{L_\alpha}\right)\frac{\rho_\infty A}{2m}\dot{\alpha} - C_D C_{L_\alpha}\left(\frac{\rho_\infty A}{2m}\right)^2\alpha\right] \end{aligned}\right\} \quad (A6)$$

Substitute (A6) into (A1) and collect terms.

$$\ddot{\alpha} - \left[\left(C_{m_q} + C_{m_{\dot{\alpha}}}\right)\frac{\rho_\infty A l^2}{2I_y} - \left(C_{L_\alpha} - C_D\right)\frac{\rho_\infty A}{2m}\right]\dot{\alpha} - \left[C_{m_\alpha}\frac{\rho_\infty A l}{2I_y} + \frac{C_{L_\alpha}C_{m_q}}{mI_y}\left(\frac{\rho_\infty A l}{2}\right)^2 + C_D C_{L_\alpha}\left(\frac{\rho_\infty A}{2m}\right)^2\right]\alpha = 0 \quad (A7)$$

Equation (A7) has the form:

$$\ddot{\alpha} + k_1\dot{\alpha} + k_2\alpha = 0 \quad (A8)$$

where k_1 and k_2 are constants defined by:

$$k_1 = -\frac{\rho_\infty A}{2m}\left[C_D - C_{L_\alpha} + \left(C_{m_q} + C_{m_{\dot{\alpha}}}\right)\left(\frac{l}{\sigma}\right)^2\right] \quad (A9)$$

and

$$k_2 = -\left[C_{m_\alpha}\frac{\rho_\infty A l}{2I_y} + \frac{C_{L_\alpha}C_{m_q}}{mI_y}\left(\frac{\rho_\infty A l}{2}\right)^2 + C_D C_{L_\alpha}\left(\frac{\rho_\infty A}{2m}\right)^2\right] \quad (A10)$$

The solution to equation (A7) may be written in the following form:

$$\alpha = e^{-\frac{k_1}{2}x}\left[C_1\cos\left(k_2 - \frac{k_1^2}{4}\right)^{1/2}x + C_2\sin\left(k_2 - \frac{k_1^2}{4}\right)^{1/2}x\right] \quad (A11)$$

where $k_1/2$ is the damping constant, and C_1 and C_2 are determined by the amplitude and phase of the oscillation at $x = 0$. The wave length and frequency of oscillation are given by

$$\frac{2\pi}{\lambda} = \frac{2\pi f}{V} = \left(k_2 - \frac{k_1^2}{4}\right)^{1/2} \tag{A12}$$

Thus, λ is constant if k_1 and k_2 are constant, but frequency of oscillation, f, is directly proportional to velocity.

The effect of deceleration on the damping is given by the term, $C_D\rho_\infty A/2m$ in equation (A9). The influence of deceleration on pitching wave length is shown by equation (A12) to depend on both k_1 and k_2 and thus on the additional terms, $C_D\rho_\infty A/2m$ and $C_D C_{I_\alpha}(\rho_\infty A/2m)^2$.

The equations for computing C_{m_α} and $\left(C_{m_q} + C_{m_{\dot\alpha}}\right)$ from observed pitching motions are obtained by use of equations (A9), (A10), and (A12). They are:

$$C_{m_\alpha} = -\left[\frac{(2\pi f)^2 I_y}{q_\infty A l} + \frac{k_1^2 I_y}{2\rho_\infty A l} + \frac{C_{I_\alpha} C_{m_q} \rho_\infty A l}{2m} + \frac{C_D C_{I_\alpha} \rho_\infty A I_y}{2 l m^2}\right] \tag{A13}$$

$$\left(C_{m_q} + C_{m_{\dot\alpha}}\right) = -\frac{I_y}{l^2}\left[\frac{2k_1}{\rho_\infty A} - \frac{\left(C_{I_\alpha} - C_D\right)}{m}\right] \tag{A14}$$

APPENDIX B

RELATIVE CONTRIBUTIONS OF AERODYNAMIC DAMPING AND DAMPING DUE TO DYNAMIC-PRESSURE VARIATION

The significance of the pitch-damping coefficients measured and the variation of dynamic pressure due to density change on the flight characteristics of a missile as it descends from high altitude were investigated as described below. A full-scale missile (similar to the blunt 60° cone tested) was assumed, with the following geometric and aerodynamic properties:

weight	125 slugs
diameter	4 ft
length	2.78 ft
$\frac{x_{cg}}{l}$	70 percent (from nose)
$C_D, C_{m_\alpha}, C_{L_\alpha}, \left(C_{m_q} + C_{m_{\dot{\alpha}}}\right)$	constant, at values measured in the present investigations, dimensionless
θ_E	entrance angle, 30°
V_E	20,000 ft/sec

With the preceding conditions given, the following expression (ref. 20) may be used to describe the amplitude ratio of the missile in descending, power-off flight in the absence of aerodynamic damping:

$$\frac{\alpha_{max}}{\alpha_i} = \left(\frac{q_{\infty i}}{q_\infty}\right)^{1/4} \tag{B1}$$

The relations of reference 1 were used to describe the density variation in the atmosphere and the velocity history of the missile; namely,

$$V = V_E e^{-\frac{C_D \rho_o A}{2\beta m \sin \theta_E} e^{-\beta y}} \tag{B2}$$

and

$$\rho_o e^{-\beta y} = \rho \quad , \qquad \text{slugs/ft}^3$$

where

$$\rho_o = 0.0034 \quad , \qquad \text{slugs/ft}^3$$

$$\beta = \frac{1}{22{,}000} \quad , \qquad \text{ft}^{-1}$$

Combining equations (B1) and (B2) gives

$$\frac{\alpha_{max}}{\alpha_i} = \frac{e^{-\frac{\beta}{4} y_i} e^{\frac{c}{2}} e^{-\beta y_i}}{e^{-\frac{\beta}{4} y} e^{\frac{c}{2}} e^{-\beta y}} \tag{B3a}$$

where

$$c = -\frac{C_D \rho_o A}{2\beta m \sin \theta_E} \tag{B3b}$$

Applying equation (B3) to the particular case described above leads to the curve labeled "dynamic-pressure effects, aerodynamic damping = 0" in figure 8 and represents the damping due to dynamic-pressure variation.

For the purpose of comparing the rate of decay of pitching due to aerodynamic damping with that due to dynamic-pressure change, it is useful to first consider level flight at constant speed at all altitudes within the range of interest. For flights of this type, the envelope of the pitching oscillations, α_{max}, will be given by:

$$\alpha_{max} = \alpha_i e^{-\frac{k_1}{2} x} \tag{B4}$$

where k_1 must be computed for $C_D = 0$ to avoid the introduction of dynamic-pressure-variation effects. The variable k_1 is a function of density alone since the aerodynamic coefficients have been assumed constant. The rate of change of amplitude with distance at every altitude is then

$$\frac{1}{\alpha_{max}} \frac{d\alpha_{max}}{dx} = -\frac{k_1}{2} \tag{B5}$$

where the transposition of α_{max} to the denominator of the left-hand side gives the fractional change in α_{max} per foot of travel. If it is assumed that the rate of decay of amplitude due to damping is at every altitude the same for descending flight as for level flight, then equation (B5) can be used to estimate the contribution of the aerodynamic damping to the pitching motion. The independent variable x must, however, be replaced by the coordinate along the flight path $y/\sin \theta_E$, where y is zero at the surface of the earth.

$$\frac{\sin \theta_E}{\alpha_{max}} \frac{d\alpha_{max}}{dy} = \frac{k_1}{2} \tag{B6}$$

From the definition of $k_1/2$,

$$\frac{k_1}{2} = -\frac{\rho_o A}{4m}\left[\left(C_{m_q} + C_{m_{\dot{\alpha}}}\right)\left(\frac{l}{\sigma}\right)^2 - C_{L_\alpha}\right]e^{-\beta y}$$

$$\frac{k_1}{2} = -D\rho_o e^{-\beta y} = -D\rho \tag{B7a}$$

where

$$D = \frac{A}{4m}\left[\left(C_{m_q} + C_{m_{\dot{\alpha}}}\right)\left(\frac{l}{\sigma}\right)^2 - C_{L_\alpha}\right] \tag{B7b}$$

Combining equations (B6) and (B7) and integrating

$$\int_{\alpha_i}^{\alpha_{max}} \frac{d\alpha_{max}}{\alpha_{max}} = -\frac{D\rho_o}{\sin \theta_E}\int_{y_i}^{y} e^{-\beta y} dy \tag{B8}$$

gives

$$\frac{\alpha_{max}}{\alpha_i} = e^{\frac{D(\rho - \rho_i)}{\beta \sin \theta_E}} = e^{\frac{k_{1_i} - k_1}{2\beta \sin \theta_E}} \tag{B9}$$

Equation (B9) is plotted in figure 8 for the example missile.

If equations (B3a) and (B9) are multiplied, the effect of both aerodynamic damping and dynamic-pressure-variation damping should be obtained. The resulting equation:

$$\left(\frac{\alpha_{max}}{\alpha_i}\right)_{total} = \frac{e^{-\frac{\beta}{4}y_i} e^{\frac{c}{2}} e^{-\beta y_i} e^{-\frac{D\rho_i}{\beta \sin \theta_E}}}{e^{-\frac{\beta}{4}y} e^{\frac{c}{2}} e^{-\beta y} e^{-\frac{D\rho}{\beta \sin \theta_E}}} \tag{B10}$$

is also plotted in figure 8. Aerodynamic damping begins to affect the amplitude ratio at altitudes near 120,000 feet, and becomes increasingly important at lower altitudes, so much so as to eliminate the diverging effect of dynamic-pressure variation at altitudes below 45,000 feet.

While the present paper was in preparation, Mr. H. J. Allen solved equation (A1) for descending flight through the atmosphere, using the density and velocity variations given by equations (B2), assuming constant aerodynamic coefficients, and neglecting only some second-order terms in the differential equation. The solution is given below, from reference (16),

$$\alpha = \alpha_E e^{k_3 e^{-\beta y}} J_0\left(2\sqrt{k_4 + k_3}\, e^{-\frac{\beta y}{2}}\right) \tag{B11}$$

where

$$k_3 = \frac{\rho_0 A}{4\beta m \sin \theta_E}\left[C_D - C_{L_\alpha} + \left(C_{m_q} + C_{m_{\dot{\alpha}}}\right)\left(\frac{l}{\sigma}\right)^2\right] \tag{B12}$$

and

$$k_4 = \frac{\rho_0 A}{2\beta^2 m \sin^2 \theta_E}\left(-\frac{C_{m_\alpha} l}{\sigma^2} + C_{L_\alpha}\beta \sin \theta_E\right) \tag{B13}$$

For large values of the Bessel function argument in equation (B11), Allen found that the following equation was valid:

$$\alpha = \frac{\alpha_E e^{k_3 e^{-\beta y}} \cos\left(\frac{\pi}{4} - 2\sqrt{k_3 + k_4}\, e^{-\frac{\beta y}{2}}\right)}{\sqrt{\pi\sqrt{k_3 + k_4}}\, e^{-\frac{\beta y}{4}}} \tag{B14}$$

and, where the envelope value may be written:

$$\alpha_{max} = \frac{\alpha_E e^{k_3 e^{-\beta y}}}{\sqrt{\pi \sqrt{k_3 + k_4}}\, e^{-\frac{\beta y}{4}}} \tag{B15}$$

It was found that at the first half-cycle of oscillation, descending from infinite altitude, equation (B15) approximates equation (B11) within 1 percent, for the hypothetical missile chosen. The Bessel function argument for this condition is approximately 3.83. The altitude corresponding to this condition is about 250,000 feet.

In order to compare the results of Allen's solution with those presented herein, α_i was chosen at y_i = 200,000 feet. Equation (B15) may then be written:

$$\frac{\alpha_{max}}{\alpha_i} = \frac{e^{-k_3 e^{-\beta y_i}} e^{-\frac{\beta y_i}{4}}}{e^{-k_3 e^{-\beta y}} e^{-\frac{\beta y}{4}}} \tag{B16}$$

If aerodynamic damping is neglected in Allen's solution $\left(\text{i.e., if } \left(C_{m_q} + C_{m_{\dot{\alpha}}}\right) \text{ and } C_{L_\alpha} \text{ are equal to zero, or } \left(C_{m_q} + C_{m_{\dot{\alpha}}}\right)\left(\frac{l}{\sigma}\right)^2 - C_{L_\alpha} = 0\right)$, equation (B16) reduces to equation (B3), Freidrich and Dore's expression. It can also be shown that if substitutions are made for c and D in in equation (B10), this equation will be identical to Allen's solution in the form given in equation (B16).

APPENDIX C

METHOD OF CALCULATING BOUNDARY-LAYER THICKNESS

The nomenclature used in this appendix is that given by Cohen and Reshotko in NACA TN's 3325 and 3326 (refs. 27 and 28).

Equation (35) of reference 27 is, in transformed dimensionless variables, the general equation for velocity and temperature distribution through the laminar boundary layer as a function of distance from the surface. When equation (35) is converted to the physical plane using dimensional variables, it becomes:

$$\frac{y}{\theta} = \frac{t_o}{t_e}\sqrt{\frac{-\beta}{n}}\int_0^{\eta}\left[(1+S) - \left(\frac{\frac{\gamma-1}{2}M_e^2}{1+\frac{\gamma-1}{2}M_e^2}\right)f'^2\right]d\eta \qquad (C1)$$

where

y normal coordinate

θ momentum thickness

t_o free-stream stagnation temperature

t_e local temperature outside boundary layer

β pressure gradient parameter

n correlation number

S enthalpy function

M_e local Mach number outside boundary layer

f' velocity ratio, $\frac{u}{u_e} = \frac{\text{local velocity in boundary layer}}{\text{local velocity outside boundary layer}}$

η similarity variable

As a particular value of y, the case of $y = \delta$ can be considered. For this purpose, the boundary-layer thickness, δ, is arbitrarily defined to agree with the definition used by Van Driest in his flat-plate calculations (ref. 26); that is, $y = \delta$ where $u = 0.995\ u_e$. Equation (C1) may then be written as:

$$\frac{\delta}{\theta} = \frac{t_o}{t_e}\sqrt{\frac{-\beta}{n}}\int_o^{\eta_e}\left[(1+S) - \left(\frac{\frac{\gamma-1}{2}M_e^2}{1+\frac{\gamma-1}{2}M_e^2}\right)f'^2\right]d\eta \qquad (C2)$$

For a given value of β and S_w, the velocity ratio, f', and enthalpy function, S, are tabulated as a function of the similarity variable, η, in reference 27. (The enthalpy function S_w is defined as: $S_w = (t_w/t_o) - 1$, where t_w is the wall temperature.) The integral of equation (C2) is evaluated graphically by use of the tabulated data, thus leading to values of δ/θ. The procedure for determining the momentum thickness, θ, is clearly explained in reference 28.

Experimental and theoretical pressure and velocity distributions were used to evaluate boundary-layer thickness, δ. For the hemisphere at a Mach number of 3.8, experimental values were used from reference 3. For the hemisphere at a Mach number of 8, simple impact theory was used ($C_p = 2\sin^2\theta_s$). The shock-expansion method was used to obtain pressure and velocity distributions over the pointed ogive at a Mach number of 4.

In order that the calculations for boundary-layer thickness be made with the minimum interpolation from the tables of reference 27, values of S_w used were those that were tabulated closest to the experimental conditions. Therefore, the calculations were made for models with slightly different heat-transfer conditions than were tested experimentally. The values used in the calculations and those that corresponded to experiment are shown in the table below, where the temperature ratios are given in terms of the notation of the present report; that is, T_∞ is free-stream static temperature.

Mach number	Model	T_w/T_∞ (calc)	T_w/T_∞ (exp)	S_w (calc)	S_w (exp)
3.8	hemisphere	0.78	1.0	-0.80	-0.743
4.0	pointed ogive	.84	1.0	-.80	-.762
8.0	hemisphere	2.76	1.8	-.80	-.87

Subsequent experience with the method of references 27 and 28 indicated that the effect on δ of using $S_w = -0.80$ instead of S_w corresponding exactly to experiment would have been small.

REFERENCES

1. Allen, H. Julian, and Eggers, A. J.: A Study of the Motion and Aerodynamic Heating of Missiles Entering the Earth's Atmosphere at High Supersonic Speeds. NACA RM A53D28, 1953.

2. Korobkin, Irving: Laminar Heat Transfer Characteristics of a Hemisphere for the Mach Number Range 1.9 to 4.9. NAVORD Rep. 3841, U. S. Naval Ordnance Lab., Oct. 10, 1954.

3. Stine, Howard A., and Wanlass, Kent: Theoretical and Experimental Investigation of Aerodynamic-Heating and Isothermal Heat-Transfer Parameters on a Hemispherical Nose With Laminar Boundary Layer at Supersonic Mach Numbers. NACA TN 3344, 1954.

4. Goodwin, Glen: Heat-Transfer Characteristics of Blunt Two- and Three-Dimensional Bodies at Supersonic Speeds. NACA RM A55L13a, 1956.

5. Low, George M.: Boundary-Layer Transition at Supersonic Speeds. NACA RM E56E10, 1956.

6. Moeckel, W. R.: Some Effects of Bluntness on Boundary-Layer Transition and Heat Transfer at Supersonic Speeds. NACA TN 3653, 1956.

7. Dorrance, William H., and Romig, Mary F.: The Effect of Blunting the Nose of a Cone on Conical Surface Reynolds Number and Laminar Flow Heat Transfer at Hypersonic Mach Numbers. Rep. ZA-7-015, Consolidated Vultee Aircraft Corp., Mar. 1955.

8. Jedlicka, James R., Wilkins, Max E., and Seiff, Alvin: Experimental Determination of Boundary-Layer Transition on a Body of Revolution at $M = 3.5$. NACA TN 3342, 1954.

9. Oliver, Robert E.: An Experimental Investigation of Flow Over Simple Blunt Bodies at a Nominal Mach Number of 5.8. G.A.L. Memo. 26, Cal. Inst. of Tech., June 1, 1955.

10. Seiff, Alvin, and Sommer, Simon C.: Experimental Investigation of the Drag of 30°, 60°, and 90° Cone Cylinders at Mach Numbers Between 1.5 and 8.2. NACA RM A52A14b, 1952.

11. Charters, A. C.: Some Ballistic Contributions to Aerodynamics. Jour. Aero. Sci., vol. 14, no. 3, Mar. 1947, pp. 155-166.

12. Hodges, A. J.: The Drag Coefficient of Very High Velocity Spheres. Tech. Rep. T-656, New Mexico School of Mines, Research and Development Div., Socorro, New Mexico, Oct. 1949.

13. Seiff, Alvin: A Review of Recent Information on Boundary-Layer Transition at Supersonic Speeds. NACA RM A55L21, 1956.

14. Seiff, Alvin: A Free-Flight Wind Tunnel for Aerodynamic Testing at Hypersonic Speeds. NACA Rep. 1222, 1955.

15. Canning, Thomas N.: Investigation of the Lift, Center of Pressure, and Drag of a Projectile at a Mach Number of 8.6 and a Reynolds Number of 17 Million. NACA RM A54H23a, 1954.

16. Allen, H. Julian: Motion of a Ballistic Missile Angularly Misaligned With the Flight Path Upon Entering the Atmosphere, and Its Effect Upon Aerodynamic Heating, Aerodynamic Loads, and Miss Distance. NACA RM A56F15, 1956.

17. Sommer, Simon C., and Stark, James A.: The Effect of Bluntness on the Drag of Spherical-Tipped Truncated Cones of Fineness Ratio 3 at Mach Numbers 1.2 to 7.4. NACA RM A52B13, 1952.

18. Grimminger, G., Williams, E. P., and Young, G. B. W.: Lift on Inclined Bodies of Revolution in Hypersonic Flow. Jour. Aero. Sci., vol. 17, no. 11, Nov. 1950, pp. 675-690.

19. Mass. Inst. of Tech., Dept. of Elect. Engr., Center of Analysis. Tables of Supersonic Flow Around Cones by the Staff of the Computing Section under the Direction of Zdenek Kopal. Tech. Rep. No. 1. Cambridge, 1947.

20. Freidrich, Hans R., and Dore, Frank J.: The Dynamic Motion of a Missile Descending Through the Atmosphere. Jour. Aero. Sci., vol. 22, no. 9, Sept. 1955, pp. 628-632, 638.

21. Sternberg, Joseph: The Transition From a Turbulent to a Laminar Boundary Layer. BRL Rep. 906, Ballistic Research Lab., Aberdeen Proving Ground, May 1954.

22. Carros, Robert J.: Effect of Mach Number on Boundary-Layer Transition in the Presence of Pressure Rise and Surface Roughness on an Ogive-Cylinder Body With Cold Wall Conditions. NACA RM A56B15, 1956.

23. Lees, Lester, and Lin, Chia-Chiao: Investigation of the Stability of the Laminar Boundary Layer in a Compressible Fluid. NACA TN 1115, 1946.

24. Evvard, J. C., Tucker, M., and Burgess, W. C., Jr.: Statistical Study of Transition-Point Fluctuation in Supersonic Flow. NACA TN 3100, 1954.

25. Probstein, Ronald F., and Lin, C. C.: A Study of the Transition to Turbulence of the Laminar Boundary Layer at Supersonic Speeds. Inst. Aero. Sci. Preprint No. 596, Jan. 1956.

26. Van Driest, E. R.: Investigation of Laminar Boundary Layer in Compressible Fluids Using the Crocco Method. NACA TN 2597, 1952.

27. Cohen, Clarence B., and Reshotko, Eli: Similar Solutions for the Compressible Laminar Boundary Layer With Heat Transfer and Pressure Gradient. NACA TN 3325, 1955.

28. Cohen, Clarence B., and Reshotko, Eli: The Compressible Laminar Boundary Layer With Heat Transfer and Arbitrary Pressure Gradient. NACA TN 3326, 1955.

29. Sternberg, Joseph: A Free-Flight Investigation of the Possibility of High Reynolds Number Supersonic Laminar Boundary Layers. Jour. Aero. Sci., vol. 19, no. 11, Nov. 1952, pp. 721-733.

30. Rumsey, Charles B., and Lee, Dorothy B.: Measurements of Aerodynamic Heat Transfer and Boundary-Layer Transition on a 10° Cone in Free Flight at Supersonic Mach Numbers up to 5.9. NACA RM L56B07, 1956.

31. Czarnecki, K. R., and Sinclair, A. R.: An Extension of the Investigation of the Effects of Heat Transfer on Boundary-Layer Transition on a Parabolic Body of Revolution (NACA RM-10) at a Mach Number of 1.61. NACA TN 3166, 1954.

32. Czarnecki, K. R., Robinson, Ross B., and Hilton, John H.: Investigation of Distributed Surface Roughness on a Body of Revolution at a Mach Number of 1.61. NACA TN 3230, 1954.

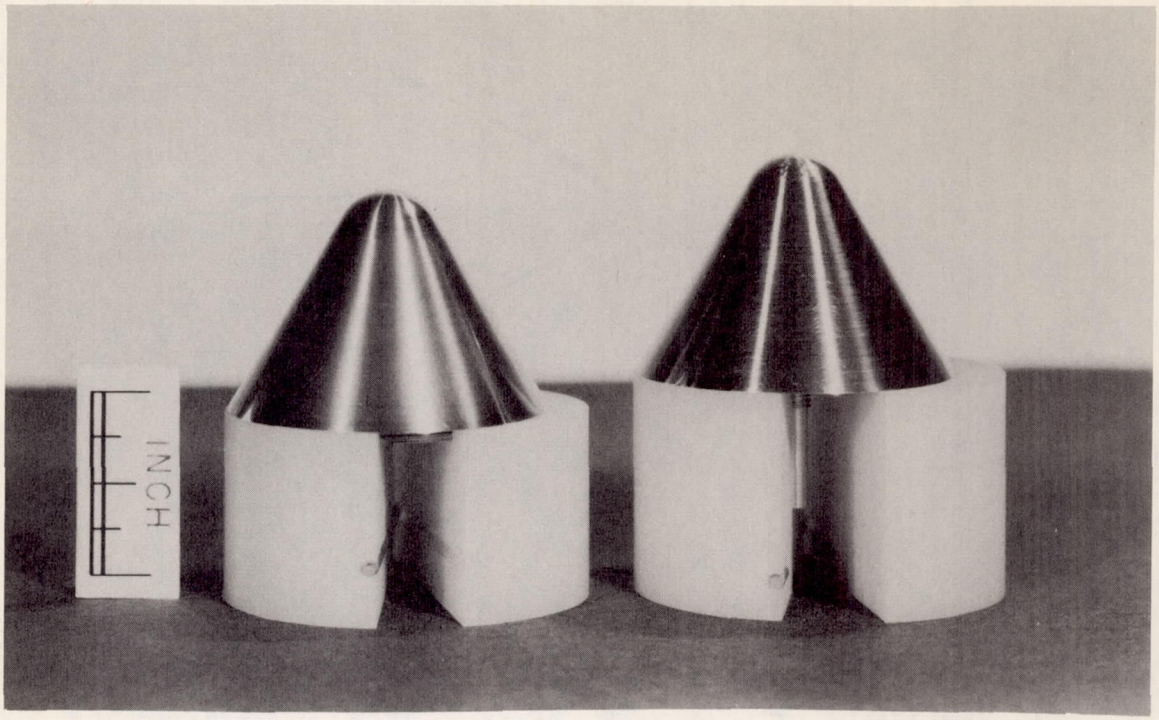
33. Luther, Marvin: Fixing Boundary-Layer Transition on Supersonic-Wind-Tunnel Models. Jet Propulsion Lab. PR 20-256, Cal. Inst. of Tech., Aug. 12, 1955.

34. Low, George M.: Cooling Requirements for Stability of Laminar Boundary Layer With Small Pressure Gradient at Supersonic Speeds. NACA TN 3103, 1954.

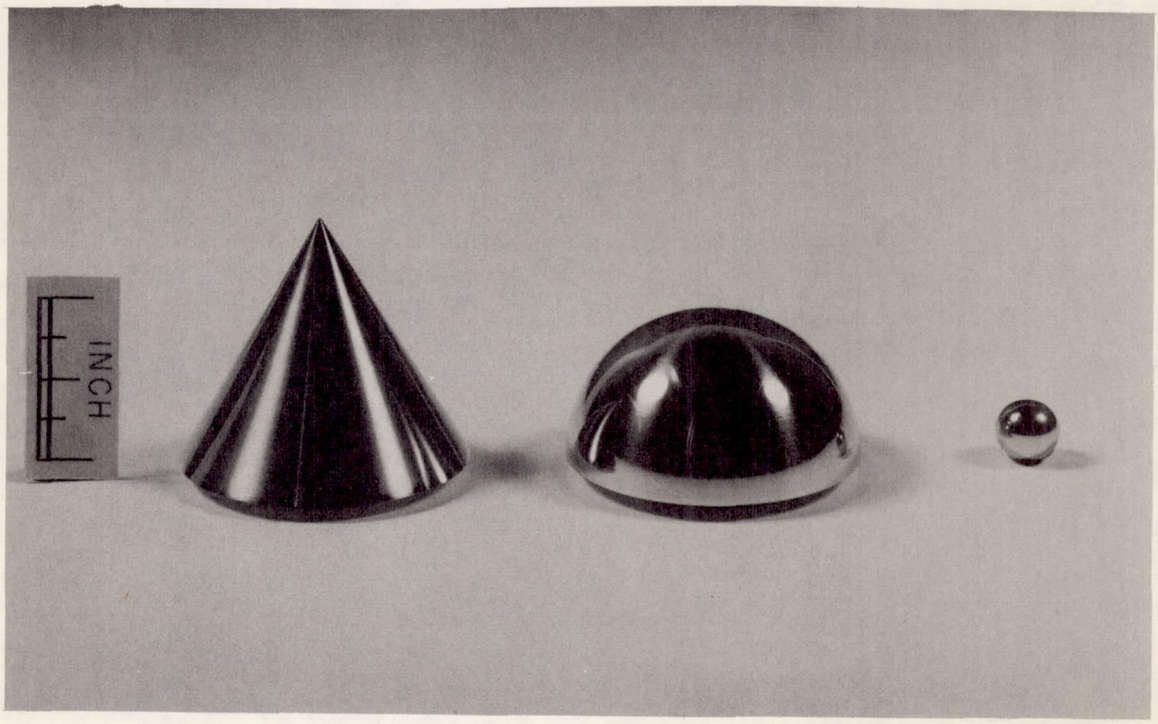
35. Ferri, Antonio, and Libby, Paul A.: Note on an Interaction Between the Boundary Layer and the Inviscid Flow. Jour. Aero. Sci., vol. 21, no. 2, Feb. 1954, p. 130.

36. Görtler, H.: On the Three-Dimensional Instability of Laminar Boundary Layers on Concave Walls. NACA TM 1375, 1954. (Translation of "Uber eine Driedimensionale Instabilitat Laminarer Grenzschickten an Konkaven Wanden." Gesellschaft der Wissenschaften zu Göttingen, Nachrichten, Mathematik, vol. 2, no. 1, 1940.)

37. Allen, H. Julian, and Neice, Stanford E.: Problems of Performance and Heating of Hypersonic Vehicles. NACA RM A55L15, 1956.

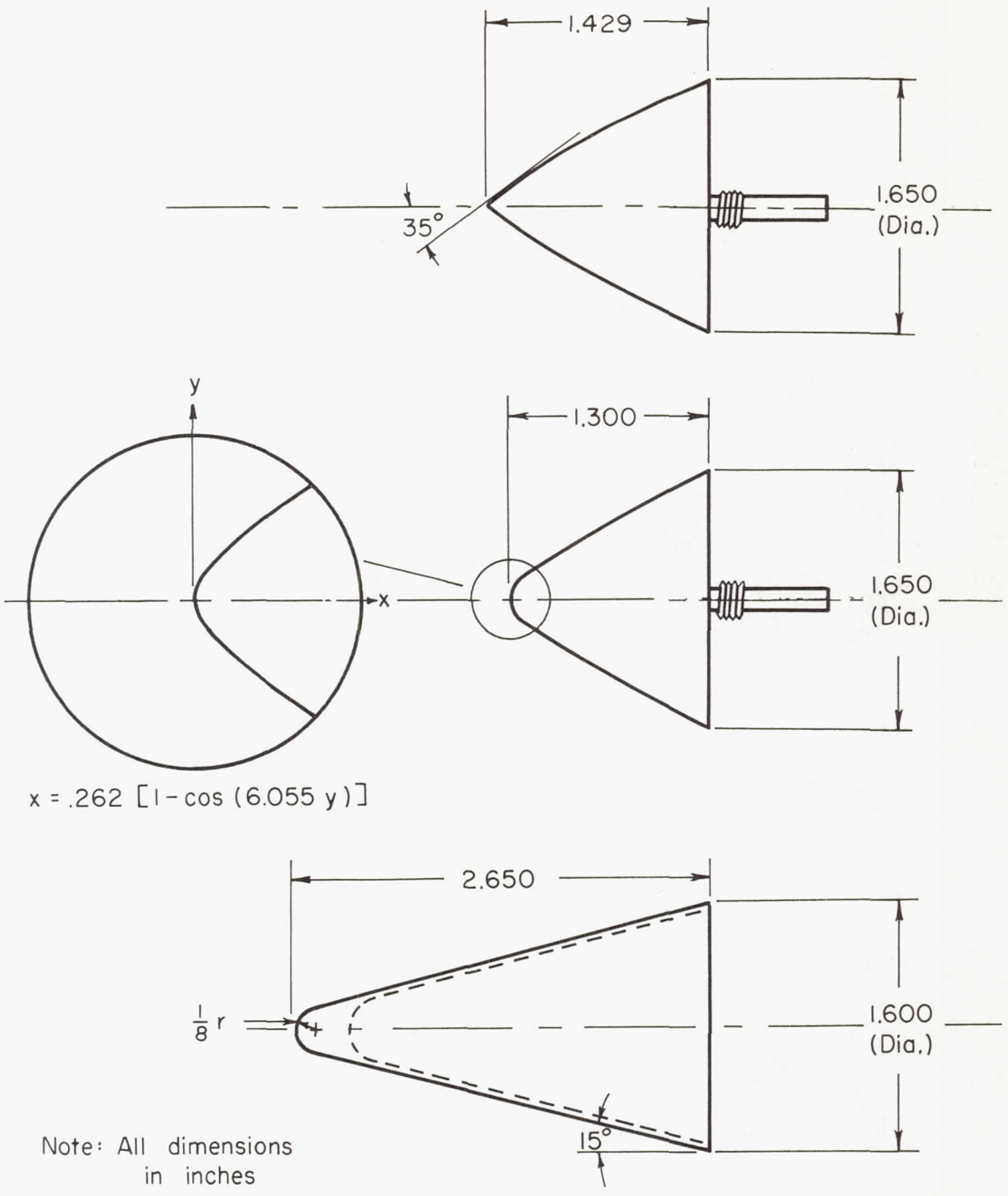


(a) Round-nosed 60° cones. A-20727



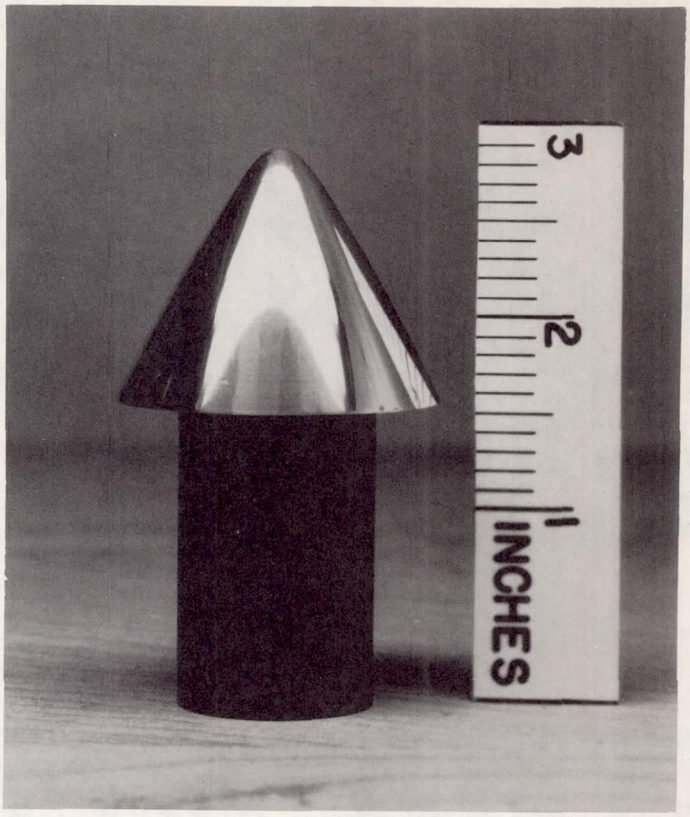
(b) Pointed 60° cone, hemisphere, and sphere. A-20728

Figure 1.- Models.



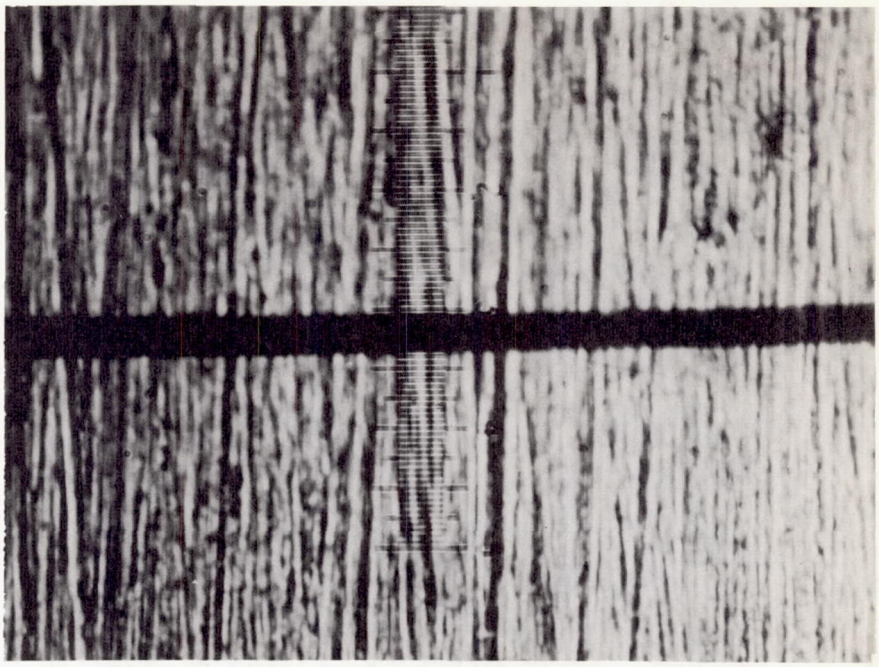
(c) Ogive, sine-wave-rounded ogive, and round-nosed 30° cone.

Figure 1. - Continued.

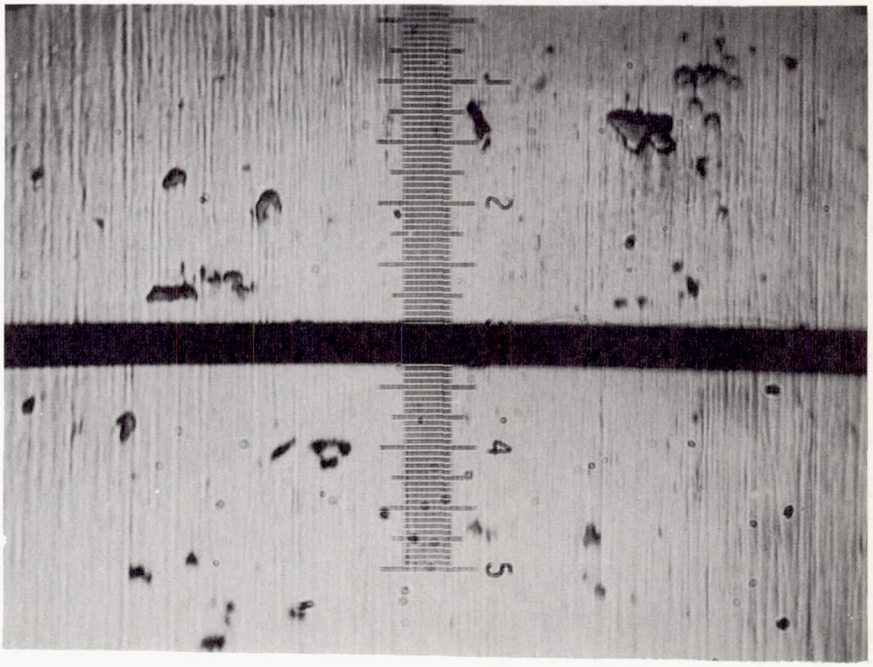


(d) Sine-wave-rounded ogive with Type III finish.

Figure 1.- Concluded.

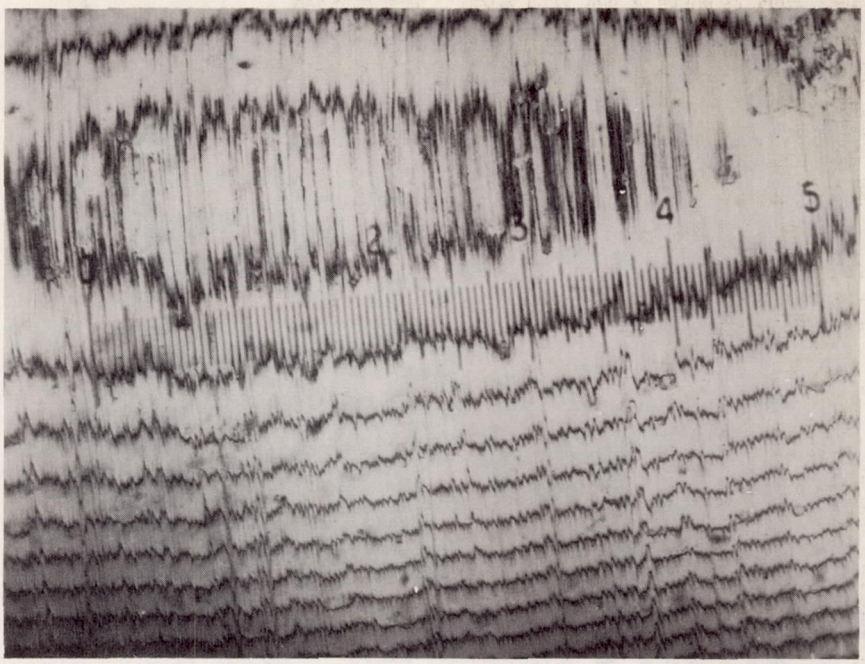


(a) Photomicrograph, Type I finish, 500X.

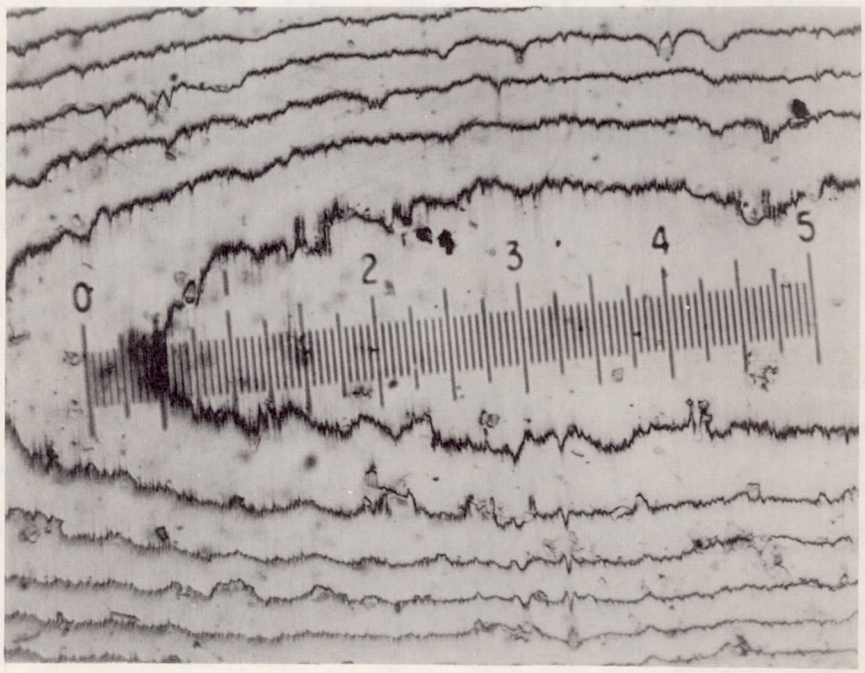


(b) Photomicrograph, Type III finish, 500X.

Figure 2.- Photographs of model surfaces.



(c) Interferogram, Type I surface, 200X.



(d) Interferogram, Type III surface, 200X.

Figure 2.- Continued.



(e) Interferogram of stagnation point, Type III surface, 200X.

Figure 2.- Concluded.

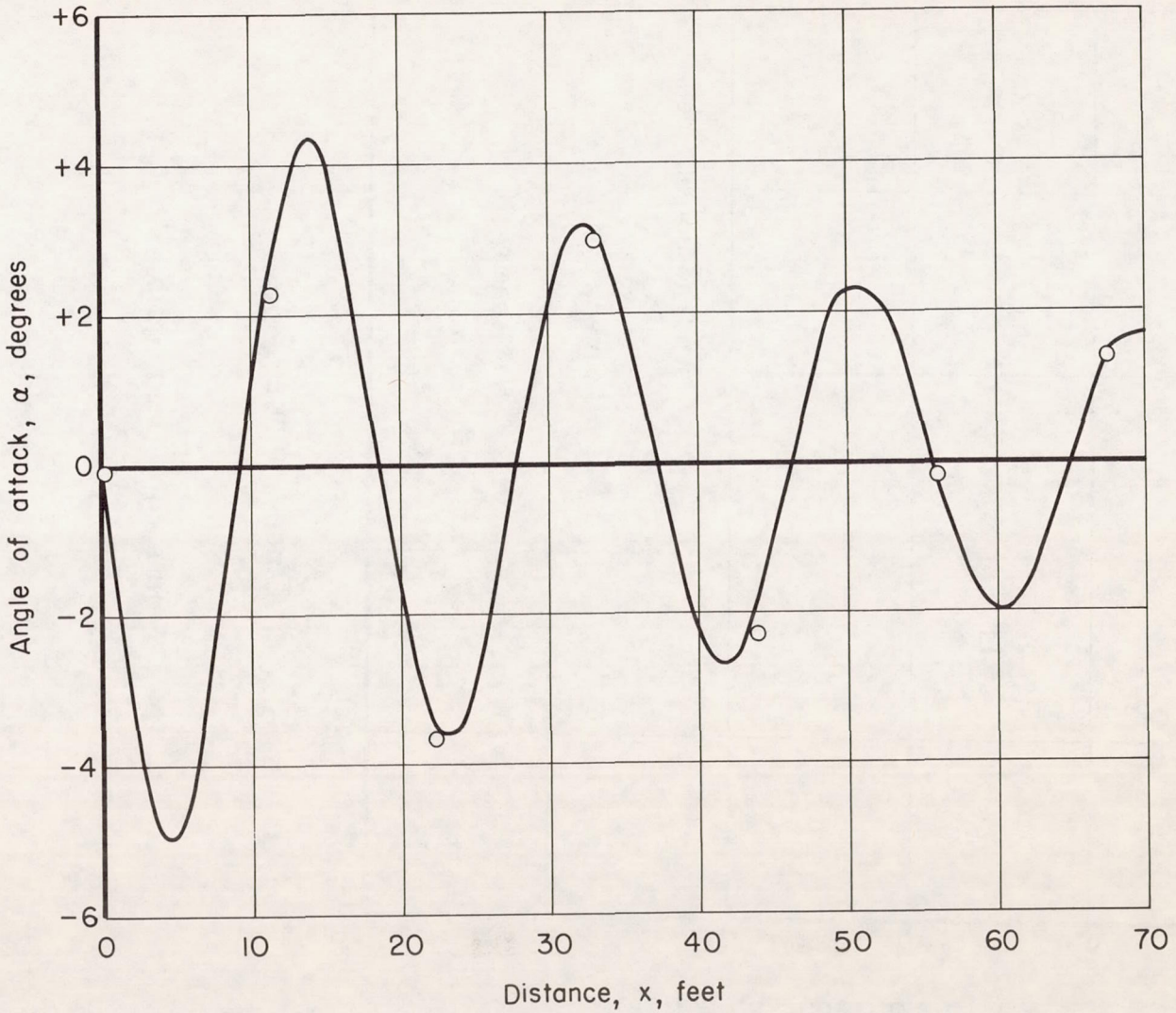


Figure 3.- Typical data for pitching oscillation of a round-nosed 60° cone.

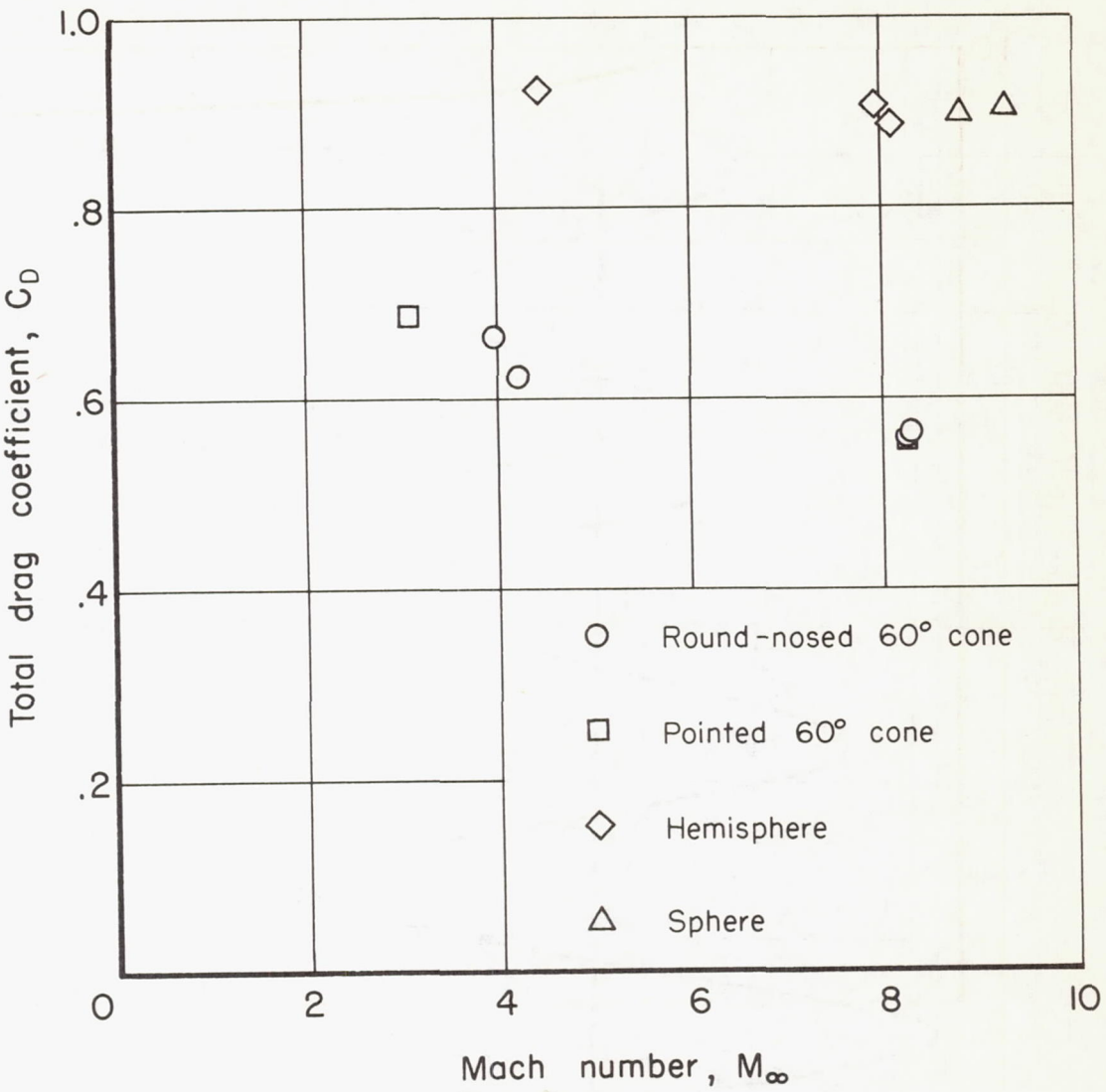
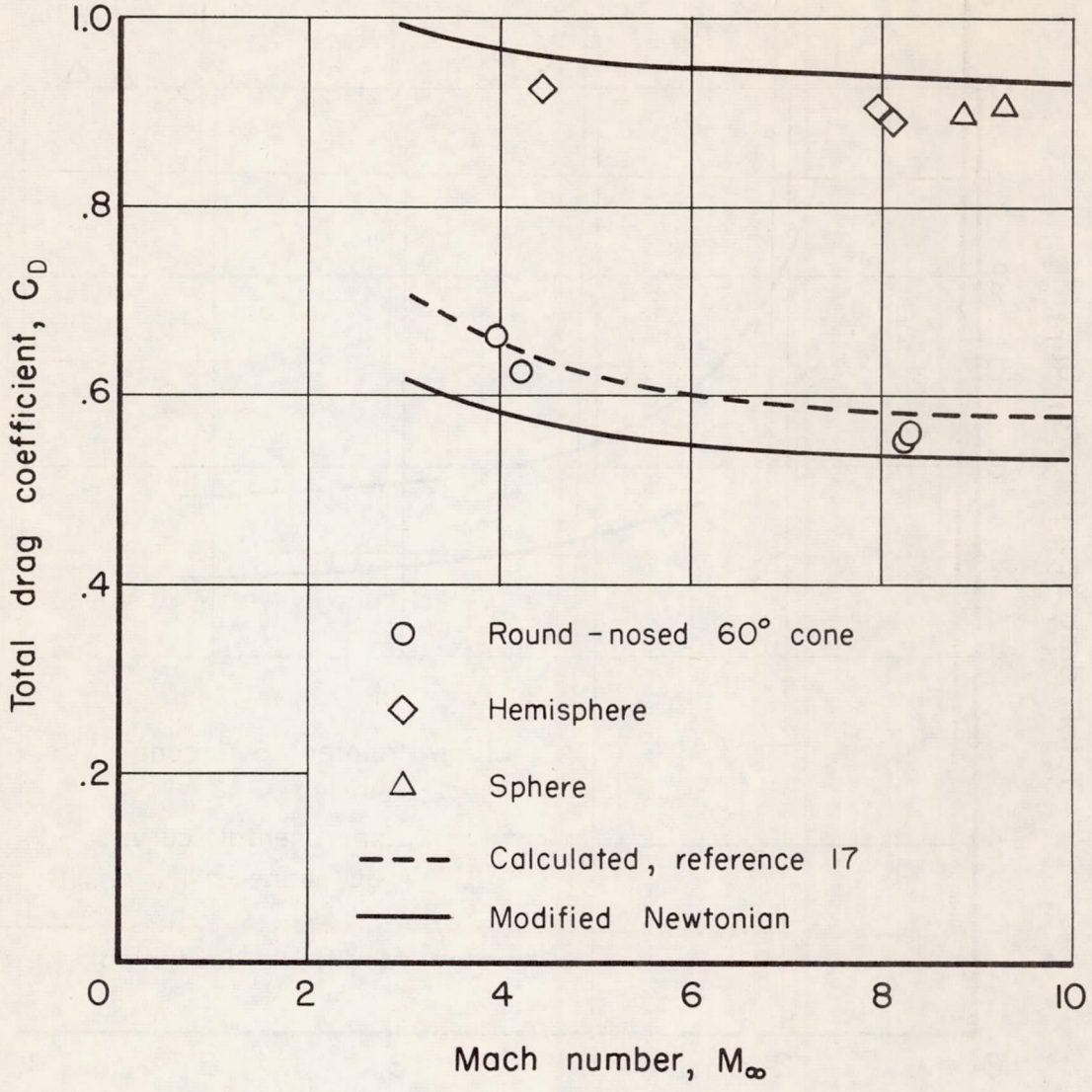
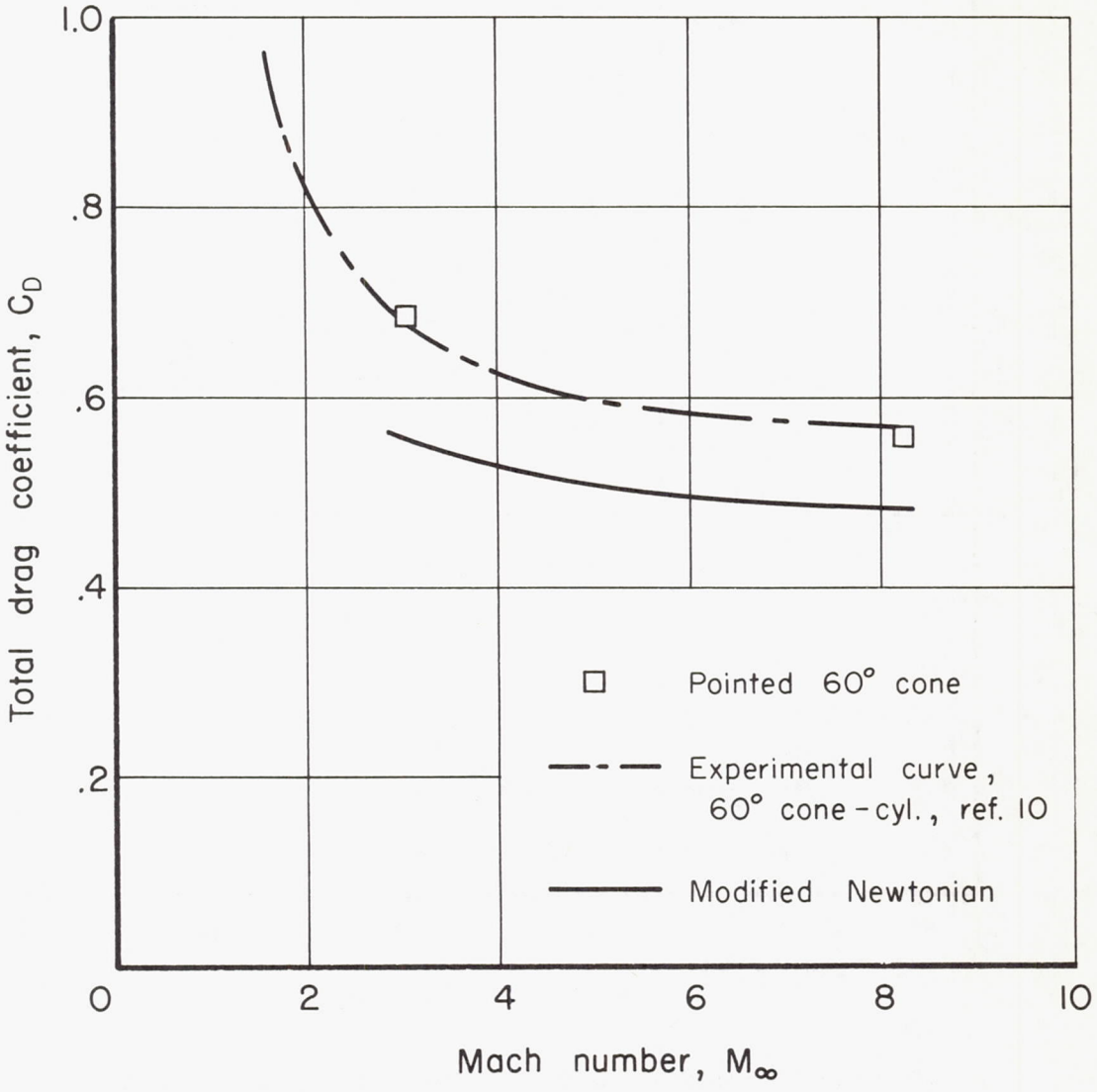


Figure 4.- Drag data.



(a) Round - nosed cone, hemisphere, and sphere.

Figure 5. - Comparison of computed and experimental total drag coefficients.



(b) Pointed 60° cone and 60° cone - cylinder.

Figure 5. - Concluded.

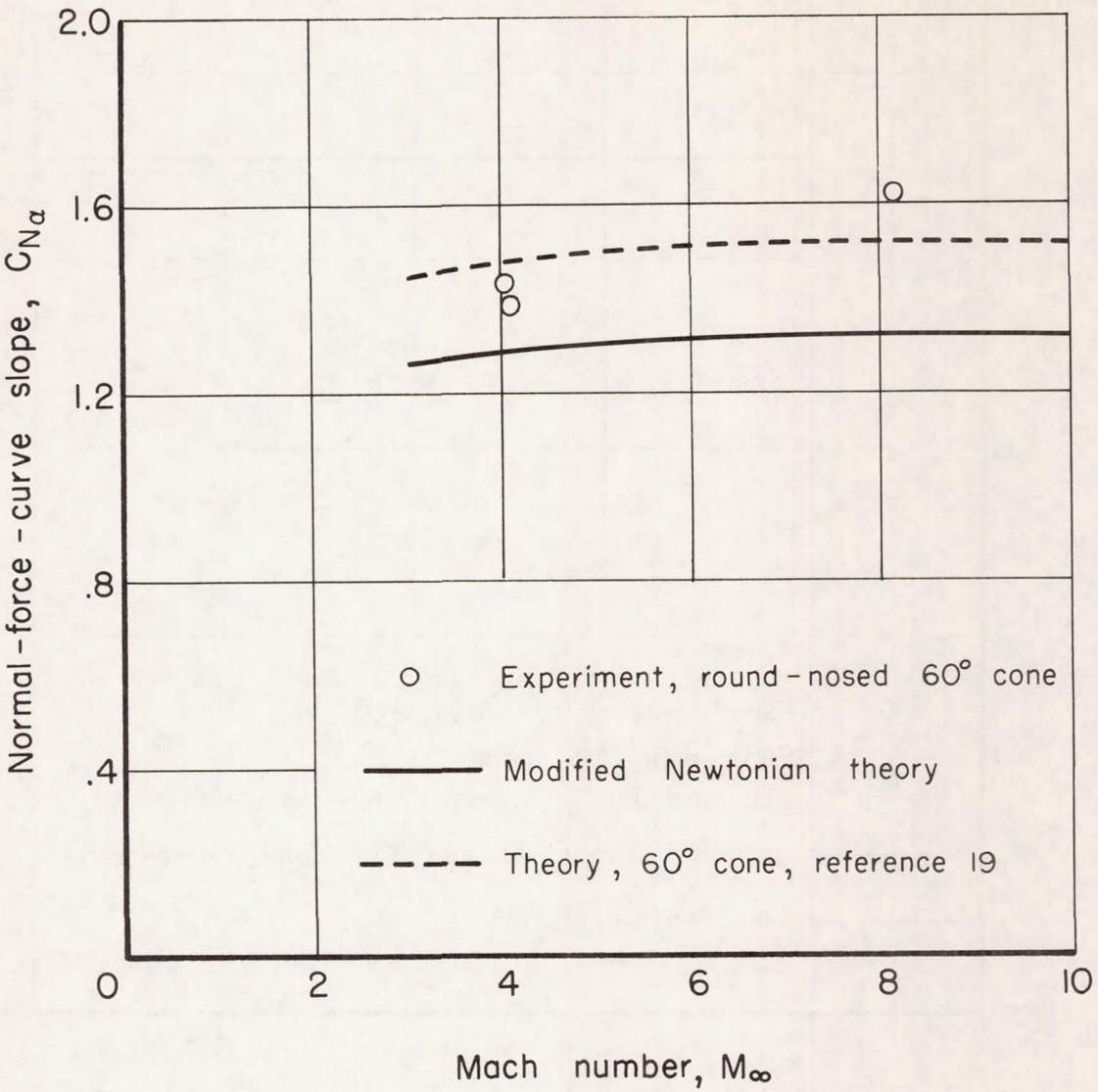


Figure 6. – Normal-force data.

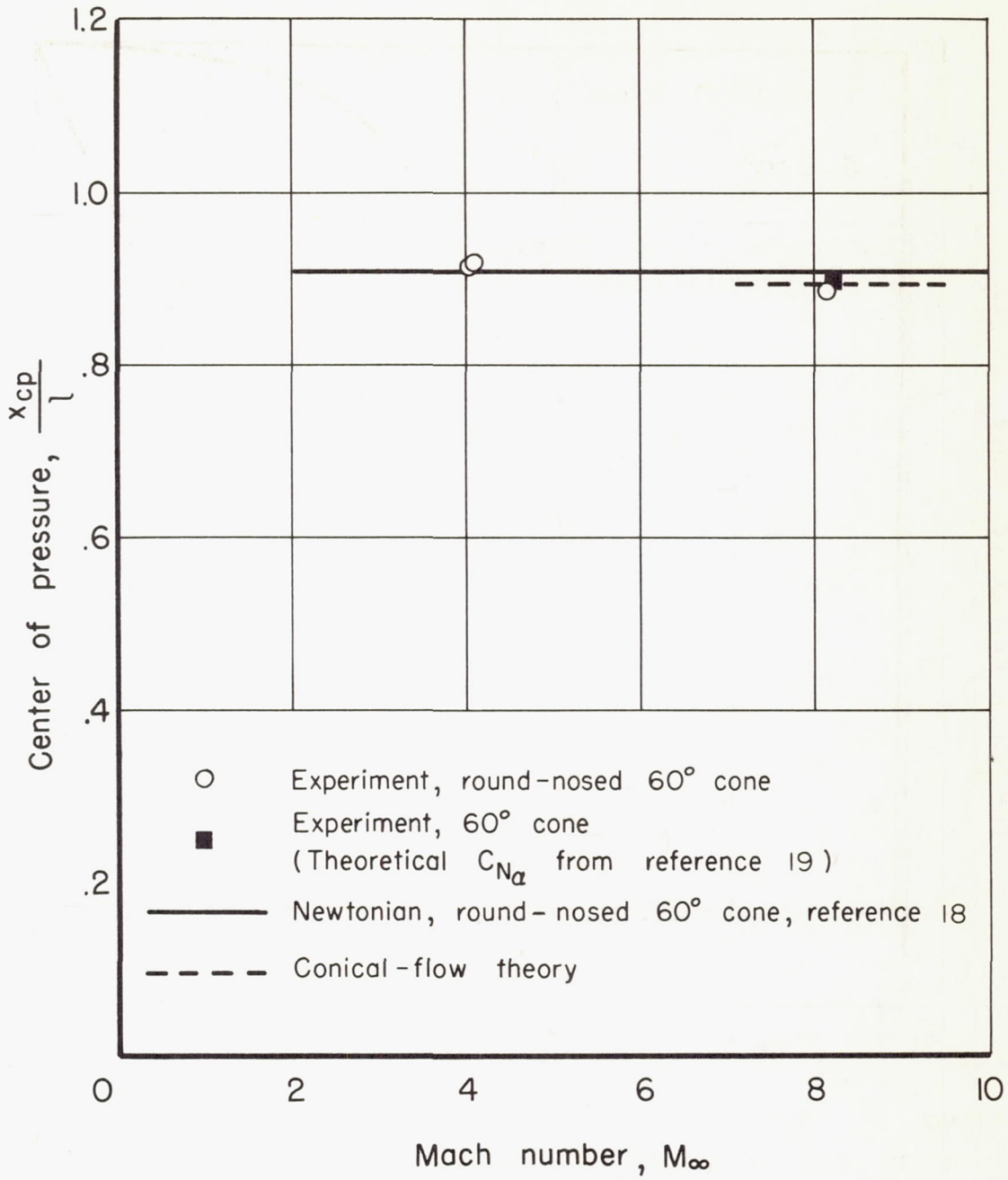


Figure 7.- Center-of-pressure data.

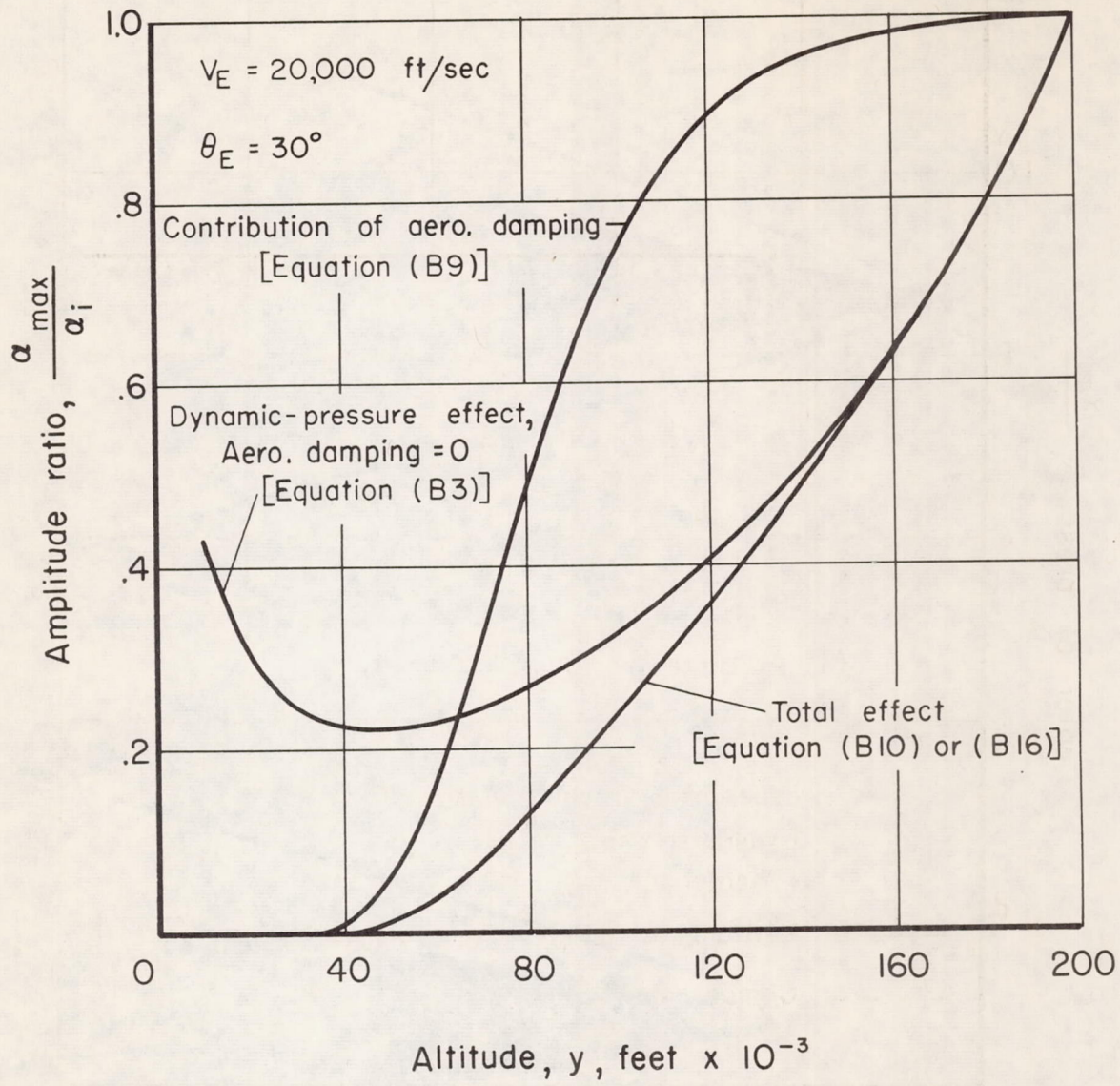
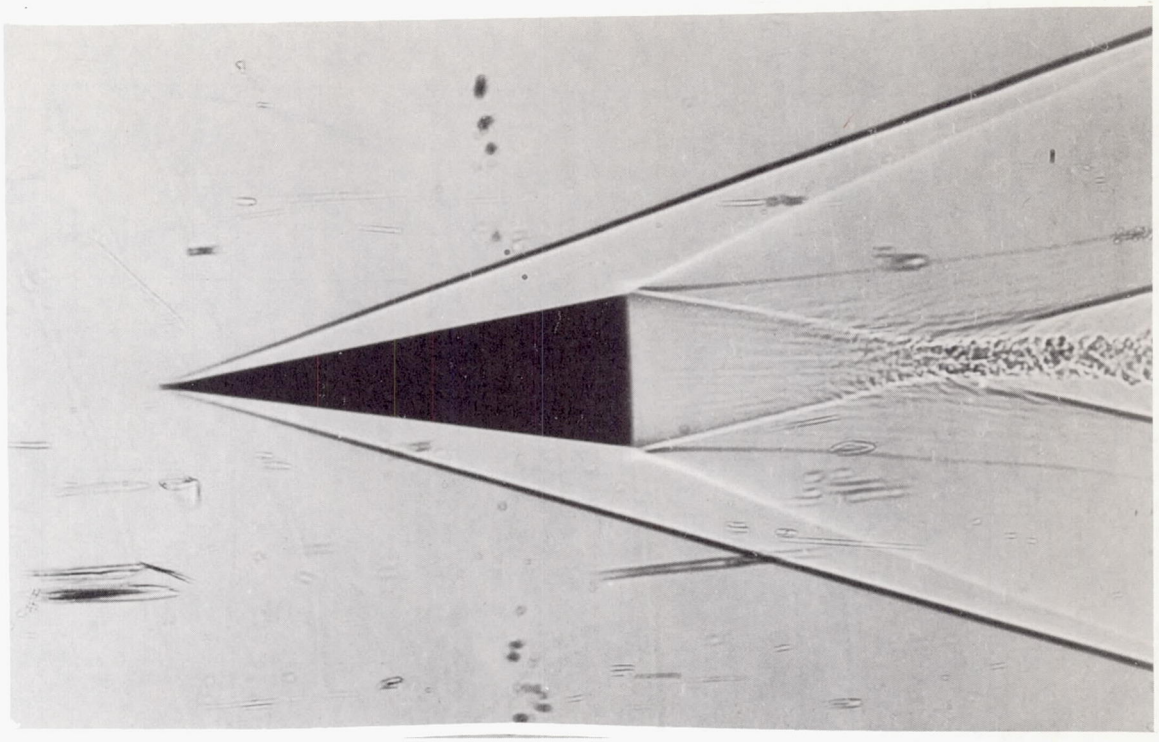
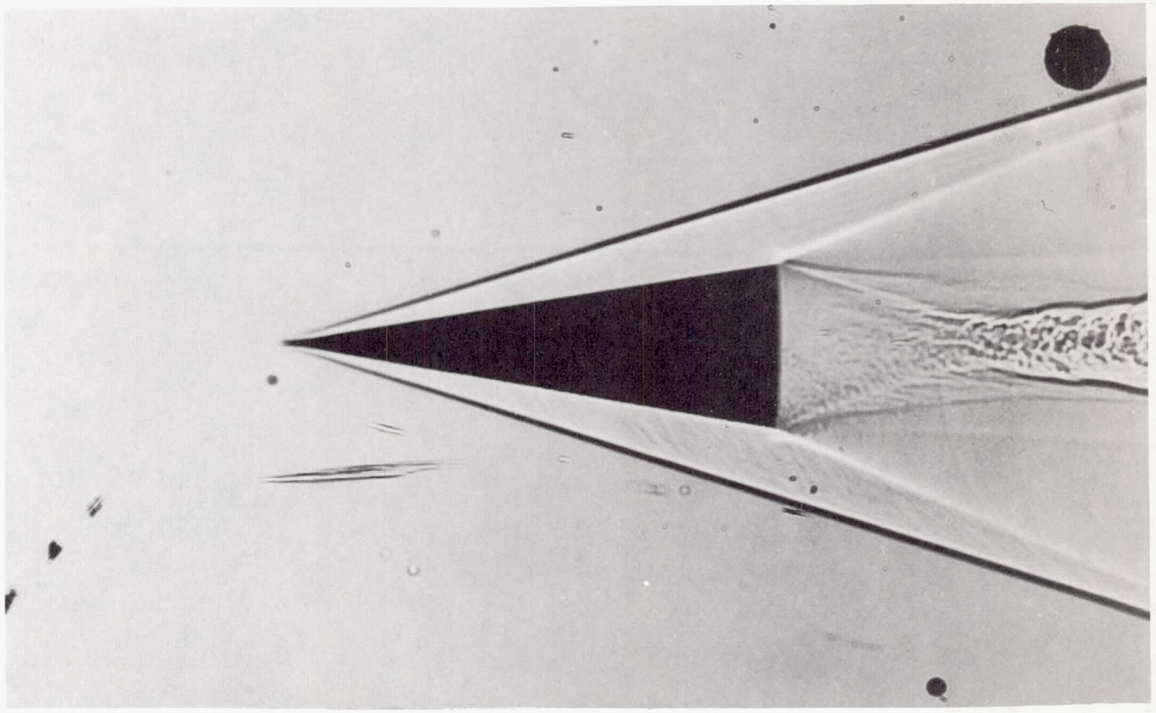


Figure 8. – Relative contributions of dynamic – pressure variation and aerodynamic damping during atmospheric entry of an example missile.

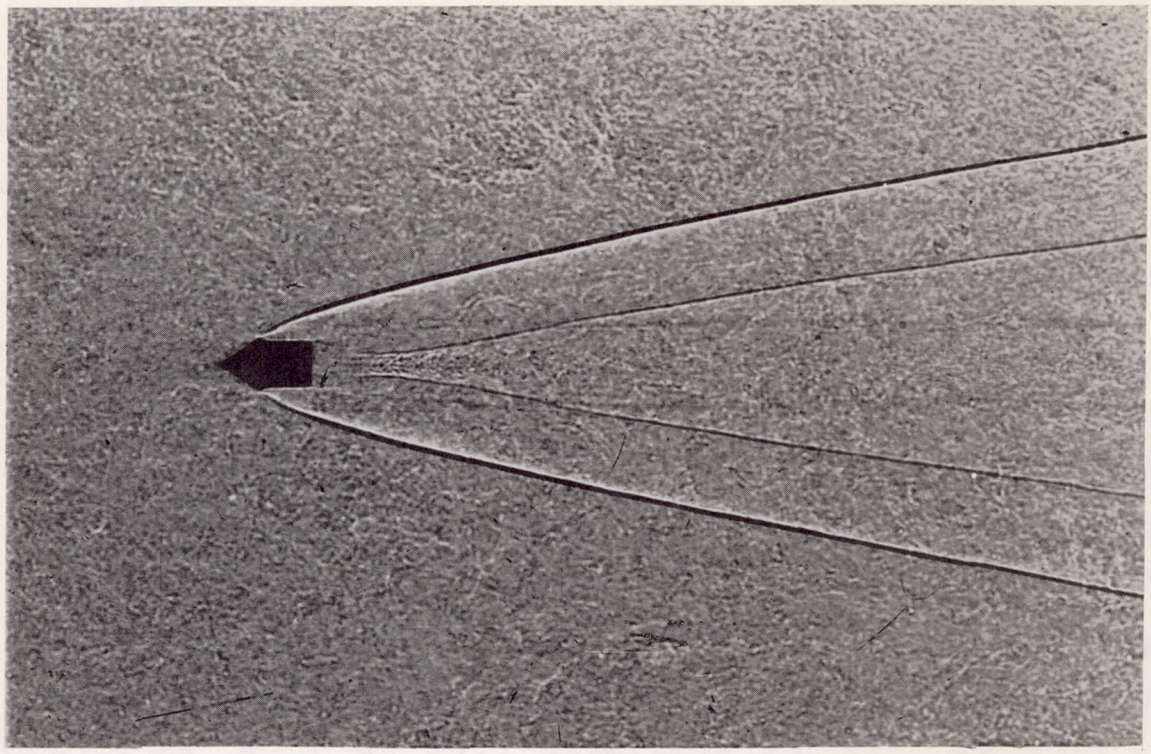


(a) Fully laminar flow off base, $M_\infty = 4$.

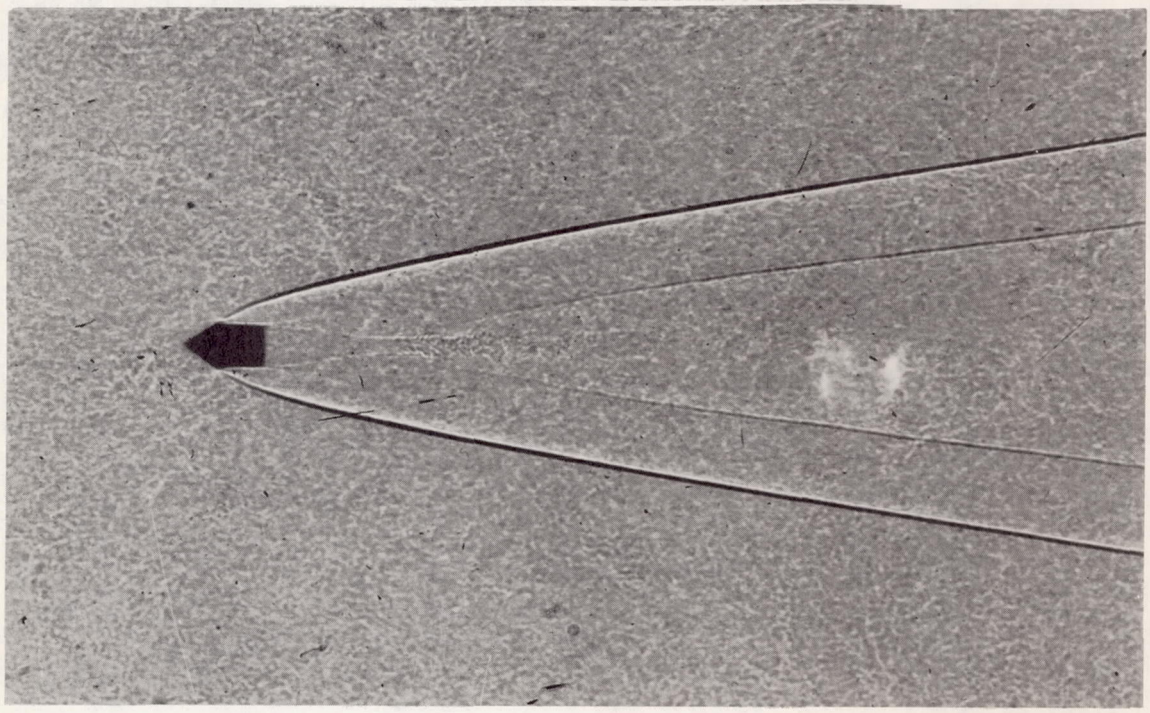


(b) One side turbulent, $M_\infty = 4$.

Figure 9.- Shadowgraphs showing difference in flow field behind base with laminar and turbulent boundary layers.

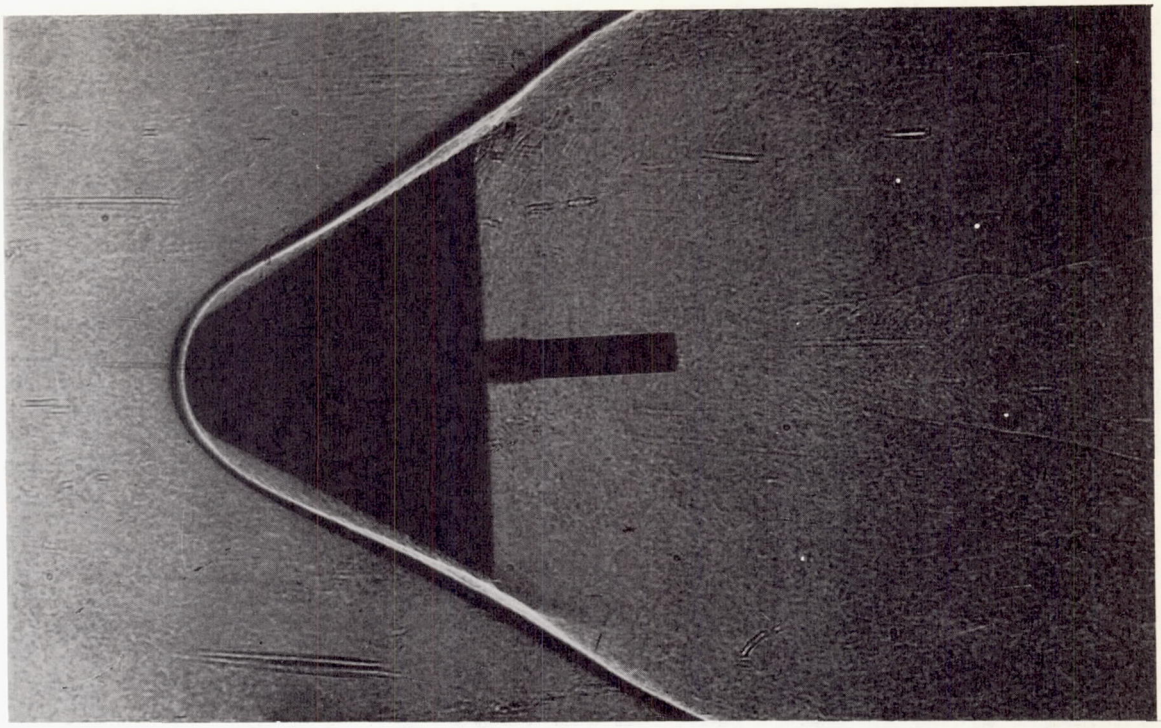


(c) Rough 60° cone-cylinder, $M_\infty = 7.0$.

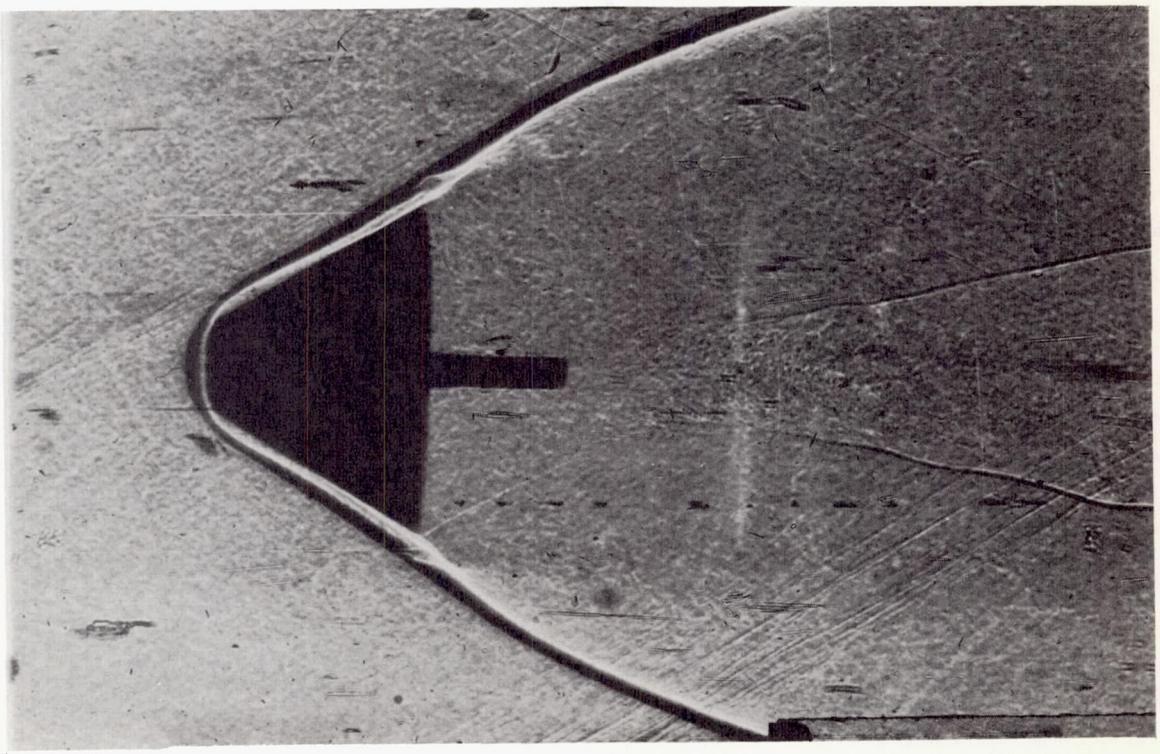


(d) Smooth 60° cone-cylinder, $M_\infty = 8.1$.

Figure 9.- Concluded.

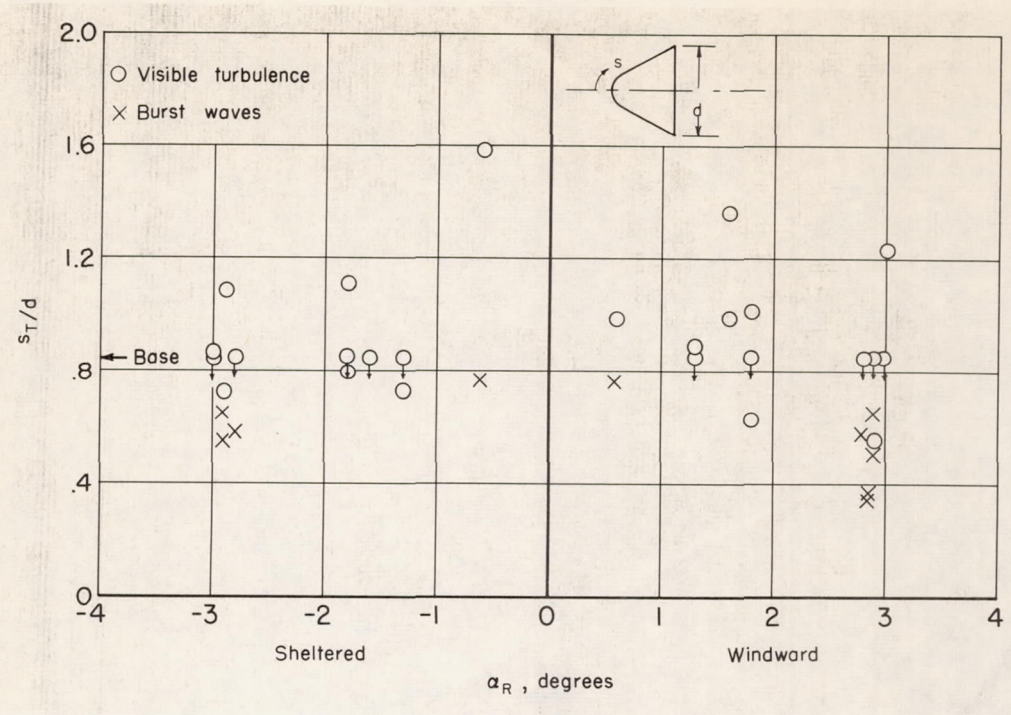


(a) Side-view, low sensitivity.

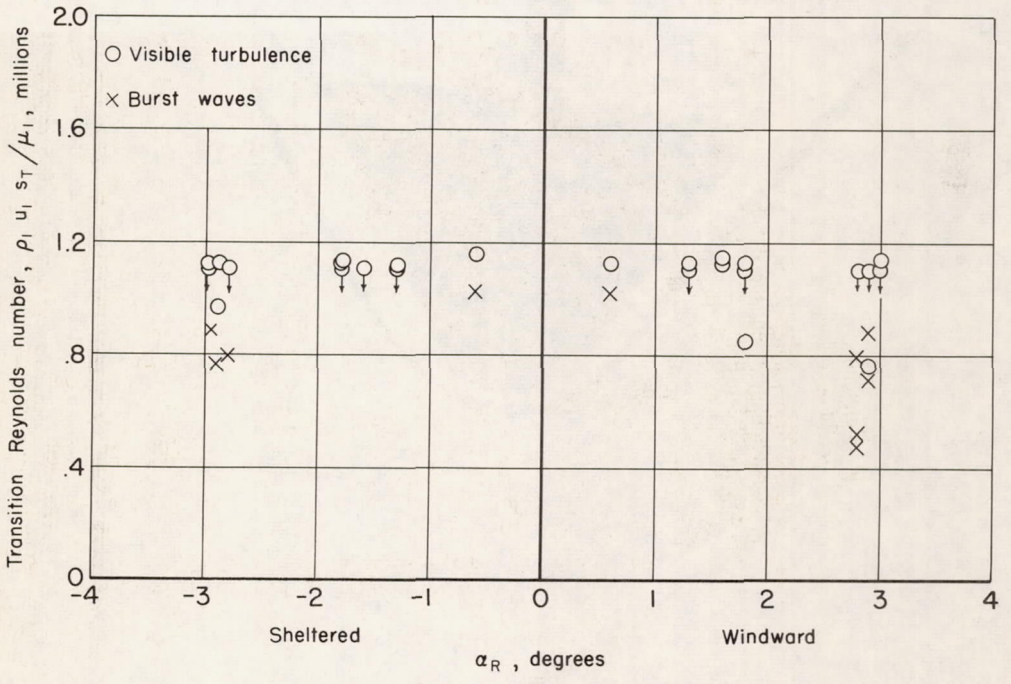


(b) Top-view, high sensitivity.

Figure 10.- Round-nosed 60° cone, $M_\infty = 8.3$.



(a) Dimensionless length of laminar run.



(b) Local Reynolds numbers at transition.

Figure 11.- Transition data from the round-nosed 60° cones with type I surface finish at $M_\infty = 8.3$ and $R_\infty = 4.8 \times 10^6$.

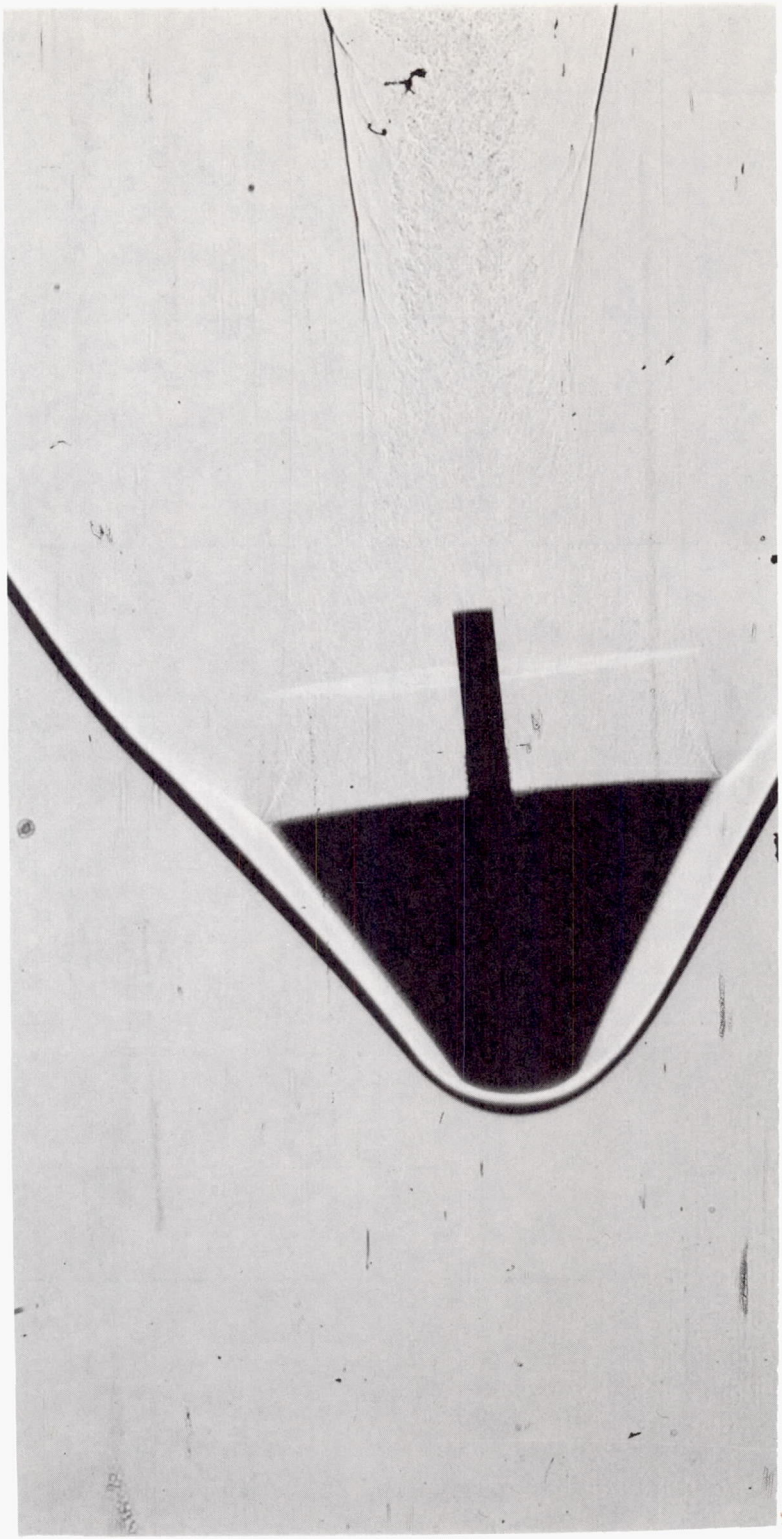
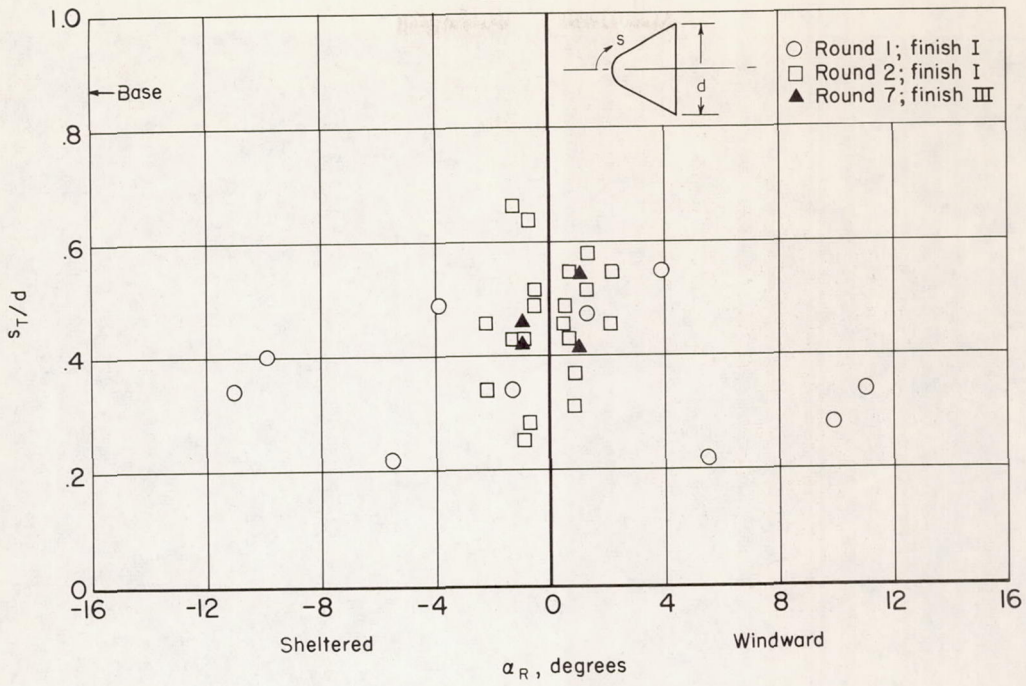
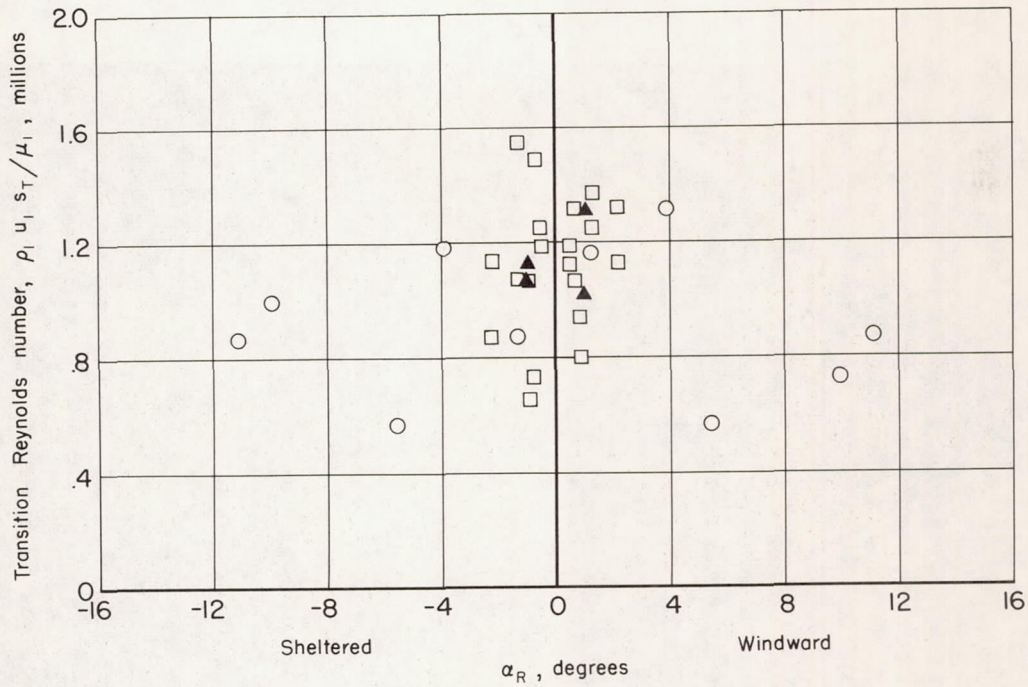


Figure 12.- Round-nosed 60° cone, $M_\infty = 4$.

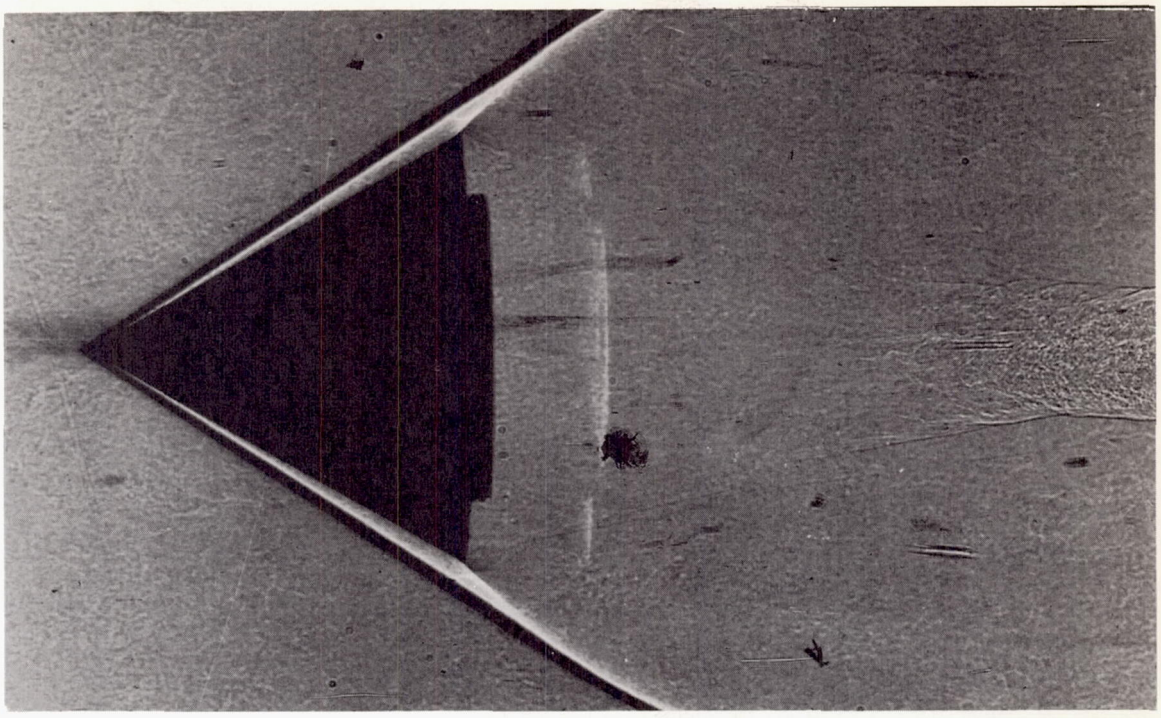


(a) Dimensionless length of laminar run.

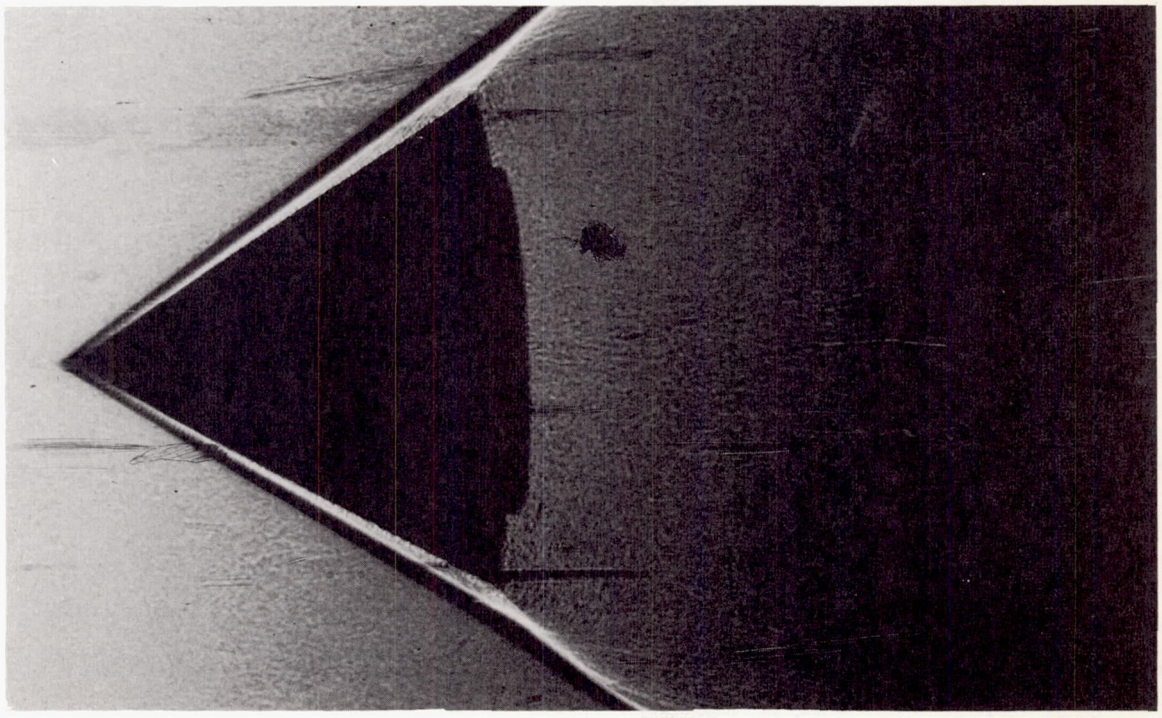


(b) Local Reynolds numbers at transition.

Figure 13.- Transition data, round-nosed 60° cones at $M_\infty = 4.0$ and $R_\infty = 3.8 \times 10^6$.

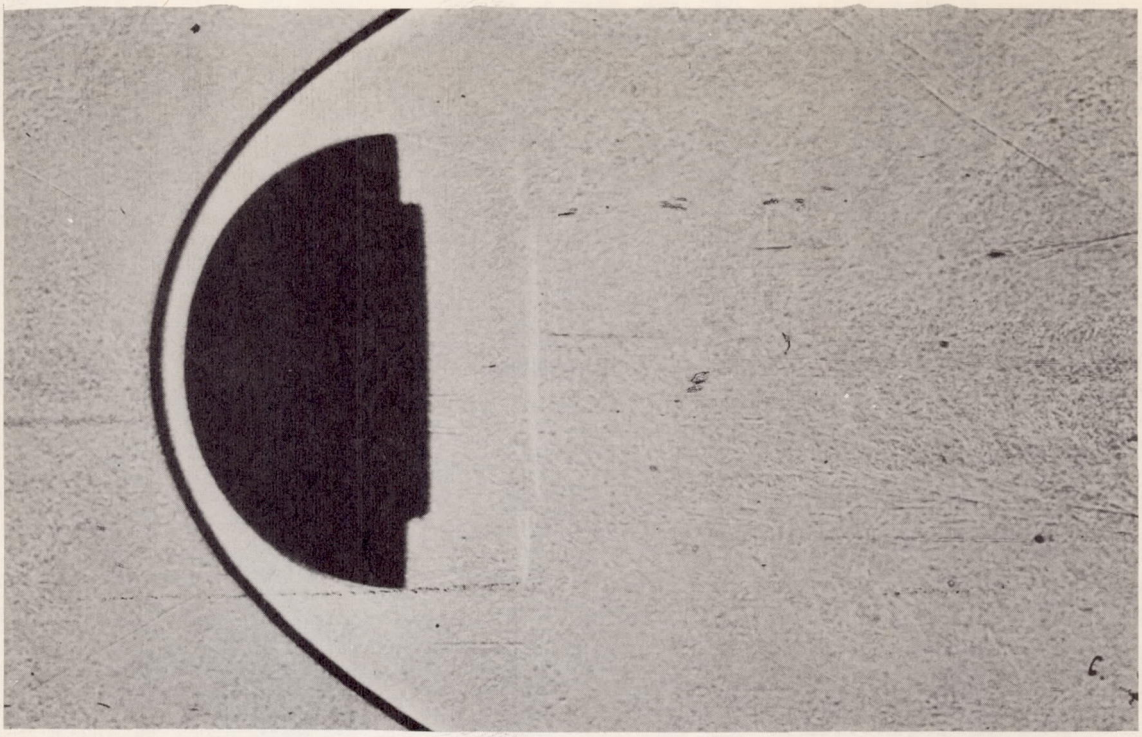


(a) Smooth.

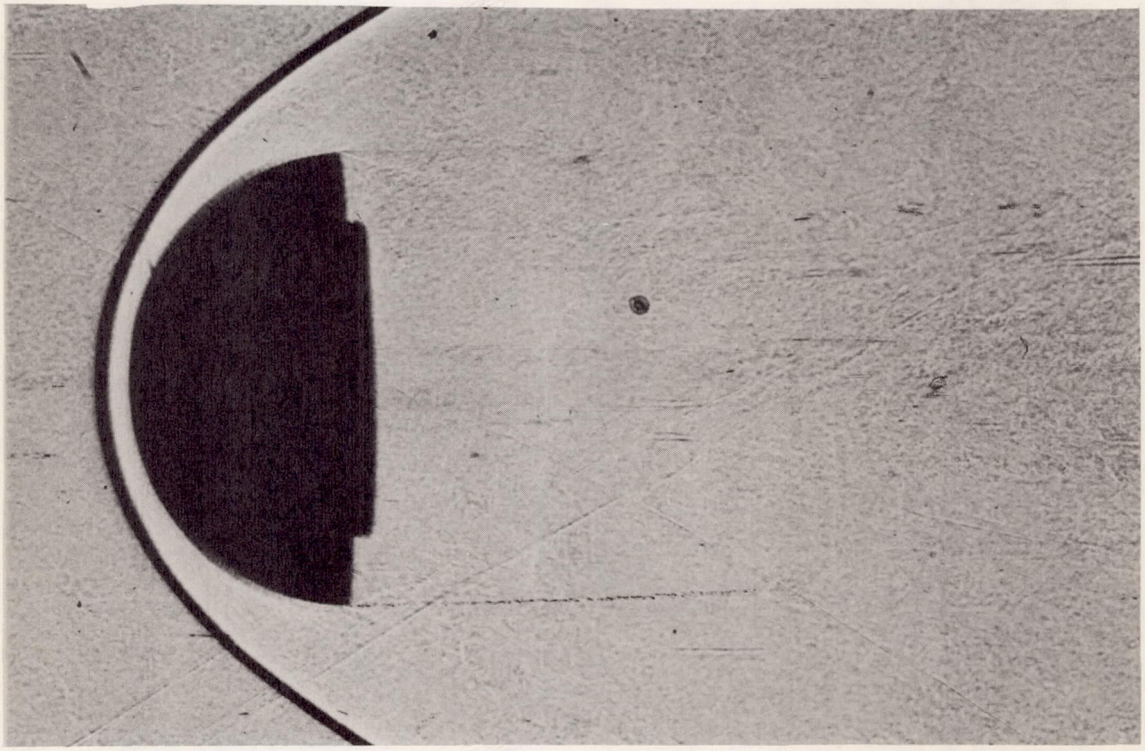


(b) Roughened.

Figure 14.- Pointed 60° cone, $M_\infty = 8.3$.

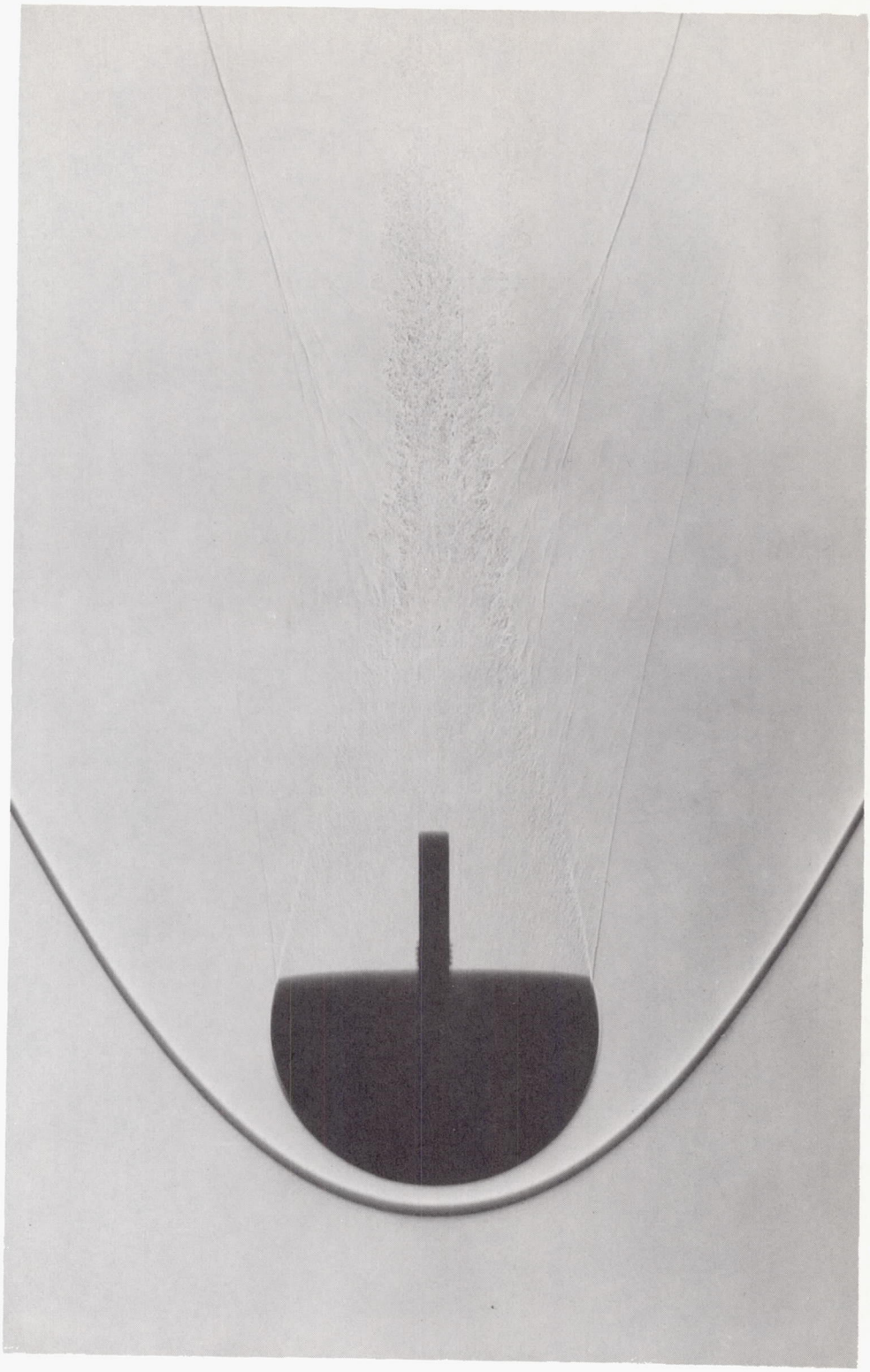


(a) Smooth, $M_\infty = 8.2$.



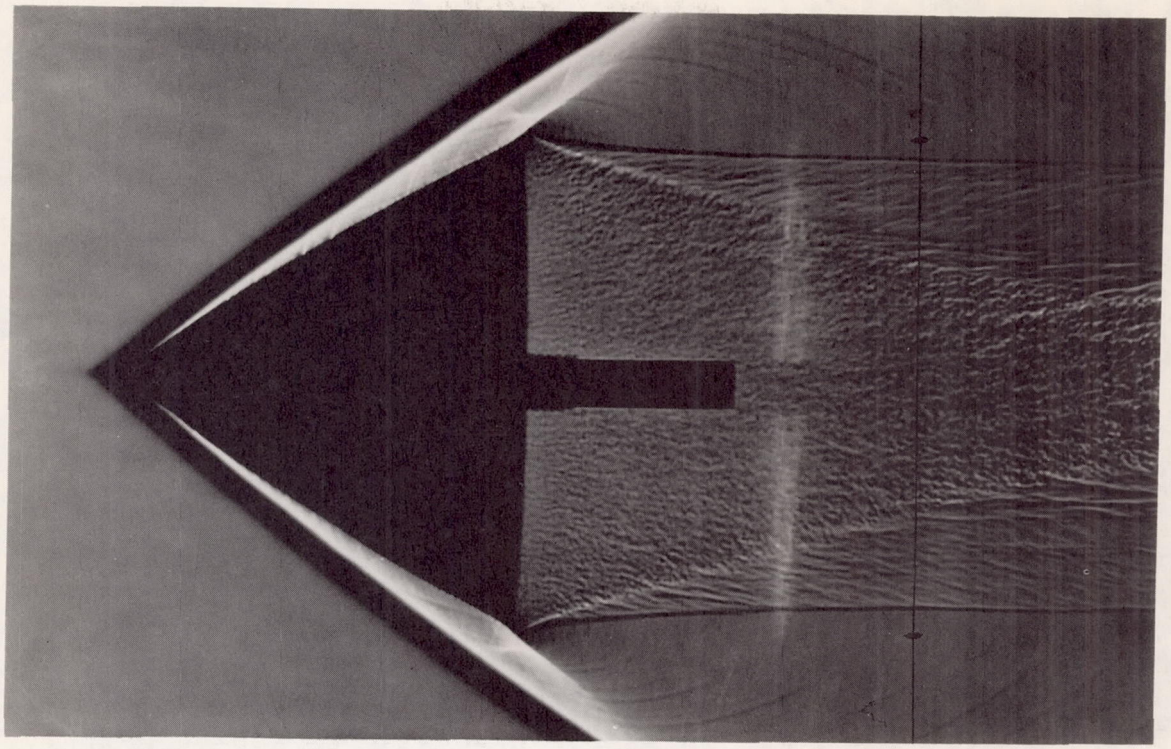
(b) Roughened, $M_\infty = 8.2$.

Figure 15.- Hemispheres.

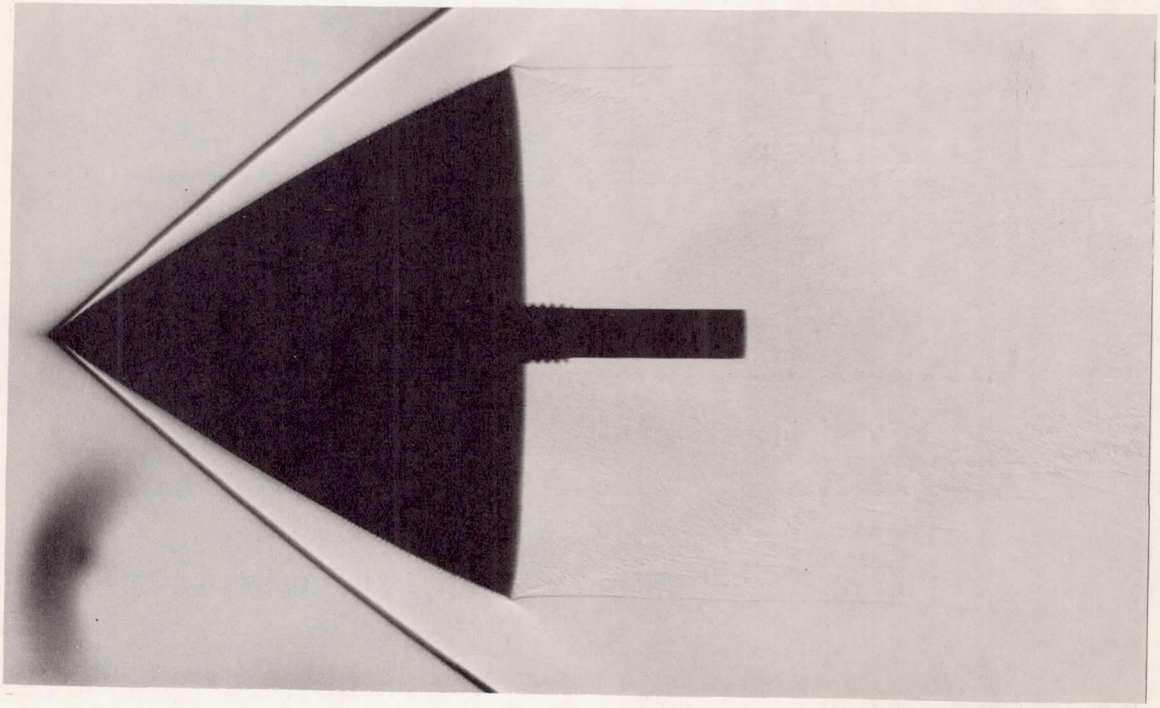


(c) Smooth, $M_\infty = 4$.

Figure 15.- Concluded.



(a) Normal shadowgraph.



(b) Less-sensitive shadowgraph.

Figure 16.- Ogive, $M_\infty = 4$.

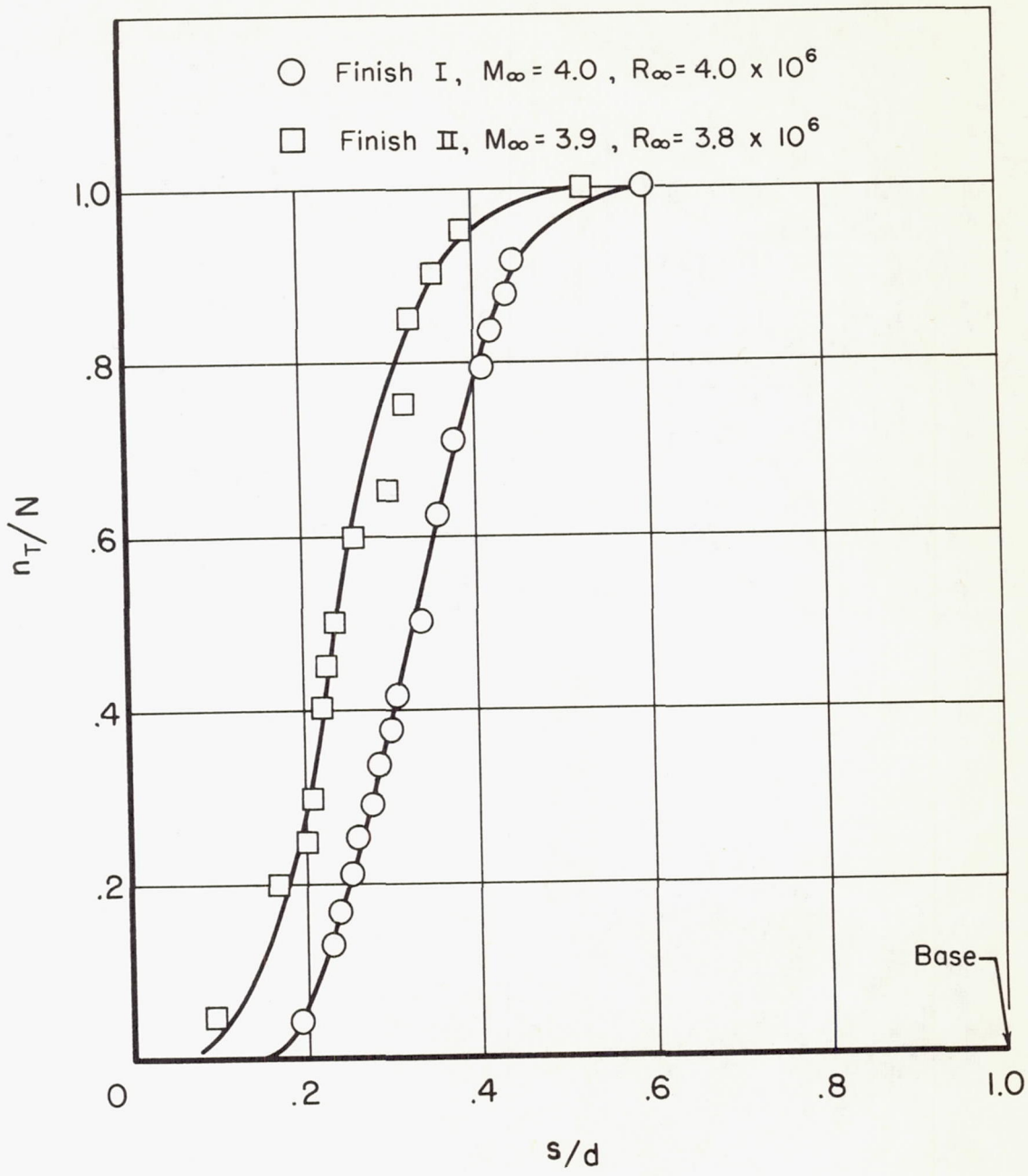


Figure 17. – Transition data from pointed ogives.

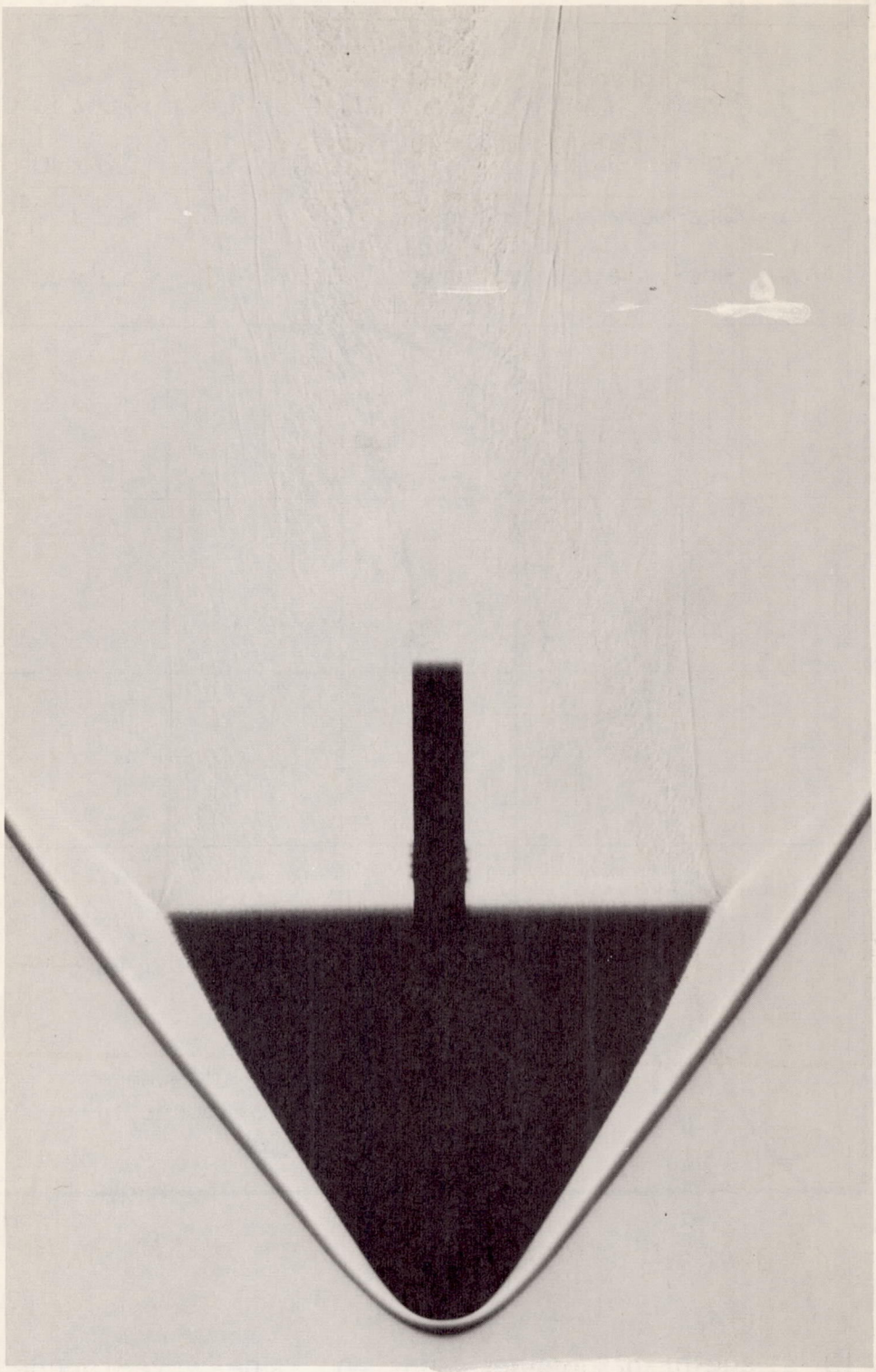


Figure 18.- Sine-wave-rounded ogive, $M_\infty = 4$.

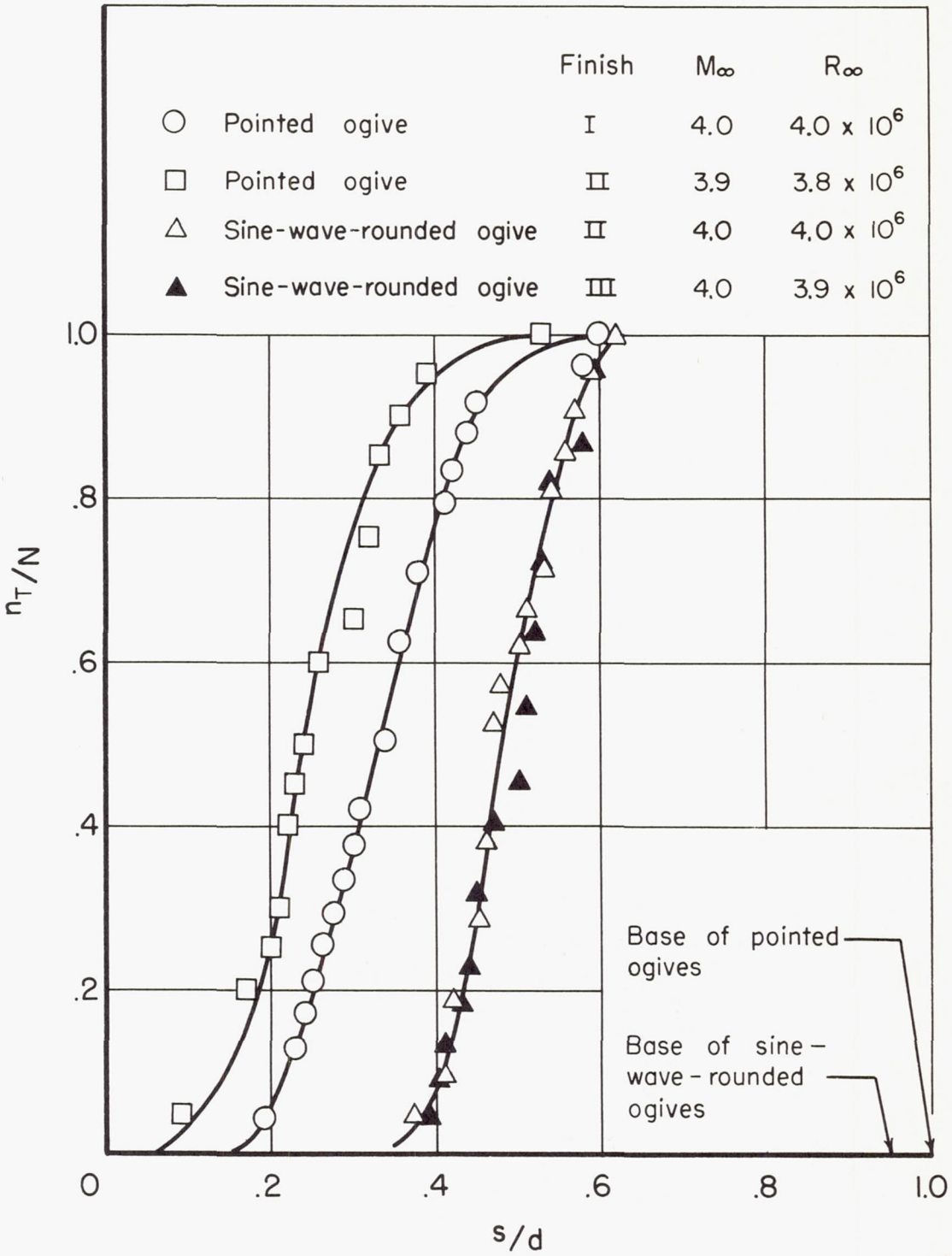


Figure 19.- Length of laminar runs on sine-wave-rounded ogives compared with those on pointed ogives.

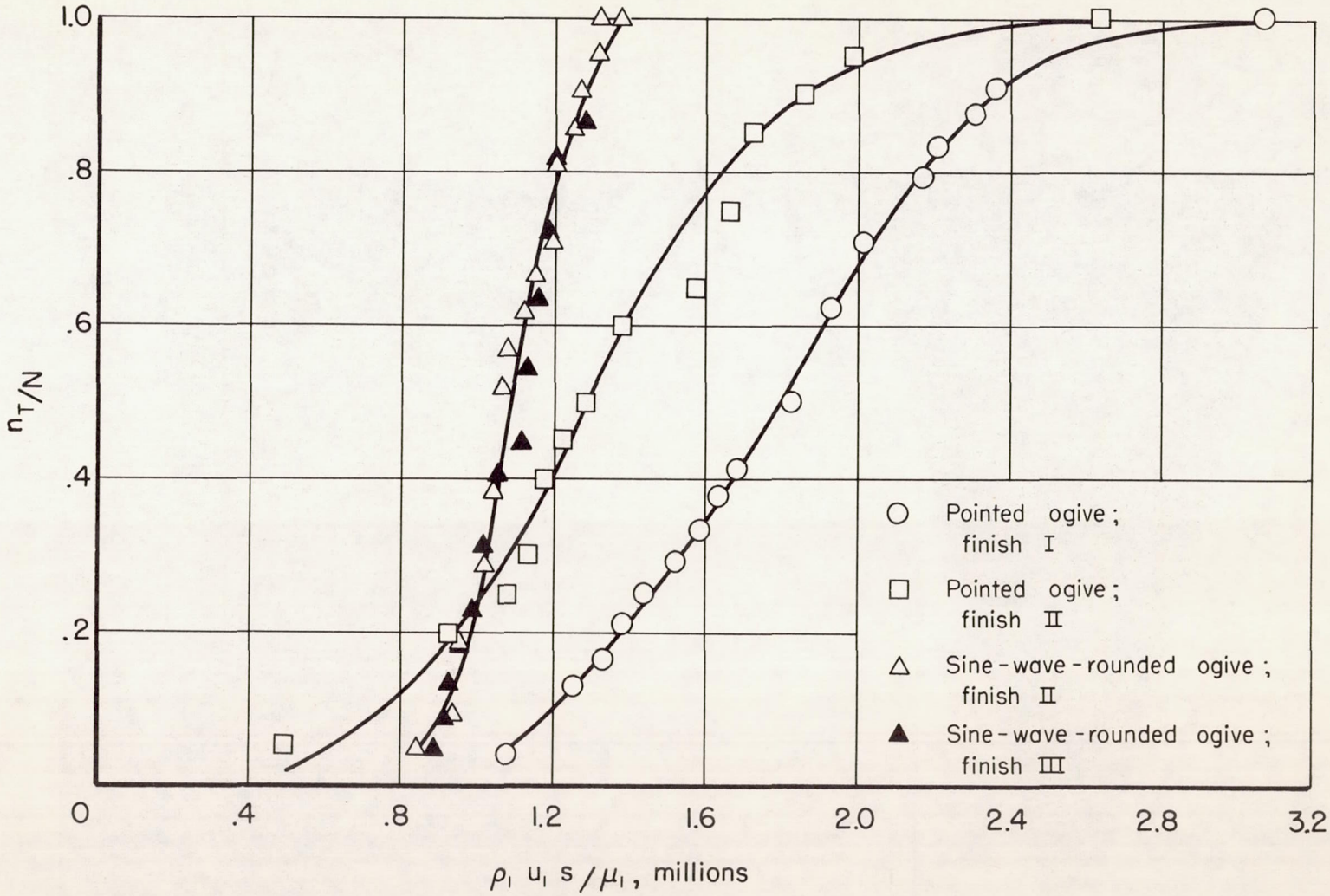
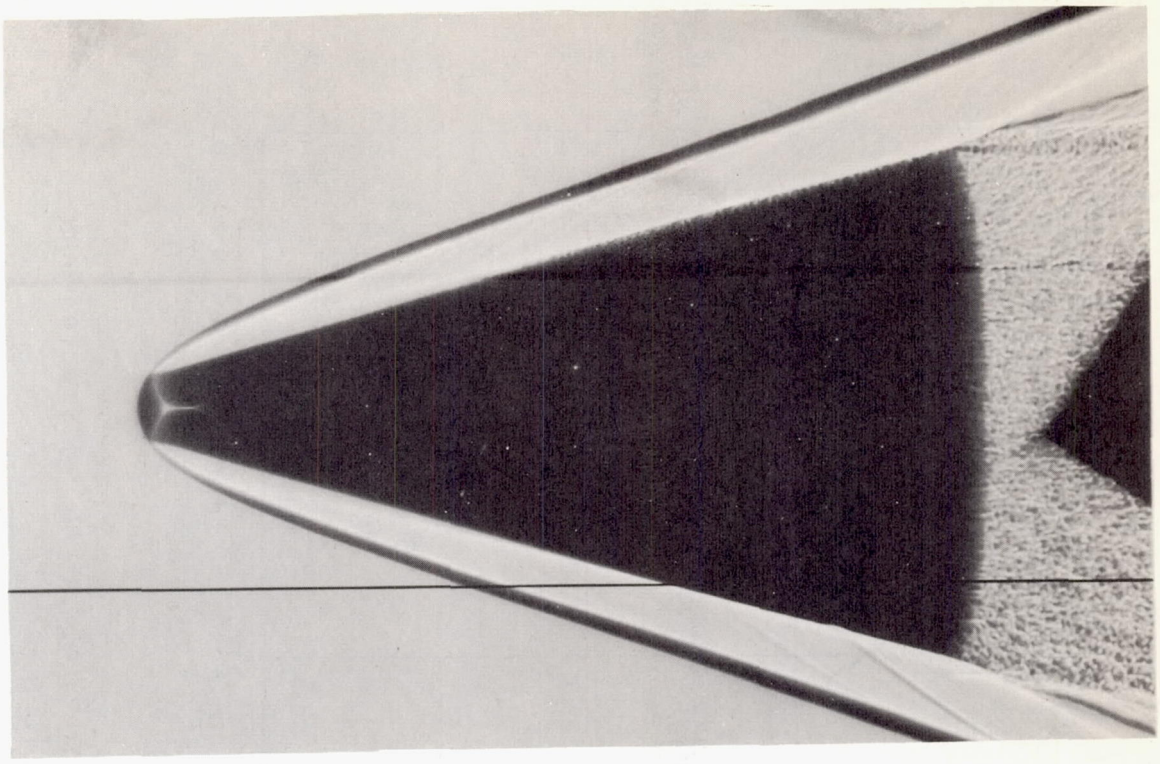
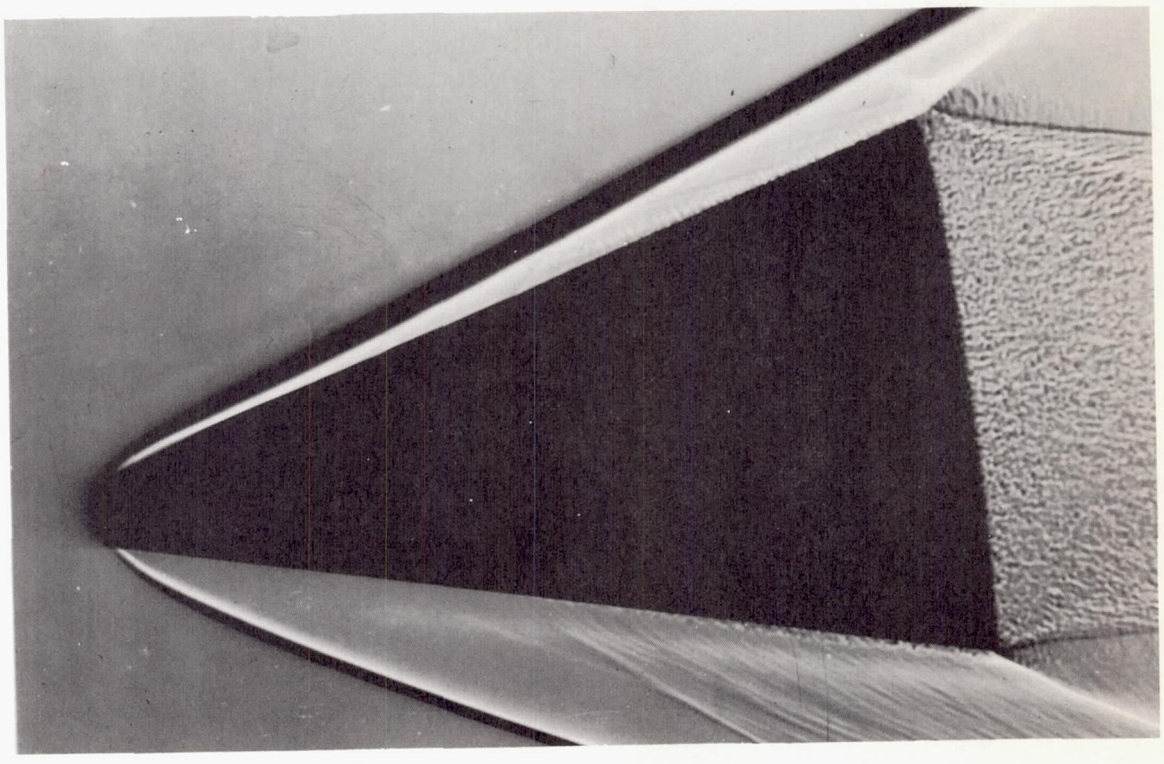


Figure 20.- Comparison of local transition Reynolds numbers on sine-wave-rounded and pointed ogives; $M_\infty = 4$, $R_\infty = 4 \times 10^6$.



(a) Small angle of attack.



(b) Large angle of attack.

Figure 21.- Round-nosed 30° cone, $M_\infty = 4.3$.

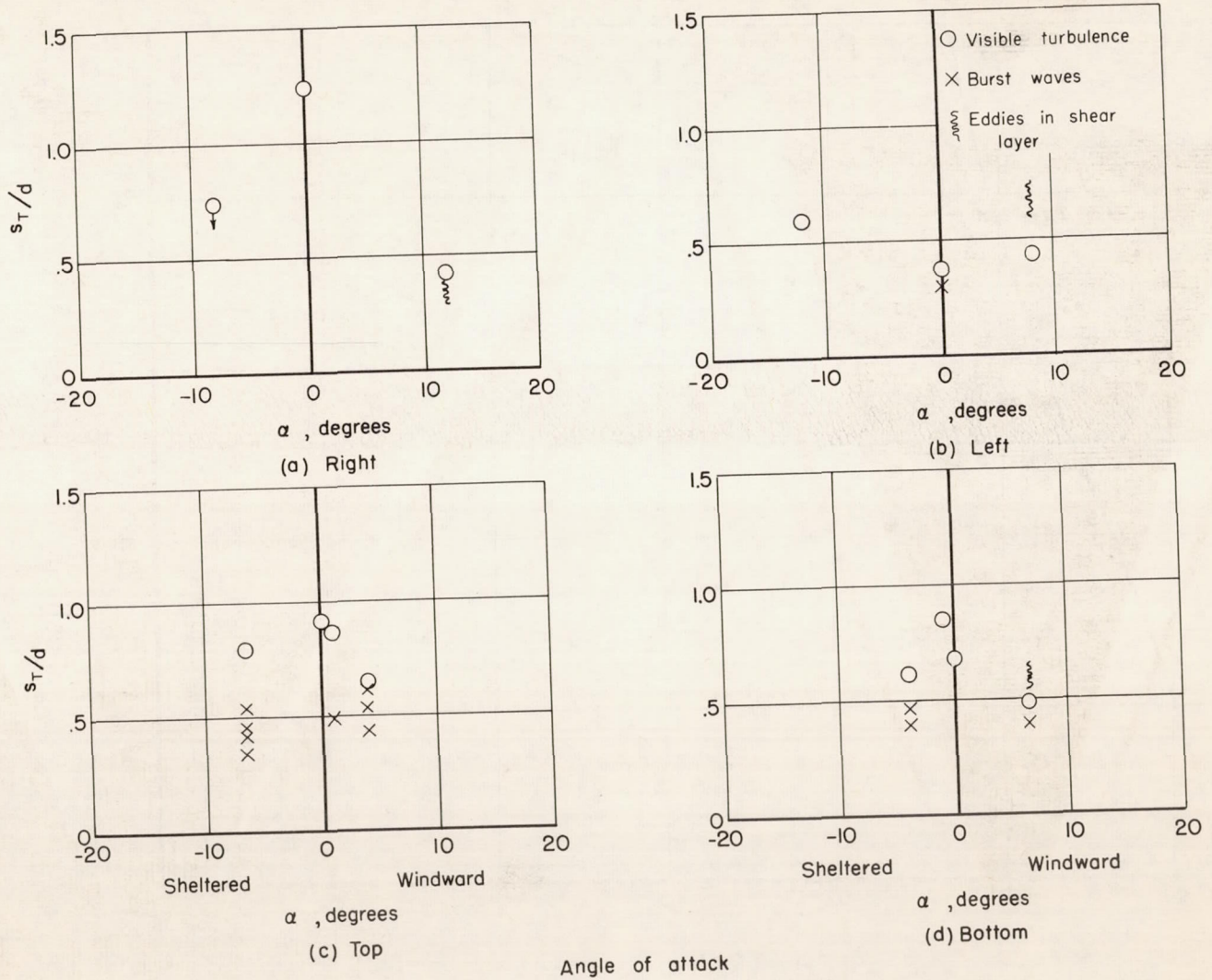


Figure 22.– Length of laminar run on round-nosed 30° cone.

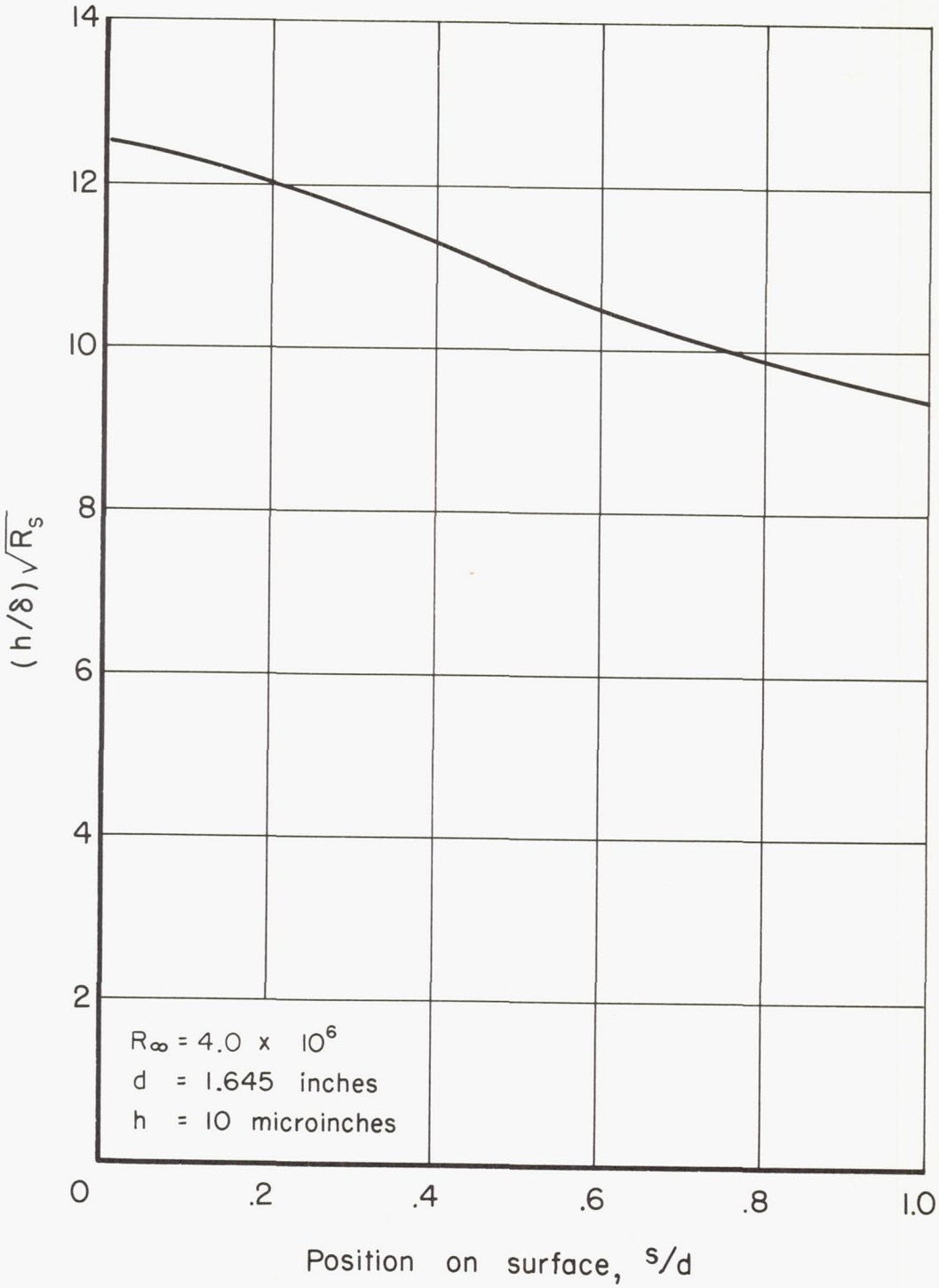


Figure 23. - Variation of roughness parameter over surface of pointed ogive.

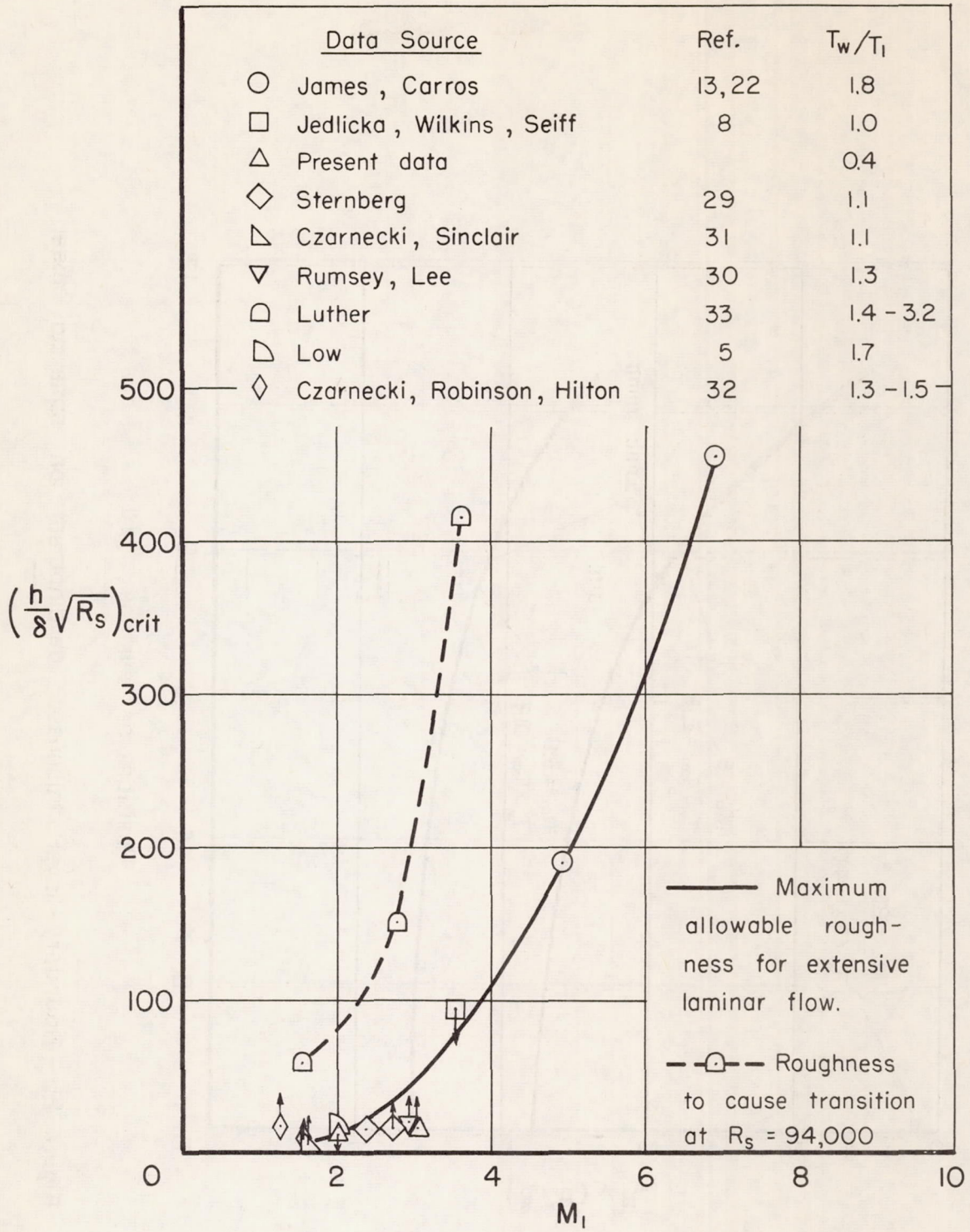


Figure 24.– Variation of critical-roughness parameter with boundary-layer-edge Mach number for pointed bodies.

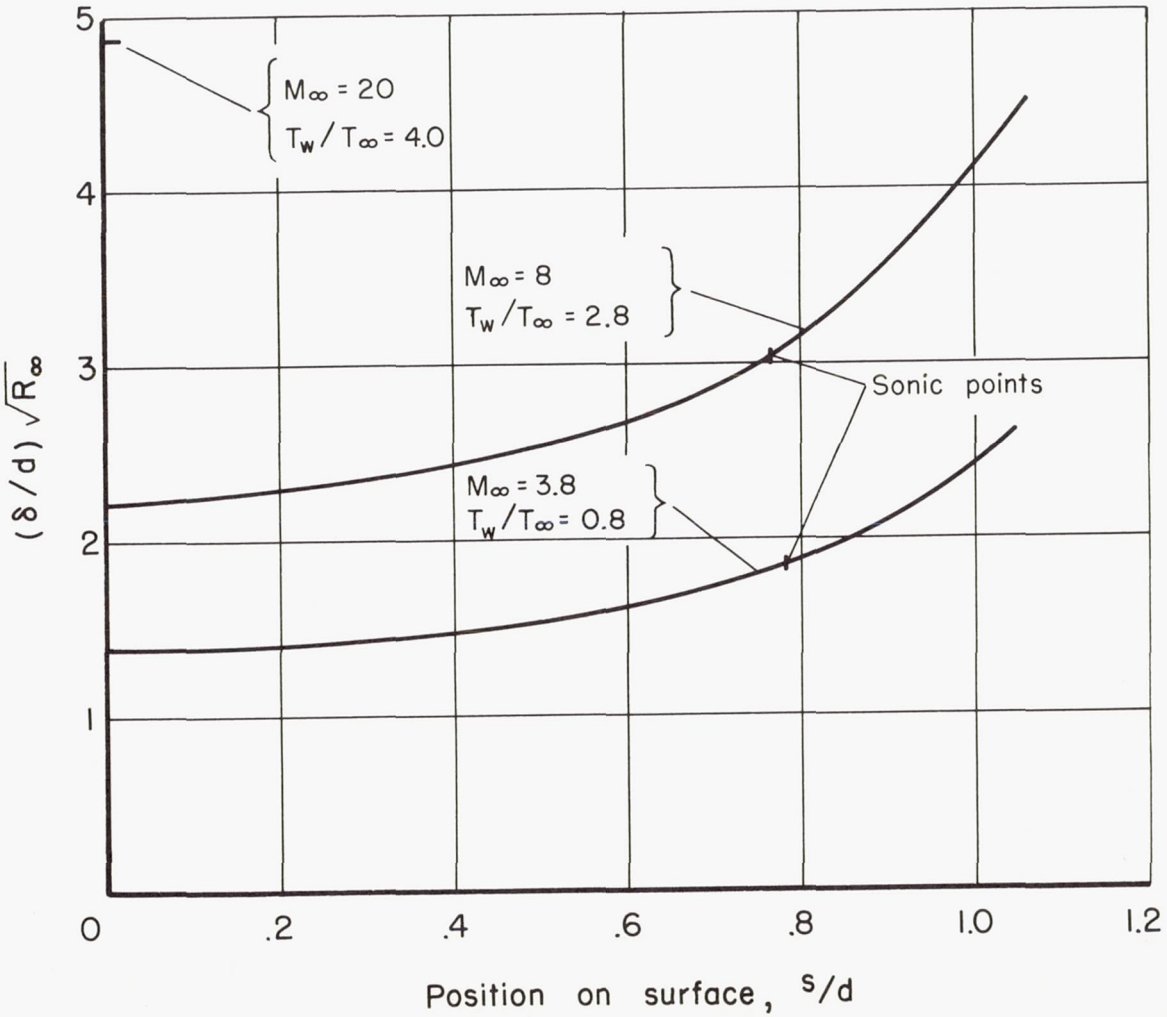


Figure 25.- Boundary-layer thickness development on spherical nose.

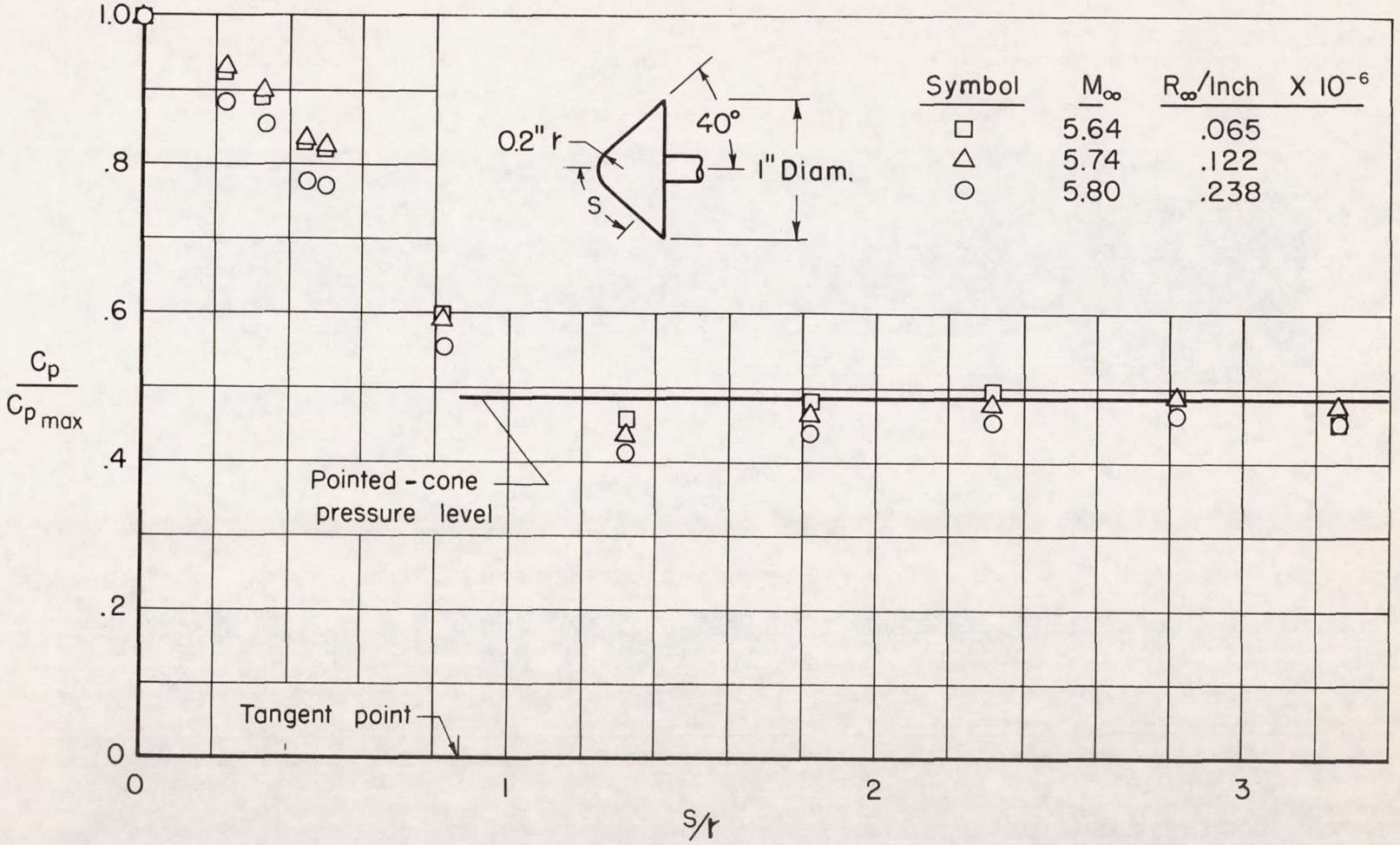
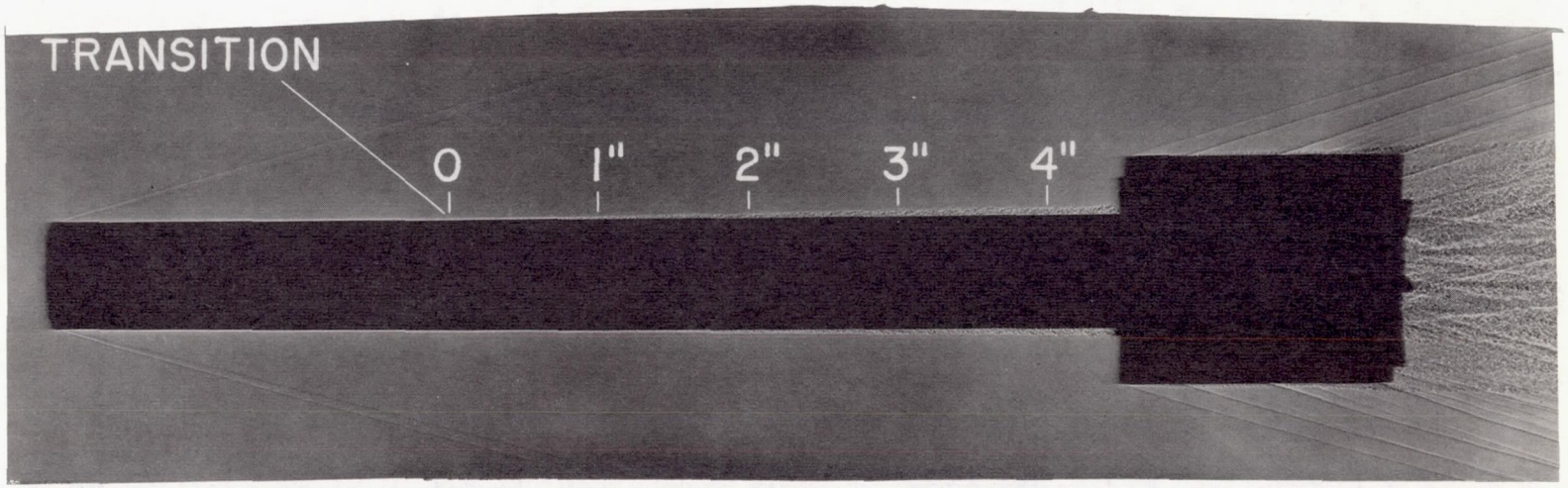
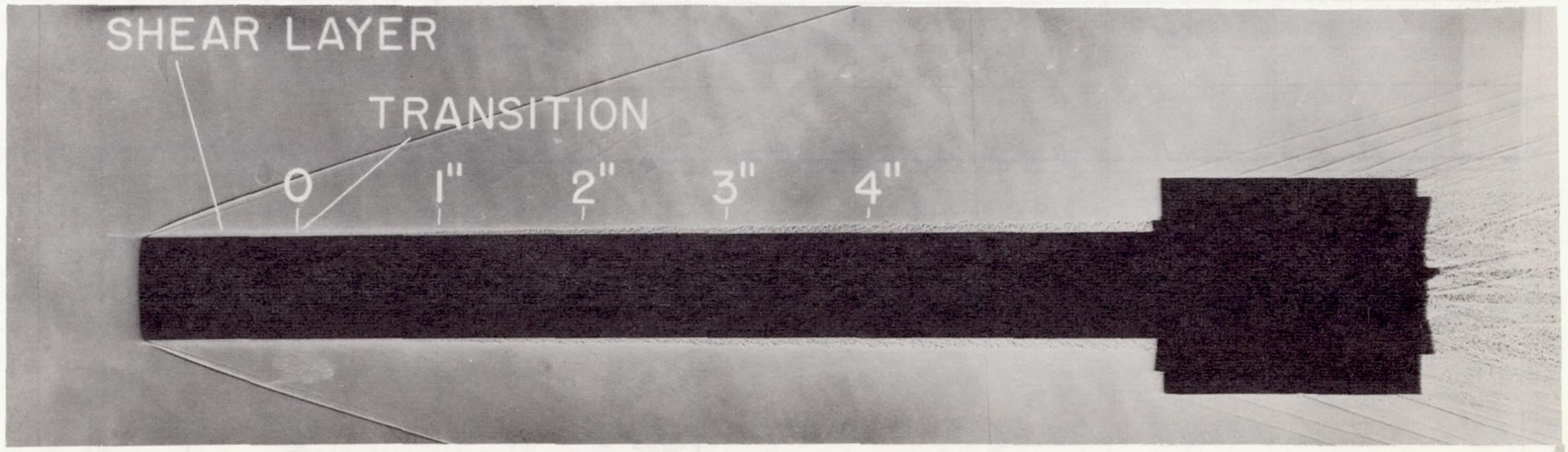


Figure 26.- Pressure - distribution data for the round - nosed 80° cone of reference 9.



(a) Leading-edge thickness = 0.0003 inch.



(b) Leading-edge thickness = 0.0100 inch.

Figure 27.- Comparison of turbulent boundary-layer initial growth rates with and without an appreciable inviscid shear layer due to leading-edge bluntness; $M_\infty = 3.8$, $R_\infty = 17 \times 10^6$, based on cylinder length.

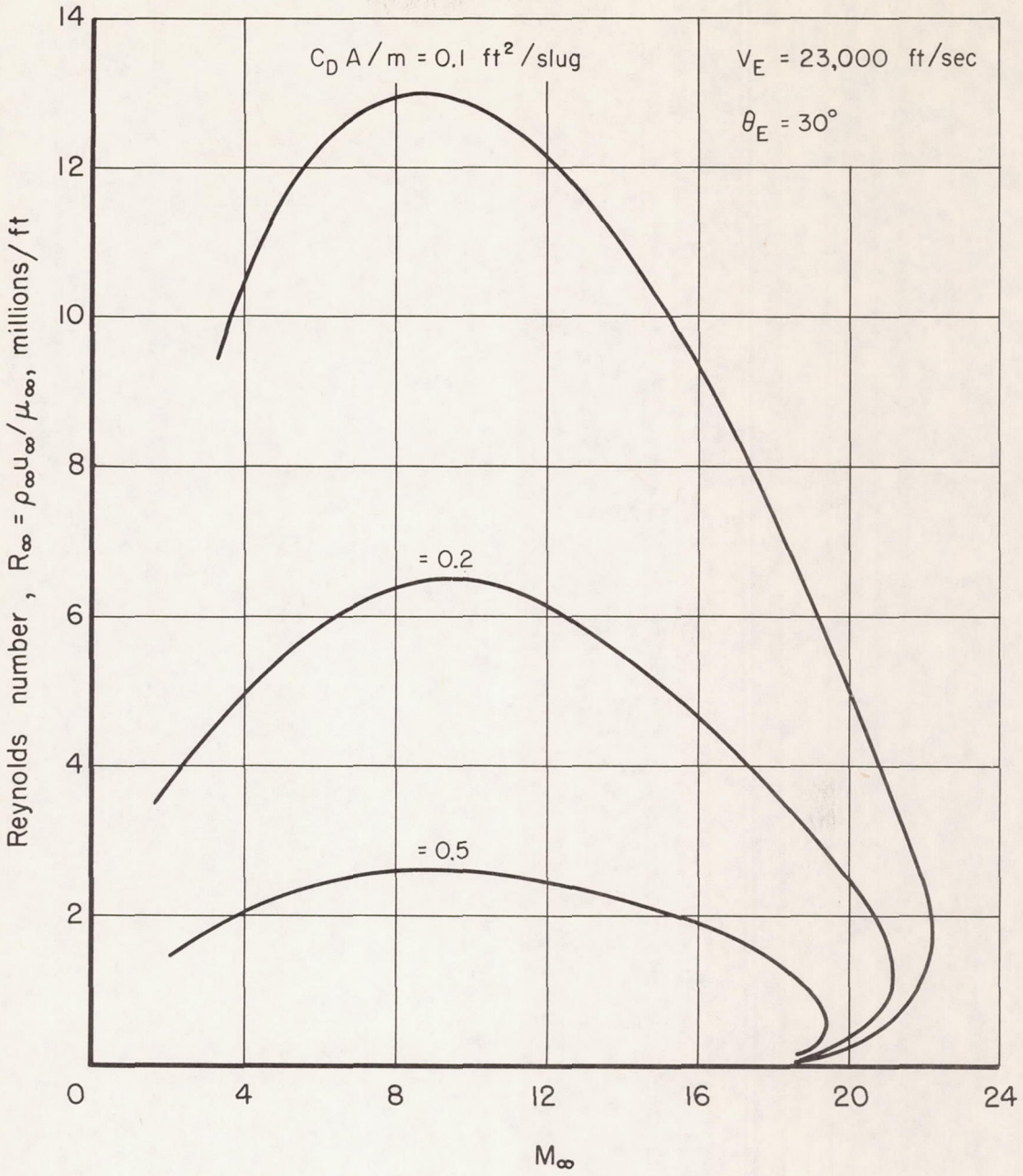


Figure 28.-Effect of ($C_D A/m$) on Reynolds numbers of missiles entering the atmosphere.